



LUND UNIVERSITY

Nuclear spin interactions and coherent control in rare-earth-ion-doped crystals for quantum computing

Syed, Hafsa

2022

Document Version:

Publisher's PDF, also known as Version of record

[Link to publication](#)

Citation for published version (APA):

Syed, H. (2022). *Nuclear spin interactions and coherent control in rare-earth-ion-doped crystals for quantum computing*. Lunds Universitet/Lunds Tekniska Högskola.

Total number of authors:

1

General rights

Unless other specific re-use rights are stated the following general rights apply:

Copyright and moral rights for the publications made accessible in the public portal are retained by the authors and/or other copyright owners and it is a condition of accessing publications that users recognise and abide by the legal requirements associated with these rights.

- Users may download and print one copy of any publication from the public portal for the purpose of private study or research.
- You may not further distribute the material or use it for any profit-making activity or commercial gain
- You may freely distribute the URL identifying the publication in the public portal

Read more about Creative commons licenses: <https://creativecommons.org/licenses/>

Take down policy

If you believe that this document breaches copyright please contact us providing details, and we will remove access to the work immediately and investigate your claim.

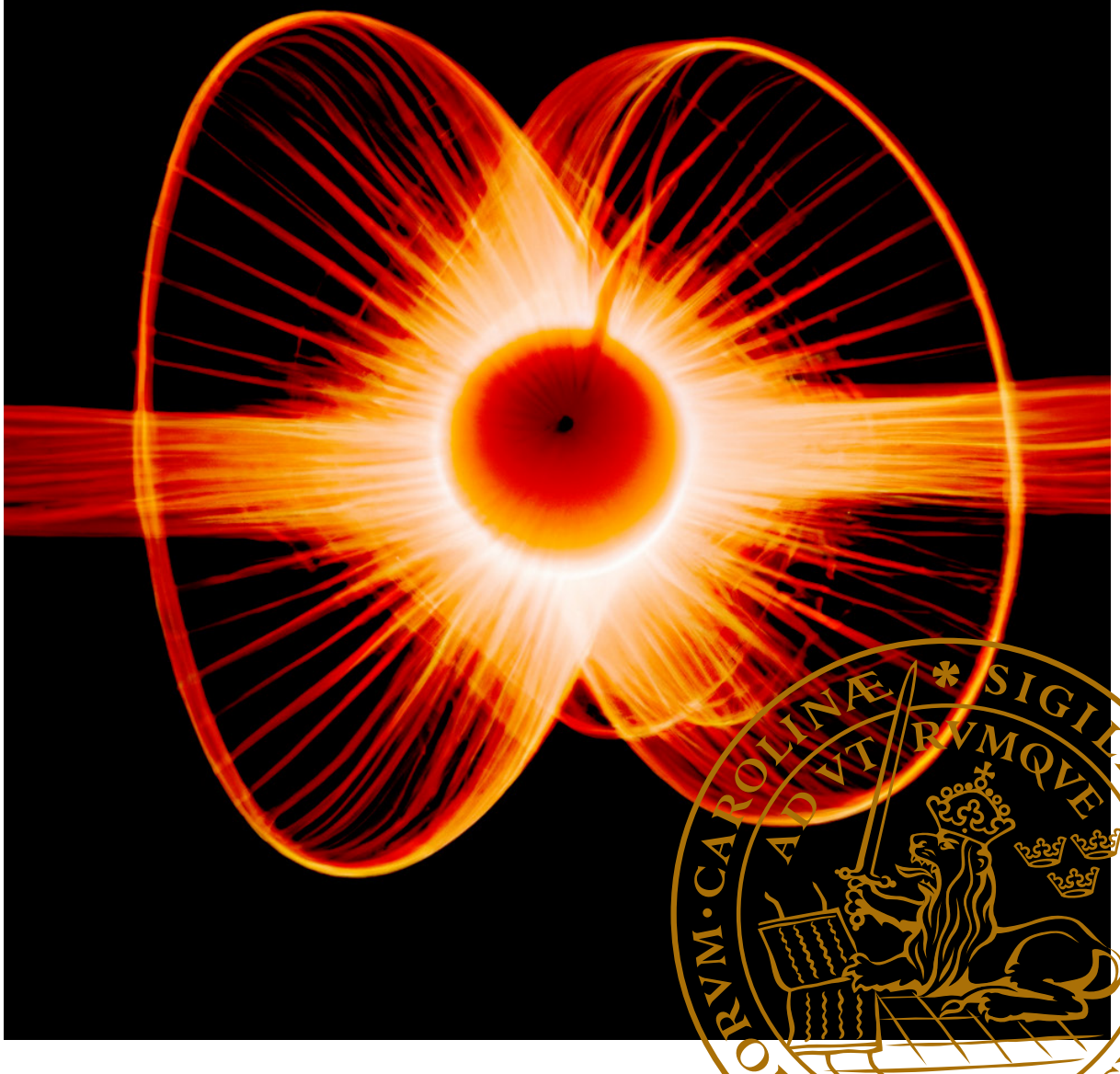
LUND UNIVERSITY

PO Box 117
221 00 Lund
+46 46-222 00 00

Nuclear spin interactions and coherent control in rare-earth-ion-doped crystals for quantum computing

HAFSA SYED

DEPARTMENT OF PHYSICS | FACULTY OF ENGINEERING | LUND UNIVERSITY



Nuclear spin interactions and coherent control in
rare-earth-ion-doped crystals for quantum computing

Nuclear spin interactions and coherent control in rare-earth-ion-doped crystals for quantum computing

by Hafsa Syed



LUND
UNIVERSITY

Thesis for the degree of Doctor of Philosophy

Thesis advisors: Prof. Stefan Kröll, Dr. Andreas Walther, Dr. Chunyan Shi

Faculty opponent: Dr. Signe Seidelin

To be presented, with the permission of the Faculty of Engineering of Lund University, for public criticism in the Rydberg lecture hall (Rydbergsalen) at the Department of Physics on Friday, the 16th of December 2022, at 9.15 a.m.

Organization LUND UNIVERSITY Department of Physics Box 118 SE-221 00 LUND Sweden	Document name Doctoral Dissertation	
Author(s) Hafsa Syed	Date of disputation 2022-12-16	
	Sponsoring organization	
Title and subtitle Nuclear spin interactions and coherent control in rare-earth-ion-doped crystals for quantum computing		
<p>Abstract</p> <p>This thesis work concerns studies of two rare-earth-ions, praseodymium (Pr^{3+}) and europium (Eu^{3+}), doped into a yttrium orthosilicate (Y_2SiO_5) crystal for applications in quantum computing. The nuclear spin levels of these ions can have very long coherence times, up to several hours. Coherence can also be effectively transferred between the optical and hyperfine levels. These systems, therefore, have been extensively used for storing quantum information e.g. quantum memories and quantum computing. With the goal of working towards building a rare-earth quantum computer, the aim of this thesis work is to understand the processes affecting the lifetime of the hyperfine states used as qubits and design ways to achieve high-fidelity gate operations.</p> <p>One of the mechanisms of relaxation between hyperfine levels is flip-flop processes due to magnetic dipole-dipole interaction between neighboring ions. Modeling of this mechanism has generally been macroscopic, characterized by an average rate describing the relaxation of all ions. One part of this thesis presents a microscopic model of flip-flop interactions between individual nuclear spins of dopant ions. Every ion is situated in a unique local environment in the crystal, where each ion has different distances and a unique orientation relative to its nearest neighbors, as determined by the lattice structure and the random doping. Thus, each ion has a unique flip-flop rate and the collective relaxation dynamics of all ions in a bulk crystal is a sum of many exponential decays, giving rise to a distribution of rates rather than a single average decay rate. The model can serve as a general tool to calculate other kinds of interactions at the microscopic level and it could also be used to study the dynamics of other rare-earth ions in different materials.</p> <p>Another part of this thesis identifies several limitations in the rare-earth system that must be overcome in order to successfully perform gate operations with high fidelities. This is presented in the context of ensemble qubits in rare-earth-ions. Although single-ion qubits are essential for scalability, an approach to building small computing nodes using ensemble qubits exists. There is also reason to explore fundamental limitations using the available technology. Two methods to tackle these limitations are presented. One is an adiabatic approach, which is slow but resilient against several imperfections in the system. The second method is 'Shortcut to Adiabaticity', which is a faster approach and can be advantageous to perform operations with high fidelity when the initial and final quantum states are known.</p>		
Key words rare-earth-ion-doped crystals, nuclear spins, magnetic dipole-dipole interactions, flip-flop interactions, quantum computing, high-fidelity		
Classification system and/or index terms (if any)		
Supplementary bibliographical information	Language English	
ISSN and key title 0281-2762, Lund Reports on Atomic Physics, LRAP - 586		ISBN 978-91-8039-402-4 (print) 978-91-8039-401-7 (pdf)
Recipient's notes	Number of pages 122	Price
	Security classification	

I, the undersigned, being the copyright owner of the abstract of the above-mentioned dissertation, hereby grant to all reference sources the permission to publish and disseminate the abstract of the above-mentioned dissertation.

Signature

Date 2022-11-09

Nuclear spin interactions and coherent control in rare-earth-ion-doped crystals for quantum computing

by Hafsa Syed



LUND
UNIVERSITY

A doctoral thesis at a university in Sweden takes either the form of a single, cohesive research study (monograph) or a summary of research papers (compilation thesis), which the licentiate student has written alone or together with one or several other author(s).

In the latter case the thesis consists of two parts. An introductory text puts the research work into context and summarizes the main points of the papers. Then, the research publications themselves are reproduced, together with a description of the individual contributions of the authors. The research papers may either have been already published or are manuscripts at various stages (in press, submitted, or in draft).

Cover illustration front: ‘Expressive orange laser painting of quantum spins atom’
by DALL-E, 9th of November 2022

Cover illustration back: ‘Quantum computing with spin crystals oil painting’
by DALL-E, 9th of November 2022

Funding information: The thesis work was financially supported by the Swedish Research Council, the European Union FETFLAG program, and the Knut and Alice Wallenberg Foundation.

pp i- 88 © 2022 Hafsa Syed
Paper I © 2022 The Authors
Paper II © 2021 The Authors
Paper III © 2022 The Authors

Department of Physics, Faculty of Engineering, Lund University

ISBN: 978-91-8039-402-4 (print)

ISBN: 978-91-8039-401-7 (pdf)

ISSN: 0281-2762, Lund Reports on Atomic Physics, LRAP - 586

Printed in Sweden by Media-Tryck, Lund University, Lund 2022



Media-Tryck is a Nordic Swan Ecolabel
certified provider of printed material.
Read more about our environmental
work at www.mediatryck.lu.se

MADE IN SWEDEN 

*Dedicated to
Ammi and Abbu
For your encouragement and support.*

Contents

Abstract	iv
List of publications	v
Acknowledgements	vi
Popular Scientific Summary	viii
Nuclear spin interactions and coherent control in rare-earth-ion-doped crystals for quantum computing	I
1 Introduction	3
1.1 Requirements for a rare-earth-quantum computer	4
1.2 Aim of this thesis	6
1.3 Outline of this thesis	8
2 Properties of rare-earth-ions	9
2.1 Energy level structure	10
2.2 Lifetime of hyperfine levels	12
2.3 Homogeneous and Inhomogeneous linewidth	12
2.4 Absorption coefficient	14
2.5 Pr^{3+} and Eu^{3+} doped in YSO	14
3 Nuclear spins and interactions	17
3.1 Magnetic dipoles in an external magnetic field	17
3.2 Nuclear spins of rare-earth-ions	19
3.2.1 Spin Hamiltonian	20
3.2.2 Dipole-dipole interactions	22
3.2.3 Decoherence from magnetic interactions	24
4 Relaxation of nuclear spins of rare-earth-ions	25
4.1 Spin-lattice relaxation	25
4.2 Relaxation via flip-flops	27
4.3 Modeling of flip-flops	28
4.3.1 Validity of Fermi's Golden Rule (FGR)	29
4.3.2 Microscopic modeling	30
4.4 Measuring flip-flops	32
4.4.1 Experimental results	33

4.4.2	Effect of magnetic field	36
4.4.3	Distribution of Rates	37
4.4.4	Effect of concentration	37
5	Ensemble qubits and coherent control	41
5.1	Control pulses	41
5.1.1	Sechyp	41
5.1.2	Two-color pulses	42
5.1.3	Sechscan	44
5.2	Creating ensemble qubits	46
5.2.1	Pr:YSO	46
5.2.2	Eu:YSO	49
5.3	Calibrating the available Rabi frequency	50
5.4	Readout	51
5.5	Detection	51
5.5.1	Noise characterization	53
5.6	Deconvolution errors	54
6	High fidelity transfers	57
6.1	Evolution of a quantum system using Lindblad equation	58
6.2	Shortcut to Adiabaticity	60
6.2.1	Lewis-Reisenfeld Invariants	60
6.2.2	Inverse engineering	61
6.2.3	Experimental implementation	63
6.2.4	Experimental results	65
6.2.4.1	Transfers between two ground states	65
6.2.4.2	Transfer between ground and superposition state	65
6.2.5	Conclusions	67
6.3	Adiabatic Approach	68
6.3.1	Choice of material	68
6.3.2	Trade-off in experimental design	68
6.3.3	Technical challenges and experimental setup	70
6.3.4	Inhomogeneity in Rabi Frequency	72
6.3.5	Creating and reading out ensemble qubits	73
6.3.6	Transfer Pulse design	74
6.3.7	Experimental Results	78
6.3.8	Performance of two-color gates	80
6.3.9	Summary of challenges and outlook	80
7	Conclusions	83
7.1	Personal perspective	84
	References	87

Scientific publications	99
Author contributions	99
Paper I: Microscopic model of spin flip-flop processes in rare-earth-ion-doped crystals	99
Paper II: Experimental implementation of precisely tailored light-matter interaction via inverse engineering	99
Paper III: Towards high fidelity transfers in $\text{Eu}^{3+} : \text{Y}_2\text{SiO}_5$ for quantum computing applications	99
Paper I: Microscopic model of spin flip-flop processes in rare-earth-ion-doped crystals	101
Paper II: Experimental implementation of precisely tailored light-matter interaction via inverse engineering	103
Paper III: Challenges towards high fidelity gates using ensemble qubits in rare-earth-ion-doped crystals	105

Abstract

This thesis work concerns studies of two rare-earth-ions, praseodymium (Pr^{3+}) and europium (Eu^{3+}), doped into a yttrium orthosilicate (Y_2SiO_5) crystal for applications in quantum computing. The nuclear spin levels of these ions can have very long coherence times, up to several hours. Coherence can also be effectively transferred between the optical and hyperfine levels. These systems, therefore, have been extensively used for storing quantum information e.g. quantum memories and quantum computing. With the goal of working towards building a rare-earth quantum computer, the aim of this thesis work is to understand the processes affecting the lifetime of the hyperfine states used as qubits and design ways to achieve high-fidelity gate operations.

One of the mechanisms of relaxation between hyperfine levels is flip-flop processes due to magnetic dipole-dipole interaction between neighboring ions. Modeling of this mechanism has generally been macroscopic, characterized by an average rate describing the relaxation of all ions. One part of this thesis presents a microscopic model of flip-flop interactions between individual nuclear spins of dopant ions. Every ion is situated in a unique local environment in the crystal, where each ion has different distances and a unique orientation relative to its nearest neighbors, as determined by the lattice structure and the random doping. Thus, each ion has a unique flip-flop rate and the collective relaxation dynamics of all ions in a bulk crystal is a sum of many exponential decays, giving rise to a distribution of rates rather than a single average decay rate. The model can serve as a general tool to calculate other kinds of interactions at the microscopic level and it could also be used to study the dynamics of other rare-earth ions in different materials.

Another part of this thesis identifies several limitations in the rare-earth system that must be overcome in order to successfully perform gate operations with high fidelities. This is presented in the context of ensemble qubits in rare-earth-ions. Although single-ion qubits are essential for scalability, an approach to building small computing nodes using ensemble qubits exists. There is also reason to explore fundamental limitations using the available technology. Two methods to tackle these limitations are presented. One is an adiabatic approach, which is slow but resilient against several imperfections in the system. The second method is ‘Shortcut to Adiabaticity’, which is a faster approach and can be advantageous to perform operations with high fidelity when the initial and final quantum states are known.

List of publications

This thesis is based on the following publications, referred to by their Roman numerals:

- I Microscopic model of spin flip-flop processes in rare-earth-ion-doped crystals**
H. Syed, A. Kinos, C. Shi, L. Rippe, and S. Kröll
Manuscript in review, *Phys. Rev. B*.

- II Experimental implementation of precisely tailored light-matter interaction via inverse engineering**
Y. Yan, C. Shi, A. Kinos, H. Syed, S. P. Horvath, A. Walther, L. Rippe, X. Chen and S. Kröll
npj Quantum Inf. 7, 138 (2021)

- III Challenges towards high fidelity transfers in $\text{Eu}^{3+} : \text{Y}_2\text{SiO}_5$ for quantum computing applications**
H. Syed, A. Walther, A. Kinos, L. Rippe, and S. Kröll
Manuscript in preparation

Acknowledgements

First and foremost, I thank my supervisor, Prof. Stefan Kröll. I am grateful for your guidance and discussions about physics or life in general. I appreciate your support and advice, whether in good or challenging times.

Several people in the Quantum Information group have made my time here enjoyable. Andreas, thank you for all the discussions and your comments on my thesis. Thank you, Lars, for sharing your excitement about physics and electronics and for popping into the lab for a chat over the years. I want to thank Adam for many discussions about physics and problems in the lab and the simulations. Conversations with you were always uplifting. Thank you, Chunyan, for being so encouraging and instilling confidence in me on not-so-good days. Thank you, Sebastian, for being kind and for being such good friends with the dye laser and everything else in the lab. I also wish to thank Yan for the good times in the lab when you visited us. David (G), thank you for teaching me the most absurd Swedish words. Mohammed, thank you for the laughs while setting up the QC labs. David (H), thank you for attempting to teach me how to swim. For all the 'Fancy Fridays', 'Whacky Wednesdays', 'Salad Thursdays', Fika, and group activities thank you, Alex, Marcus, Kevin, Steffen, Haitham, and Arvid.

I have so many other people in the division to be thankful for. My old office mates - Samuel and Anna, thank you for always greeting me with a big smile. Cornelia, thank you for the fun chats over lunch. Anka, thank you for walking me back home after the LLC day and procuring the beverages from Germany. Åke, thanks for helping me with anything computer-related. Anne P.J, Jakob, Maria, and Jane, thank you for helping with the administrative work. To everyone else at the division - I am happy to have been part of this division and to have shared good times with you all, be it over Fika or just passing by you in the corridor with a smile and a greeting. I also need to thank Jonas at MediaTryck for being so patient with me.

My board games group of friends - Karl, Tim, Vidar, Ace, and Stelios - thank you for all the enjoyable times! Meng, thank you for bringing me treats and lighting up my day. My climbing buddies - Mads, Annika, Elisabeth, Emil - thanks for the great times at the gym. Kalyani, Dinesh, and Suman, thank you for the badminton Saturdays.

My family away from home - Emmy and Neha, thank you for always being there for me. I am so excited to welcome Tarun soon! CJ, thanks for everything, very cool. Kailash, Soni, Vivek, Jennifer, Nimba, Amit, Rajiv, Vidit, Sameeksha, Sunny, Dhanu, Shradha, and Ashwin - thank you for all the good times at the festivals and celebrations. Sruthi, thanks for being my dance partner, dude. Rohit, thanks for the special seating arrangements at your defense party...that worked out for me very well!

My friend back home - Greeshma, thank you for being the happiest person to see me every time I visit. Chimmu, thank you for all the beautiful hikes in Sweden! Harsha, Rishav, Harish, Vamsi, Ashwin, Akshay, Anu, Sushma, Nikhila, and Rijutha - thank you for all the good times during the years in college and for so many years after that. Surya and Charu, thank you for the enjoyable time at RRI. Taha, thank you for all the times we gossiped about the family. Nihaan and Fauzan, thank you for getting me excited about longboarding. To everyone in the family, thank you for your prayers.

Didi, thank you for being my hero and for being so strong. Most of all, I am thankful to Ammi and Abbu. Words will fail to express my gratitude for you.

Popular Scientific Summary

A classical computer's workhorse is a transistor that can behave as a switch and has two states: 'on' and 'off' (or 1 and 0). Using this simple property, integrated circuit chips were developed to compute complex operations quickly. The computing power increases with the number of transistors one can jam into a single chip. But technology has advanced so much today that we are approaching the limit of fitting in more transistors to gain computing power. One approach that seeks to increase the computing power for a specific set of problems is *quantum computing*. This is very different from classical computing and requires the knowledge of a separate branch of physics known as quantum mechanics. While a quantum computer will not replace our laptops, we are approaching a new era of computing using both classical and quantum computers. One of the world's leading companies in computing, IBM, calls this 'quantum-centric supercomputing'. There are also many classes of problems that can only sufficiently be solved using quantum mechanics and can potentially pave new paths to secure information, for example, the data stored on our credit cards.

A considerable effort has been devoted to making quantum computing a usable technology, both by industrial companies and research institutions worldwide. And a plethora of platforms can be used as building blocks of a quantum computer. One example of such a system is the nucleus of an atom. It can behave akin to a magnetic compass, which always points towards the north pole. This property is historically known as 'spin' and is purely quantum mechanical in nature. A key feature of quantum mechanical systems is 'superposition': a system can have states beyond just '0' and '1' (written as $|0\rangle$ and $|1\rangle$) and is allowed to have different combinations of $|0\rangle$ and $|1\rangle$. The creation of such superposition states and the ability to manipulate them is imperative to quantum computing.

Nuclear spin states of some elements known as 'rare-earth-ions' can be very long-lived when embedded in a transparent crystal. They can also be controlled using laser light: thus, the state can be initialized, manipulated, and read out by shining light on these crystals. Another attractive feature is that the crystals serve as a relatively quiet environment for the rare-earth-ions to live in, so any information stored in the states is not easily lost due to environmental disturbances. A large part of this thesis is about understanding the *magnetic* personalities of the nuclear spins of the rare-earth-ions and exploring ways of making them dance to the tune of light.

Nuclear spin interactions and coherent control in rare-earth-ion-doped crystals for quantum computing

Chapter 1

Introduction

Why quantum computers?

The inspiration for building a quantum computer is often credited to Richard P. Feynman, who ended his speech *Simulating Physics with Computers* [1] with the following words:

‘..I’m not happy with all the analyses that go with just the classical theory, because nature isn’t classical, dammit, and if you want to make a simulation of nature, you’d better make it quantum mechanical, and by golly it’s a wonderful problem, because it doesn’t look so easy.’

The essence of his speech was that one needs a system that uses the principles of Quantum Mechanics to understand other quantum mechanical phenomena. This problem is not easy because quantum systems need to be isolated from the environment to use them for any computing purposes. The theoretical knowledge on this problem is immense, but more often than not, technological advancements fall short of achieving this goal.

Several platforms are being used to realize a quantum computer - superconducting qubits [2–4], trapped ions [5–7], optical photons [8, 9], and nitrogen-vacancy centers in diamonds [10], only to mention a few. This field of research has gained momentum in the past few decades but it is not clear which platform will ultimately become a scalable and useful quantum computer. Most efforts today are, however, invested into superconducting qubits including substantial efforts from major companies like IBM, Google, Rigetti, etc. IBM has successfully made a quantum processor with 127 qubits, with a qubit connectivity of 2-3. The fidelity error on single-qubit and two-qubit gates is $1 - 7 \cdot 10^{-2}$ [3]. Google has 54 qubits and the fidelity error on

single-qubit operations could be 10^{-3} and the two-qubit operations could be $2 \cdot 10^{-2}$ [11]. IonQ, a company that uses ion traps has achieved single-qubit errors of $5 \cdot 10^{-4}$ and two-qubit gate errors of $4 \cdot 10^{-3}$. It has demonstrated connectivity between all of its 21 qubits [12]. Rare-earth-ions are another promising platform for quantum computing, although they have not yet demonstrated equally impressive results. This thesis aims towards building a rare-earth quantum computer (REQC).

1.1 Requirements for a rare-earth-quantum computer

A joint effort by several research groups in Europe, under the European Flagship project, ‘Scalable QUAntum computing nodes with Rare-Earth ions’ (SQUARE), has led to the laying down of a Roadmap[13] for the present status and prospects of using rare-earth-ions for quantum computing. The criteria to be satisfied for building a quantum computer were given by DiVincenzo[14] in the year 2000. There are five requirements and here, each point is discussed in the context of rare-earth-ion quantum computing as envisioned in the roadmap:

1. A scalable physical system with well-characterized qubits

The most promising rare-earth (RE) approach to scalability is using single RE ions, where one species is used for qubit operations and another species is used as a readout ion. When rare-earth-ions are doped into crystals and cooled down to ~ 4 K, one can shield them from the environmental noise very well and store quantum information for a long time. The nuclear spin states are used as qubit levels and they are accessed via an optically excited state. There could be several candidates to be used as the qubit ion, and europium (Eu^{3+}) seems to have favorable properties. Theoretical investigations have been made using single-ion qubits in Eu^{3+} doped into Yttrium orthosilicate (Eu^{3+} : Y_2SiO_5 or $\text{Eu}:\text{YSO}$ for short) with encouraging results [15, 16]. Another approach could be to use ensemble qubits in stoichiometric crystals to build small processor nodes[17]. This thesis explores the use of ensemble qubits in randomly doped crystals.

2. The ability to initialize the state of the qubits to a simple fiducial state, such as $|000\rangle$

Rare-earth-ion-doped crystals also have an inhomogeneous broadening, which allows the preparation of a qubit in different spectral regions within the inhomogeneously broadened line. Qubits can be differentiated from each other depending on their resonant optical frequency (in other words, their spectral position in the inhomogeneous line). The number of potentially accessible

qubit channels is the ratio of the inhomogeneous linewidth to the homogeneous linewidth of the optical transitions. This could be $\sim 10^6$, discussed in Ch. 2.

The initialization of the state of the qubits involves principles of optical pumping and spectral hole burning. Transparent spectral windows are first prepared and then the qubits are initialized in this spectral region to isolate from other non-qubit ions, thus minimizing off-resonant excitations. The wider the transmission spectral window, the better. Nominally, qubits can be separated by about 1 GHz. This technique is common to single-ion qubits as well as ensemble qubits. This has been fairly well established, for example, initialization of an ensemble qubit in praseodymium ion or Pr^{3+} doped in YSO [18]. This will be discussed in Ch. 5. Paper II shows a new experimental technique that could be used to initialize qubits to a known state with a fidelity of $\sim 0.98\%$.

Currently, the time it takes to initialize the qubit is much longer than the lifetime of the optically excited state. In a full quantum algorithm, this is not ideal since the duration of the initialization step should be comparable to a gate operation. Additionally, there are technological limitations. The laser source used to address the qubits in frequency needs to be able to switch several GHz in a few microseconds. The laser tuning range directly limits the connectivity of the qubits, but with sufficient tuning range, the average connectivity per qubit could be about 50 [13].

3. Long relevant decoherence times, much longer than the gate operation time

Europium or Eu^{3+} has a very long lifetime of 1.9 ms and coherence time of 1.5 ms, as will be discussed in Ch. 2. The large splitting between the hyperfine levels also allows the use of pulses much shorter than the gate operation time. The hyperfine levels in Eu^{3+} can live longer than 49 days [19] and the hyperfine coherence time could be as long as six hours [20] in the presence of an external magnetic field.

4. A ‘universal’ set of quantum gates

A scheme to perform arbitrary rotations on the Bloch sphere has been experimentally demonstrated [21]. They are implemented using two-color optical pulses and this technique will be discussed in Ch. 5. Including the effects of decay, decoherence, and internal cross-talk, single-ion-qubit operations can be $\sim 3.4 \mu\text{s}$ long, where the realistic fidelity errors could be $\sim 10^{-4}$ [15] in simulations. Entanglement can be achieved using the dipole-blockade mechanism [22, 23] and the simulated two-qubit gate errors can be between $10^{-4} - 10^{-3}$ [15], over a range of dipole-dipole shifts, of about 100 MHz.

Unfortunately, the errors in single-qubit operations on ensembles are not this low due to several sources of inhomogeneities. This has been shown in experiments. In Pr:YSO, the experimental errors could be about 4% [21] and the primary limitation is the coherence time. In Eu:YSO, where coherence times are longer, the limitation is the weak oscillator strength of the transitions. The laser power available may then be insufficient to drive the transitions and thus longer pulses need to be designed. Spin inhomogeneity also limits the fidelity to about 95%. These aspects and experimental results are discussed in Paper III.

5. A qubit-specific measurement capability

For the single-ion approach, a rare-earth species different from the qubit ion is chosen as the readout ion, whose emission can be Purcell-enhanced by using a cavity with a high-quality factor. The readout ion needs to be coupled to one or several qubit ions through the dipole-blockade mechanism used for two-qubit gates. Neodymium or erbium could be favorable for this purpose. If emission rates of 10^7 photons/s are achieved, readout fidelities $> 99\%$ could be possible [13]. Several nodes can be connected via an optical interface between cavities with readout ions.

In the ensemble approach used in this thesis work, the readout is done using absorption spectroscopy where an optical pulse chirps in frequency, across the ensemble qubit. A full Quantum State Tomography can be done using a scheme with two-color pulses. This has earlier been demonstrated in Pr:YSO [21] and has the same fidelity as the single-qubit operation, $\sim 96\%$.

The above discussion is by no means complete. The objective here has been to provide a glimpse into the field of rare-earth-ion quantum computing and show that rare-earth-ions have some attractive and promising features for quantum computing. A more detailed and thorough discussion of different protocols, their limitations, and current progress are presented in Ref.[13].

1.2 Aim of this thesis

This thesis work aims to understand the processes affecting the lifetime of the hyperfine (nuclear spin) states used as qubits and design ways to achieve high-fidelity gate operations for quantum computing using ensemble qubits in rare-earth-ion-doped crystals. The dominant mechanism affecting the lifetime of the hyperfine states which is relevant for this work is flip-flop interaction. Modeling of this mechanism has so far been macroscopic, characterized by an average rate describing the relaxation of

all ions. In Paper I, a microscopic model of flip-flop interactions between individual nuclear spins of dopant ions is presented. Also, a new method to measure rates of individual transitions from hole burning spectra is presented. It requires significantly fewer fitting parameters in theoretical rate equations compared to earlier work.

Papers II and III are part of the SQUARE project (European Flagship project) and aim to demonstrate high-fidelity single-qubit operations using ensemble qubits. Paper II is an experimental demonstration of a new technique to perform operations in ensemble qubits. This technique, known as ‘Shortcut to Adiabaticity’ uses pulses of shorter duration and it is a good tool to perform operations with high fidelity when the initial and final quantum state are known. Paper III presents an adiabatic approach useful when pulses with low Rabi frequency are required to perform gate operations. Limitations due to several sources of inhomogeneities in ensemble qubits are detailed and the trade-offs to be made in the experimental design are discussed.

As has been pointed out in the section above, one needs single-ion qubits to build a scalable rare-earth quantum computer. The primary reason is that is challenging to find chains of strongly interacting ensemble qubits. While there has been quite some theoretical work investigating gate operations using single-ion qubits [13, 15, 16, 24], technological advancement has been the limiting factor in exploring this area in experiments. Reading out the state of a single ion is challenging due to the low spontaneous emission rate. An approach to overcome this difficulty is using cavities-based approaches. Developments in the detection of single-ions have been made in recent years [25–28] and this is expected to bolster the experimental progress using single-ion-qubits. During the majority of the work in this thesis, these technologies were still in development.

The case of ensemble qubits could still be useful in stoichiometric crystals and ensemble-based operations in atomic frequency comb (AFC) quantum memories. The idea of building small quantum processing nodes using ensembles in stoichiometric crystals was proposed in Ref.[17]. It involves using a stoichiometric crystal in Eu^{3+} , lightly doped with another rare-earth-ion. A cluster of Eu^{3+} spins around the doped ion is characterized by a ‘satellite’ line that can be resolved optically. Each cluster can potentially be used as a qubit, and one can find up to 30 clusters in some materials [29, 30]. Such qubits can potentially be used to perform linear operations and in quantum memories. Another reason to explore ensemble qubits is to understand the requirements for high-fidelity transfers in spin-wave AFC quantum memories [31–33], where operations are done on optically inhomogeneous ensembles via the optically excited state. Papers II and III investigate several aspects relevant to such high-fidelity transfers.

1.3 Outline of this thesis

A primer on the properties of rare-earth-ion-doped crystals that make them attractive for quantum computing is provided in Ch. 2. Subsequent chapters are divided into two main topics, with the common context of rare-earth-ion quantum computing.

Nuclear spin interactions: Ch. 3 develops the concept of nuclear spins, starting from a classical theory point of view and extends to the case of rare-earth-ions. It also gives an overview of the Spin Hamiltonian formalism to describe the behavior of the nuclear spins of the rare-earth-ions in the presence of an external magnetic field. Interactions between the various nuclear spins present in a crystal are also discussed. One such interaction, known as *flip-flops* are the dominant mechanism limiting the lifetime of the nuclear spin states. Paper I develops a new method to model and measure this interaction in rare-earth-ion-doped crystals. The main results of Paper I are described in Ch. 4 .

Coherent control: Ch. 5 gives an overview of the tools for coherent control of ensemble qubits in rare-earth-ions. For quantum computing, the ability to perform gate operations with high fidelity is essential. Ch. 6 describes two methods to achieve this. One is an adiabatic approach, which is the subject of Paper III. This approach is designed to overcome several imperfections in the rare-earth-ion system. The second method is ‘Shortcut to Adiabaticity’, used in Paper II. The main results and some details of both the papers are described in this chapter.

This thesis concludes with an outlook of all the papers and a personal perspective on the progress of this thesis work in Ch. 7.

Chapter 2

Properties of rare-earth-ions

Rare-earth elements are a group of seventeen elements in the periodic table: Scandium (^{21}Sc), Yttrium (^{39}Y), and the lanthanide series of elements from Lanthanum to Lutetium (^{57}La - ^{71}Lu). The Swedish village, Ytterby, has a rich history associated with these elements, with several being mined here for the first time and four even named after it. These elements have a ubiquitous presence in several consumer goods - batteries, lights, computers, DVD players, catalysts in cars and industries - wind turbines, magnets, lasers, fiber optics, superconductors, etc.

Of particular interest to the Quantum Information group in Lund and several other research groups all over the world is their use in quantum technologies [13, 22, 24, 34–43], biomedical imaging [44–49] and laser stabilization [50–54]. When these ions are doped into inorganic crystals, they have hyperfine levels with unique properties such as long lifetimes and coherence times. For example, Eu^{3+} can have a lifetime of more than 49 days [19] and a coherence time of six hours [20], when doped into Y_2SiO_5 . These transitions are easily accessible via optical transitions that are inhomogeneously broadened (up to 100's of GHz) and also possess narrow homogeneous linewidths (≤ 1 kHz). Inhomogeneous broadening and long lifetimes facilitate making, or 'burning' spectral holes in these materials, which means that one can create spectral regions in these materials that are transparent to light. The idea of spectral hole burning in rare-earth-ion-doped crystals for quantum computing was pioneered by Ref. [55] and developed by Ref. [22]. Since then, this field has been explored extensively [17, 18, 21, 56–62].

In this chapter, some of the spectroscopic properties relevant to applications in quantum computing are introduced. These properties can vary for different dopant ions, host crystals, doping concentrations, temperatures, external magnetic fields, etc. First,

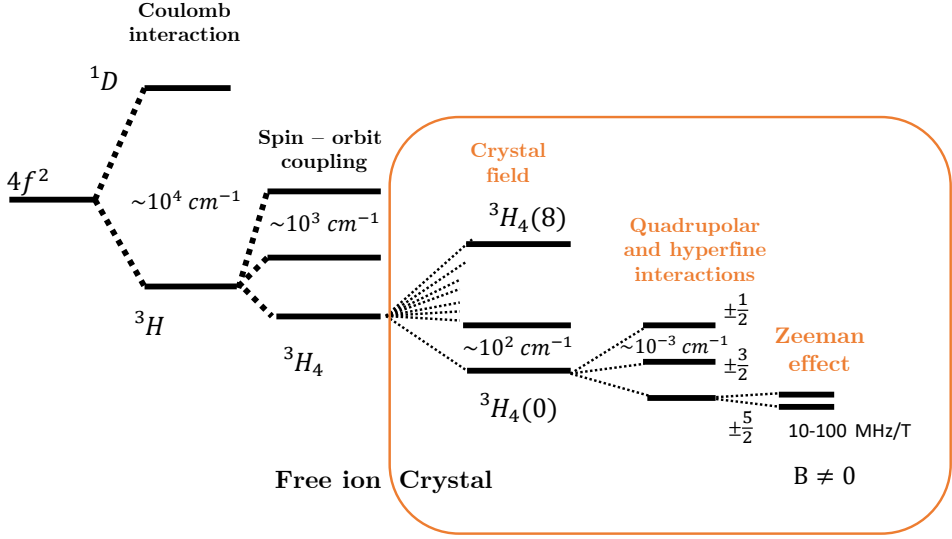


Figure 2.1: Energy levels of Pr^{3+} as a free ion and the splitting of these levels due to different interactions when doped into YSO. The splitting of 3H is shown here as an example. 1D level also has a similar structure.

an overview is given that captures the essence of what makes rare-earth-ions a promising platform for quantum computing. Then, properties specific to Pr^{3+} and Eu^{3+} are given in Sec. 2.5 since they are central to this thesis.

2.1 Energy level structure

The rare-earth (RE) elements considered in this work are trivalent cations of the form RE^{3+} with a configuration of $[\text{Xe}]4f^N$. The value of the principal quantum number n is 4, the angular momentum quantum number l is 3 (corresponds to the f orbital) and N is the number of valence electrons. The ionic radii of all the RE^{3+} ions are similar, facilitating the replacement of one RE^{3+} in an inorganic crystalline host with another RE^{3+} ion. The ions considered in this work are Pr^{3+} and Eu^{3+} . The configuration of Pr^{3+} is $4f^2$, with a ground state 3H_4 , and of Eu^{3+} is $4f^6$, with a ground state 7F_0 (written using the spectroscopic term $^{2S+1}L_J$).

The above ionic energy levels lose their degeneracy completely due to the electric field of the crystal, giving rise to $(2J + 1)$ levels. Nuclear quadrupolar and hyperfine interactions lead to $(2I + 1)/2$ levels. In the presence of an external magnetic field, these levels are further split due to the nuclear Zeeman effect, resulting in $(2I + 1)$ levels.

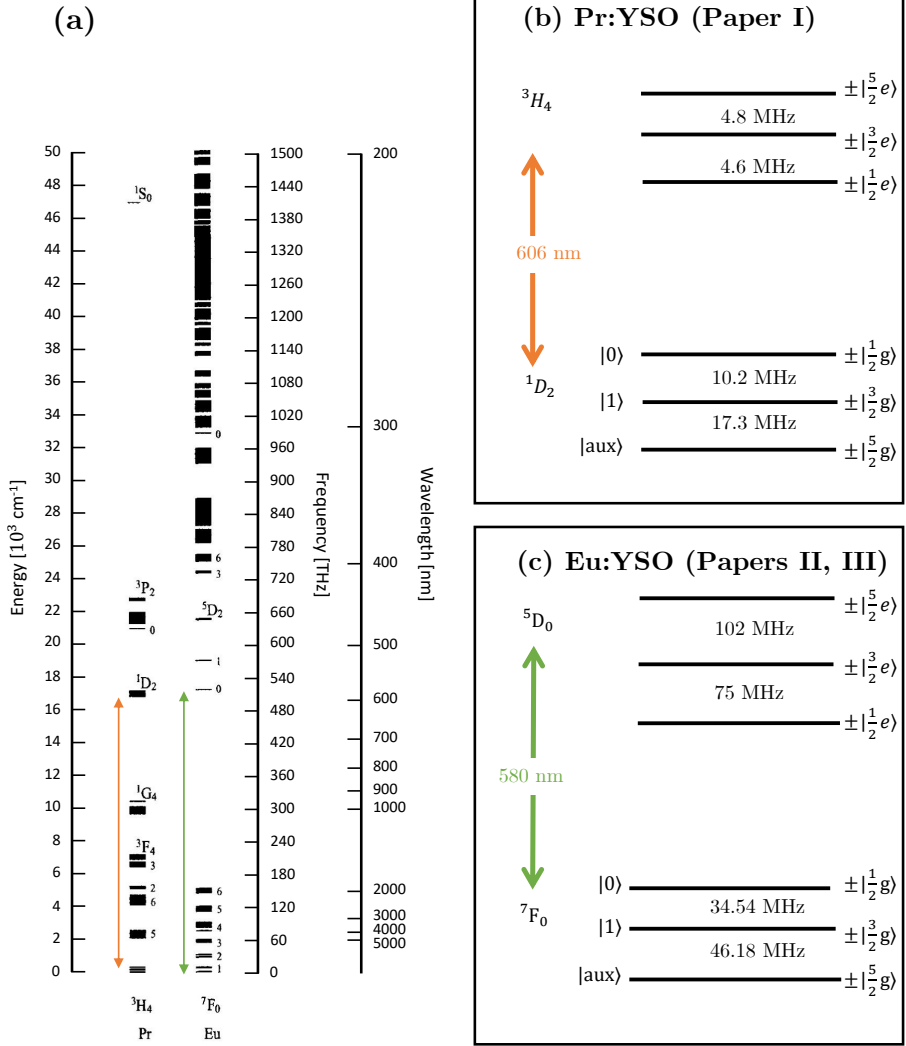


Figure 2.2: (a) Calculated energy level structure of Eu^{3+} and Pr^{3+} , doped in LaF_3 . This image has been reproduced from another reference. See text for details. (b) Hyperfine structure of the lowest crystal field levels in the $^3H_4 - ^1D_2$ transition at 606 nm Pr^{3+} , doped in YSO (c) Hyperfine structure of the lowest crystal field levels in the $^7F_0 - ^5D_0$ transition at 580 nm Eu^{3+} , doped in YSO. For easy conversion between different units : $1 \text{ cm}^{-1} \simeq 1 \text{ K} \simeq 30 \text{ GHz} \simeq 10^7 \text{ nm}$.

A schematic of the interactions and the splitting of energy levels is shown in Fig. 2.1, with Pr^{3+} as an example. For quantum computing, the hyperfine levels $\pm |\frac{1}{2}g\rangle$ and $\pm |\frac{3}{2}g\rangle$ are used as qubits. The qubit states are manipulated via an optically excited state in the 1D level shown in Fig. 2.1, which also has a hyperfine structure similar to 3H .

2.2 Lifetime of hyperfine levels

The transitions considered in this work are electronic transitions within the $4f$ shell. These transitions are not allowed for a free ion since parity is conserved (Laporte rule). However, they become weakly allowed when doped into a crystal since the crystal field mixes the pure $4f$ states. These transitions are also very sharp. The outer-lying $5s$ and $5p$ orbitals are completely filled and shield the $4f$ shell electrons from electric field perturbations due to the crystal field. Additionally, the density of phonons that can contribute to line broadening is drastically reduced when cooled down to 2 K (discussed further in Ch. 4). This leads to long lifetimes of the hyperfine ground states and facilitates persistent spectral hole burning in these materials. In other words, the qubit levels used for quantum computing are long-lived. For example, hyperfine levels in Eu:YSO can have a lifetime T_1 longer than 49 days [19].

The calculated energy level structure of Pr^{3+} and Eu^{3+} doped in LaF_3 is shown in Fig. 2.2(a). This figure is adapted from Ref. [63] and originally from Ref. [64]. This way of representing the energy levels, known as the Dieke diagram, was first used in Ref. [65] and has been modified several times. The transitions used in this work are highlighted, and in Fig. 2.2(b) and (c), the hyperfine structure of the transitions is shown. The optical and hyperfine transitions are inhomogeneously broadened due to the anisotropy of the crystal so that each ion experiences a unique chemical environment [66].

2.3 Homogeneous and Inhomogeneous linewidth

The homogeneous linewidths Γ_h in these materials are narrow. The optical homogeneous linewidth can be in the range of 0.1 Hz-1kHz [67]. Generally, different contributions to the broadening of the homogeneous linewidth are given as [68, 69]:

$$\Gamma_h = \frac{1}{2\pi T_1} + \Gamma_{ISD} + \Gamma_{phonon} \quad (2.1)$$

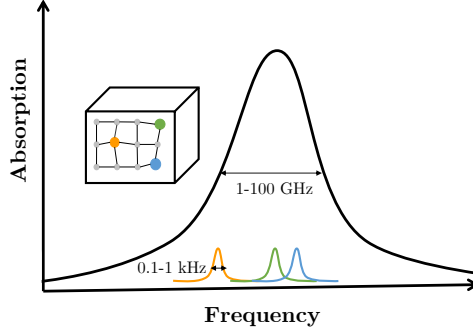


Figure 2.3: The chemical environment around each dopant ion is different, which shifts its resonance frequency, resulting in an inhomogeneous broadening $\Gamma_{inh} \sim 1 - 100$ GHz, apparent when all the ions in the crystal are probed. The homogeneous linewidth of each ion is much narrower, in the range $\Gamma_h \sim 0.1 - 1$ kHz.

where T_1 is lifetime of the optical excited state, Γ_{ISD} is the contribution from instantaneous spectral diffusion effects and Γ_{phonon} comes from temperature-dependent effects due to phonons. Instantaneous spectral diffusion happens due to electric dipole-dipole interactions between dopant ions. When an ion is excited, the static electric dipole moment changes and the resulting change in the electric field around it affects the neighboring dopant ions. Such effects are discussed, for example in Ref. [68, 70]. Phonon-related effects are discussed in Ch.4. The homogeneous linewidth is related to the coherence time T_2 as $\Gamma_h = \frac{1}{\pi T_2}$. Long T_2 is another attractive feature for quantum computing.

The homogeneous linewidth corresponds to a single ion in the crystal. When an ensemble of ions is probed, the inhomogeneous broadening becomes apparent. Since each dopant ion lives in a unique environment in the crystal, the resonant frequencies shift slightly. Inhomogeneous broadening Γ_{inh} can be of the order of $1 - 100$ GHz [67]. This is sketched in Fig. 2.3. The ratio $\frac{\Gamma_{inh}}{\Gamma_h} \sim 10^6$ and this implies that one can potentially access a million qubit channels in one crystal.

The spin homogeneous linewidths can be $< \text{kHz}$. With the application of small magnetic fields, they can be narrowed down by an order of magnitude. For example, Pr^{3+} has a spin coherence time of 0.5 ms, and by applying a modest field of 2 mT, it is increased to 6 ms [71]. By carefully selecting the magnitude and direction of the applied field, it can be further increased to 82 ms [71]. This increase in T_2 happens due to the reduction of the magnetic noise in the host crystal and will be discussed further in Ch.3.

Table 2.1: Spectroscopic properties and relaxation parameters of Pr:YSO (site 1) and ^{151}Eu :YSO (site 1). $T_{1,opt}$ and $T_{2,opt}$ are the lifetime and coherence time for the optically excited level of the transition listed in the first row. $T_{1,spin}$ and $T_{2,spin}$ are the lifetime and coherence time for the spin or hyperfine levels of the ground state for their respective transition. μ_{eg} is the optical transition dipole moment. Γ_{inh} is the inhomogeneous linewidth, given for both the optical and spin transition. α is the absorption coefficient.

Property	Pr:YSO	Eu:YSO
Transition	$^3\text{H}_4(1) \rightarrow ^1\text{D}_2(1)$	$^5\text{D}_0 \rightarrow ^7\text{F}_0$
Wavelength	605.977 nm [69]	579.879 nm [72]
$T_{1,opt}$	164 μs [69]	1.9 ms [72]
$T_{2,opt}$	152 μs [69] (B = 7.7 mT)	1.5 ms [72]
$T_{1,spin}$	~ 100 s [19]	> 49 days [19]
$T_{2,spin}$	0.5 ms [71, 73]	6 hours (B = 1.35 T) [20]
	6 ms [71, 73] (B = 2 mT)	
Oscillator strength	7.7×10^{-7} [74]	1.2×10^{-8} [72]
μ_{eg}	2.5×10^{-32} Cm [74]	6.6×10^{-33} Cm [74]
$\Gamma_{inh,opt}$	4.4 GHz (0.02% conc.) [69]	1.7 GHz (0.1% conc.) [68]
$\Gamma_{inh,spin}$	50 – 75 kHz [75]	30 kHz [76]
α	47 cm^{-1} [66] (along D_2 , 0.05% conc.)	2.7 cm^{-1} (along D_1 , 0.1% conc., measured in Lund)

2.4 Absorption coefficient

Rare-earth-ions doped into crystals are absorbing materials. The spectroscopic studies in this thesis are based on the absorption of the light incident on these crystals. An estimation of absorption can be made using the equation $I = I_0 e^{-\alpha L}$, where I_0 is the light incident on a crystal of length L , α is the absorption coefficient of the crystal and I is the transmitted light after absorption. More absorption is good for the studies in this thesis since higher absorption means higher SNR (Signal-to-Noise Ratio), and more will be discussed in Paper III. The host crystals can be biaxial, so the refractive index and absorption are polarization-dependent. To drive an optical transition, the polarization of the incident light should have a component along the electric transition dipole moment, μ_{eg} . The convention is to give the direction of μ_{eg} and, consequently, the absorption coefficient with respect to the crystal axes D_1, b, D_2 .

2.5 Pr^{3+} and Eu^{3+} doped in YSO

The two ions used in this thesis are Pr^{3+} and Eu^{3+} . The host crystal is Yttrium orthosilicate, Y_2SiO_5 (or YSO for short). This host was chosen because it has outstanding material properties that lead to very narrow homogeneous linewidths of the

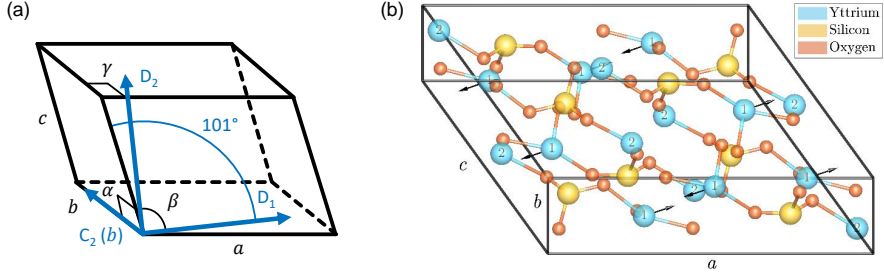


Figure 2.4: (a) Unit cell of Y_2SiO_5 in the C_2/c base-centered group, with $a = 1.44137$ nm, $b = 0.6719$ nm, $c = 1.040$ nm, $\alpha = 90^\circ$, $\beta = 122.235^\circ$, $\gamma = 90^\circ$. (b) Eight basic molecules of Y_2SiO_5 contained in a unit cell, constructed using the atom coordinates from Ref. [77]. Figure taken from Ref. [16].

dopant ions. The most abundant isotopes of Si and O have no nuclear magnetic moments, while Y has a low magnetic moment. This leads to low magnetic noise and preserves the coherence of the rare-earth-ion for longer. Fig. 2.4 shows the structure of the unit cell of YSO [16]. It is monoclinic, biaxial, and the relation between the principal axes a, b, c with the crystal axes D_1, b, D_2 is also shown in the figure. Pr^{3+} or Eu^{3+} replaces either of the Yttrium's labeled as '1' and '2', commonly referred to as site 1 and site 2, respectively. This structure was used to obtain a distribution of the nearest neighbors, as will be discussed later in Paper I.

The reason for choosing Pr^{3+} and Eu^{3+} are discussed below. The oscillator strength of the optical transition is strong enough so that the available laser power is sufficient to control Pr^{3+} ions coherently. Thus, Pr:YSO serves as a good test bed for experiments in many applications for quantum technologies, even though it does not have the longest coherence time. Spectral tailoring techniques in Pr^{3+} are well established in the lab here at Lund. For Paper I, Pr:YSO was chosen to study the hyperfine lifetimes, which is ~ 100 s, and in Paper II, it was chosen to demonstrate a new method to perform population transfers. Eu^{3+} has a very long coherence time which is good for quantum computing, but its transition oscillator strength is weaker than Pr^{3+} by two orders of magnitude. To drive the transitions in Eu^{3+} , pulses designed to work with low Rabi frequency are needed. Several challenges regarding working with Eu^{3+} will be explored in Paper III.

The most relevant properties are listed in Tab. 2.1. In this thesis, 0.05% $\text{Pr}^{3+}:\text{Y}_2\text{SiO}_5$ and isotopically pure 0.1% $^{151}\text{Eu}^{3+}:\text{Y}_2\text{SiO}_5$ were used. For the former, the transition $^3\text{H}_4(1) \rightarrow ^1\text{D}_2(1)$ at 605.977 nm at site 1 was used (Paper I and Paper II), and for

Table 2.2: Experimentally measured values of the relative oscillator strength for Pr:YSO (site 1) [18] and ^{151}Eu :YSO (site 1) [78]

Pr:YSO	$\pm 1/2e\rangle$	$\pm 3/2e\rangle$	$\pm 5/2e\rangle$
$\pm 1/2g\rangle$	0.56	0.38	0.06
$\pm 3/2g\rangle$	0.39	0.60	0.01
$\pm 5/2g\rangle$	0.05	0.02	0.93
Eu:YSO	$\pm 1/2e\rangle$	$\pm 3/2e\rangle$	$\pm 5/2e\rangle$
$\pm 1/2g\rangle$	0.03	0.22	0.75
$\pm 3/2g\rangle$	0.12	0.68	0.20
$\pm 5/2g\rangle$	0.85	0.10	0.05

the latter, $^7F_0 \rightarrow ^5D_0$ at 579.879 nm at site 1 was used (Paper III). The transition $J = 0$ to $J = 0$ is normally forbidden, but when Eu^{3+} is doped in a low symmetry host like YSO, it is weakly allowed due to the mixing of the crystal field levels. This is the reason why 5D_0 has longer lifetimes compared to other rare-earth-ions. For a thorough overview of the spectroscopic properties, the reader is referred to Ref. [66, 68].

The hyperfine structure of Pr:YSO and Eu:YSO shown in Fig. 2.2(b) and (c), respectively, have three levels in the ground and excited state each. The crystal field mixes the levels, so the transition selection rules no longer hold, and there can be nine transitions between these levels. The experimentally measured values of the relative oscillator strengths for the different transitions are given in Tabs.2.2. For Pr:YSO, the values are taken from Ref. [18] but normalized to 1. For Eu:YSO, the values are taken from Ref. [78].

The absorption signal will be proportional to the relative oscillator strengths. For qubit operations, ideally, one should choose two transitions with similar oscillator strengths so that they are equally easy (or difficult) to drive with the available laser power. The excited state should be chosen so that the relative oscillator strength to the third ground state is low so that ions in the ensemble qubit lost to this state during the operations are minimized. Making these considerations, $\pm |1/2g\rangle$ and $\pm |3/2g\rangle$ are chosen as the qubit levels, and the operations are done via $\pm |3/2e\rangle$. In Eu:YSO, the qubit levels are again $\pm |1/2g\rangle$ and $\pm |3/2g\rangle$ while the excited state chosen is $\pm |5/2e\rangle$.

Chapter 3

Nuclear spins and interactions

In this chapter, the behavior of a magnetic dipole in the presence of an external magnetic field is briefly described [79, 80]. The quantum mechanical description of a nucleus with a nuclear spin $I = \frac{5}{2}$ is given. Magnetic dipole-dipole interactions and specifically, flip-flop interactions are also introduced. The general concepts underlying magnetic dipole-dipole interactions date back to the seminal work on relaxation effects in Nuclear Magnetic Resonance (NMR) [81] and the equations can be translated to the case of nuclear spins in rare-earth-ions. These concepts lay the background for Paper I.

3.1 Magnetic dipoles in an external magnetic field

The objective of this section is to describe how a classical magnetic dipole behaves in the presence of an external magnetic field. A very simple description is given but it gives insight into the quantum mechanical description of the nuclear spin levels in rare-earth-ions.

In classical theory, the magnetic dipole moment μ and the angular momentum \mathbf{J} of an object are related as:

$$\mu = \gamma \mathbf{J} \tag{3.1}$$

where γ is a scalar called the ‘gyromagnetic ratio’. It is the ratio of the magnetic moment and the angular momentum. In the presence of an external magnetic field \mathbf{B} , the magnetic dipole experiences a torque given by:

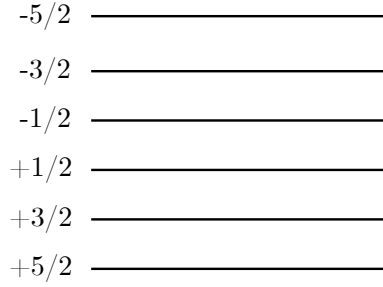


Figure 3.1: Equally spaced energy levels of a system with a nuclear spin $I = 5/2$ according to Eq. 3.7, corresponding to the eigenvalues $m = -5/2, -3/2, -1/2, +1/2, +3/2$, and $+5/2$.

$$\boldsymbol{\tau} = \boldsymbol{\mu} \times \mathbf{B} \quad (3.2)$$

And, the angular momentum vector \mathbf{J} precesses about \mathbf{B} with an angular frequency known as the ‘Larmour frequency’:

$$\omega = \gamma B \quad (3.3)$$

The energy of the dipole (‘Zeeman energy’) is:

$$W = -\boldsymbol{\mu} \cdot \mathbf{B} \quad (3.4)$$

In the quantum mechanical description, the mathematics of angular momentum and spin are very closely related. A dimensionless angular momentum operator \mathbf{I} is used:

$$\mathbf{J} = \hbar \mathbf{I} \quad (3.5)$$

where \hbar is the reduced Planck constant. The components of \mathbf{I} , i.e., I_x, I_y, I_z commute with \mathbf{I}^2 , so one can simultaneously measure one of the components and \mathbf{I}^2 . Thus, their eigen values are good quantum numbers. The eigenvalues of \mathbf{I}^2 and I_z are $I(I + 1)$ and $m = I, I - 1, \dots, -I$, respectively. I can be half-integer or integer. Let us describe the energy of the dipole along one of the directions z . If the field along this direction is B_z , the interaction energy or the Hamiltonian is written as:

$$H = -\gamma \hbar B_z I_z \quad (3.6)$$

The above equation is analogous to Eq. 3.4, where the classical magnetic moment μ has been replaced with the quantum mechanical term $\gamma\hbar I_z$. For $I = \frac{5}{2}$, the eigenvalues of the above Hamiltonian are multiples of the eigenvalues of I_z :

$$E = -\gamma\hbar B_z m \quad (3.7)$$

where $m = -5/2, -3/2, -1/2, +1/2, +3/2$, and $+5/2$ and the levels are equidistant, separated by $\gamma\hbar B_z$. The levels are shown in Fig. 3.1. This splitting of the levels is known as ‘lifting the degeneracy’ of the nuclear spin.

For the rare-earths, the magnetic dipole moment is usually given in units of the nuclear magneton μ_N , defined in SI units as:

$$\mu_N = \frac{e\hbar}{2m_p} \quad (3.8)$$

The value of $\mu_N = 5.05 \times 10^{-27} \text{ JT}^{-1}$. There can sometimes be a ‘ c ’ (speed of light) in the denominator of the above equation, which means that the units are in the CGS system. One should also be cautious with the units of the gyromagnetic ratio γ since it can vary when one navigates through different references (which can sometimes make the life of a new student very enjoyable). In Eq. 3.1, γ was defined as the ratio of the dipole moment and the angular momentum. In SI units, it is expressed as $\text{rads}^{-1}\text{T}^{-1}$ and can also be expressed as $\gamma/2\pi$ in units of MHzT^{-1} . In this thesis, MHzT^{-1} is used.

3.2 Nuclear spins of rare-earth-ions

To go from the classical picture to the quantum picture, we introduced Planck’s constant \hbar and replaced vectors with operators in the previous section. To describe the nuclear spin of a rare-earth-ion, we also need to use tensors since the host crystal can be anisotropic. A 3×3 tensor T is used, where each term is T_{ij} and $i, j = x, y, z$. Thus, there are nine terms: $T_{xx}, T_{xy}, T_{xz}, \dots, T_{zy}, T_{zz}$. Instead of one vector for the magnetic dipole moment μ , there are two tensors \mathbf{Q} and \mathbf{M} , arising from different effects.

The rare-earth-ions considered in this work, Pr^{3+} and Eu^{3+} have a nuclear spin $I = 5/2$. The description below applies to Pr^{3+} , since this is relevant for Paper I. The nuclear spin (or the hyperfine) levels in Pr^{3+} with $m = \pm 1/2, \pm 3/2$ and $\pm 5/2$ result from the second-order hyperfine and nuclear quadrupole interactions [66]. These two interactions can often not be measured independently and

thus are clubbed together in one term, known as the ‘effective quadrupole tensor’, \mathbf{Q} . With an external field, the doubly-degenerate levels split, resulting in levels with $m = +1/2, -1/2, +3/2, -3/2, +5/2, -5/2$. These levels, known as the ‘Zeeman’ levels are not equidistant, as in the simple case of Fig. 3.1. The extent to which the levels are split is governed by the ‘Zeeman’ tensor, \mathbf{M} .

These six hyperfine levels are, in reality, not represented by the pure eigenstates of I_z and they are in fact, a linear combination of the pure eigenstates. This admixture happens due to the mixing caused by the crystal field [66]. Thus, the selection rule $\Delta m_I = \pm 1$ no longer holds and all the transitions between the hyperfine levels are allowed.

3.2.1 Spin Hamiltonian

This section describes the equations used to derive the hyperfine structure, shown in Fig. 2.2(b), given some information on the host crystal parameters. In general, the wavefunctions of the hyperfine levels $|x^i\rangle$ and $|y^j\rangle$ are the eigenstates of the spin Hamiltonian and they depend on the external magnetic field \mathbf{B} , the Zeeman tensor \mathbf{M} and the effective quadrupole tensor \mathbf{Q} . They are calculated using the following equation for the spin Hamiltonian [66, 75, 82].

$$H_{spin} = \mathbf{B} \cdot \mathbf{M} \cdot \tilde{\mathbf{I}} + \tilde{\mathbf{I}} \cdot \mathbf{Q} \cdot \tilde{\mathbf{I}}. \quad (3.9)$$

$\tilde{\mathbf{I}}$ is the vector of nuclear spin operators $\tilde{I}_x, \tilde{I}_y, \tilde{I}_z$ and \mathbf{B} is the magnetic field vector. \mathbf{M} is the effective Zeeman tensor and \mathbf{Q} is the effective quadrupole tensor.

At this point, it is worth mentioning that there are multiple coordinate systems to be considered here. One system corresponds to the crystallographic axes of the crystal $[D_1 D_2 b]$ and forms the common frame of reference for the above calculations. The second is the system corresponding to the principal axis of the host crystal, in which the tensors are diagonalized. Then, there is the lab coordinate system. These systems are often different and some transformations need to be made in the calculations.

The effective Zeeman tensor, \mathbf{M} and the effective quadrupole tensor, \mathbf{Q} are defined as follows:

$$\mathbf{M} = \mathbf{R}_M \begin{bmatrix} g_x & 0 & 0 \\ 0 & g_y & 0 \\ 0 & 0 & g_z \end{bmatrix} \mathbf{R}_M^T = \begin{bmatrix} g_{xx} & g_{xy} & g_{xz} \\ g_{yx} & g_{yy} & g_{yz} \\ g_{zx} & g_{zy} & g_{zz} \end{bmatrix}, \quad (3.10)$$

$$\mathbf{Q} = \mathbf{R}_Q \begin{bmatrix} E - \frac{1}{3}D & 0 & 0 \\ 0 & -E - \frac{1}{3}D & 0 \\ 0 & 0 & \frac{2}{3}D \end{bmatrix} \mathbf{R}_Q^T. \quad (3.11)$$

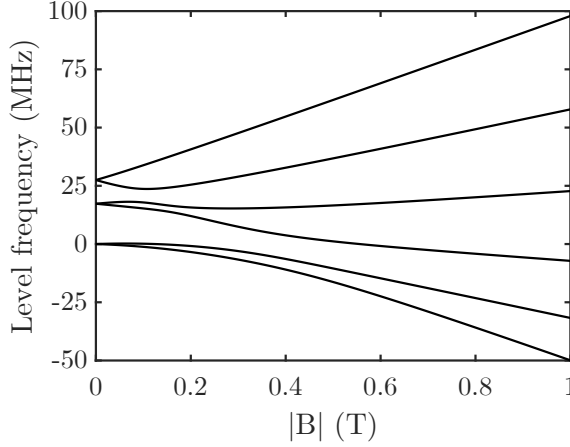


Figure 3.2: Change in the frequencies of the hyperfine levels of the ground state $^3\text{H}_4$ in Pr:YSO (site 1) as the magnitude of the external magnetic field is increased between 0-1 T, along a specific direction. The frequency is plotted as an offset from the lowest hyperfine level, refer to Fig. 2.2(b).

Each of the above matrices is transformed into the frame $[D_1 D_2 b]$ using rotation matrices \mathbf{R} with appropriate Euler angles: $\mathbf{R}_{\mathbf{k}} = R(\alpha, \beta, \gamma)$. The terms g_x, g_y, g_z are the gyromagnetic ratios $\gamma/2\pi$ expressed in units of MHzT^{-1} . The reason it is written as g and not γ here, is because some references use the ‘g-factor’ (a dimensionless constant) as a synonym for the gyromagnetic ratio. I have followed the notations of Ref. [75]. The terms E and D describe the effective quadrupole effect and are also expressed in units of MHzT^{-1} .

The two terms on the right-hand side of Eq. 3.9 are evaluated according to Ref. [80]: $\mathbf{B} \cdot \mathbf{M} \cdot \tilde{\mathbf{I}} = g_{pq} B_p \tilde{I}_q$ and $\tilde{\mathbf{I}} \cdot \mathbf{Q} \cdot \tilde{\mathbf{I}} = Q_{pq} \tilde{I}_p \tilde{I}_q$ where $p, q = x, y, z$ and the usual summation rules are to be observed whenever a suffix occurs twice. This notation omits summation signs and since the suffix p appears twice, a summation over p is implied. Note that in this thesis work, the summation is implied only for the suffix and not for the superscripts. Since q appears once, it can take one of the values x, y, z . For example, if $\mathbf{B} = B_z$, the following terms are summed: $\mathbf{B} \cdot \mathbf{M} \cdot \tilde{\mathbf{I}} = g_{zx} B_z \tilde{I}_x + g_{zy} B_z \tilde{I}_y + g_{zz} B_z \tilde{I}_z$.

The levels $\pm |\frac{1}{2}g\rangle$, $\pm |\frac{3}{2}g\rangle$ and $\pm |\frac{5}{2}g\rangle$ lose their degeneracy in the presence of a field due to the Zeeman effect. In other words, a peak of an ensemble of ions prepared in one of the states splits. The effect of an external magnetic field on the hyperfine levels of the ground state $^3\text{H}_4$ in Pr:YSO has been studied in another work, Ref. [83].

Table 3.1: Parameters for the spin Hamiltonian in Eq. 3.9, for the ground state $^3\text{H}_4$ in Pr:YSO (site 1). Taken from Ref. [75]

Parameter	Value
D	-4.4435 MHz
E	-0.56253 MHz
α_Q	62.1°
β_Q	31.81°
γ_Q	93.94°
g_x	26.57 MHzT ⁻¹
g_y	31.01 MHzT ⁻¹
g_z	113.08 MHzT ⁻¹
α_M	112.0°
β_M	35.68°
γ_M	101.54°

As a sanity check that the code used in Paper I was correct, a result from Ref. [83] was reproduced. A field was applied in a specific direction: [-0.81, 0.16, 0.56] along the crystal axes $[D_1 D_2 b]$ with a magnitude between 0-1 T. The result is plotted in Fig. 3.2 and matches well with Fig. 4 in Ref. [83]. The spacing between the levels is different for a given value of the external field. This figure can be qualitatively compared with the simple case in Fig. 3.1, where the levels were equally spaced for a given value of the external field.

The equations described in this section are used in Paper I for the calculation of the wavefunctions of the hyperfine levels of the ground state $^3\text{H}_4$ in Pr:YSO. The values of all the parameters above were taken from Ref. [75] and are listed in Tab. 3.1. In Paper I, the field applied is only 10 mT (albeit along a different direction) and thus, the hyperfine levels do not split much.

3.2.2 Dipole-dipole interactions

From classical theory, the energy of interaction between two point magnetic dipoles ' μ^i ' and ' μ^j ' separated by a distance \mathbf{r}^{ij} ¹[80] is:

$$W^{ij} = \frac{\mu_0}{4\pi} [\mu^i \cdot \mu^j - 3(\mu^i \cdot \hat{\mathbf{r}}^{ij})(\mu^j \cdot \hat{\mathbf{r}}^{ij})] \frac{1}{|\mathbf{r}^{ij}|^3} \quad (3.12)$$

For the equivalent in quantum theory, the Hamiltonian H_{dd}^{ij} for magnetic dipole-dipole interaction between an anisotropic magnetic dipolar ion ' i ' and its neighbor ' j '

¹Note that summation is not implied for the superscripts which occur twice.

can be written by introducing the customary Planck's constant and using the operator form for nuclear spins as $\boldsymbol{\mu}^i = g^i \hbar \tilde{I}^i$ and $\boldsymbol{\mu}^j = g^j \hbar \tilde{I}^j$ [79, 80, 84]:

$$H_{dd}^{ij} = \frac{\mu_0 \hbar^2}{4\pi} \tilde{I}_p^i \tilde{I}_q^j \{ g_{ps}^i g_{qs}^j - \frac{3 \mathbf{r}_s^{ij} \mathbf{r}_t^{ij}}{|\mathbf{r}^{ij}|^2} g_{ps}^i g_{qt}^j \} \frac{1}{|\mathbf{r}^{ij}|^3} \quad (3.13)$$

where $\tilde{\mathbf{I}}$ is the vector of nuclear spin operators $\tilde{I}_x, \tilde{I}_y, \tilde{I}_z$ and g_{xy} are components of the effective Zeeman tensor (related to nuclear magnetic moment) in MHzT^{-1} (Equivalent to $\gamma \hbar$ in Eq. 3.7). Each of the subscripts p, q, s, t takes the values x, y, z and is introduced to account for the anisotropy of the magnetic dipoles. The summation rules are to be observed whenever a suffix occurs twice.

To glean more information from Eq. 3.13, it can be expanded and written in terms of the direction cosines of \mathbf{r} , (l, m, n) [80]:

$$H_{dd}^{ij} = \frac{\mu_0 \hbar^2}{4\pi} \left\{ (1 - 3l^2) g_x^i g_x^j I_x^i I_x^j + (1 - 3m^2) g_y^i g_y^j I_y^i I_y^j + (1 - 3n^2) g_z^i g_z^j I_z^i I_z^j \right. \\ \left. - 3lm (g_x^i g_y^j I_x^i I_y^j + g_y^i g_x^j I_y^i I_x^j) - 3mn (g_y^i g_z^j I_y^i I_z^j + g_z^i g_y^j I_z^i I_y^j) \right. \\ \left. - 3nl (g_z^i g_x^j I_z^i I_x^j + g_x^i g_z^j I_x^i I_z^j) \right\} \frac{1}{|\mathbf{r}^{ij}|^3} \quad (3.14)$$

The above equation can be re-arranged, so it becomes more suggestive of what happens to the spin state [79, 81]. Using the ladder operators² $I_+ = (I_x + iI_y)$ and $I_- = (I_x - iI_y)$ and dropping the constants, there are five terms :

$$\begin{aligned} A &\propto I_z^i I_z^j \\ B &\propto (I_+^i I_-^j + I_-^i I_+^j) \\ C &\propto (I_+^i I_z^j + I_z^i I_+^j) \\ D &\propto (I_-^i I_z^j + I_z^i I_-^j) \\ E &\propto (I_+^i I_+^j) \\ F &\propto (I_-^i I_-^j) \end{aligned} \quad (3.15)$$

²Note the difference in the imaginary unit i and superscript i for the ion index.



Figure 3.3: A representation of the flip-flop interaction between two ions ‘i’ and ‘j’, with two levels $|x\rangle$ and $|y\rangle$.

One of the terms above, B , is responsible for a ‘flip-flop’ process. In a spin $\frac{1}{2}$ system consisting of two isotropic spins \mathbf{m}^i and \mathbf{m}^j , the flip-flop term connects the state $|\mathbf{m}^i, \mathbf{m}^j\rangle$ to $|\mathbf{m}^i + 1, \mathbf{m}^j - 1\rangle$ or $|\mathbf{m}^i - 1, \mathbf{m}^j + 1\rangle$. Thus, one spin flips up, and the other spin flips down simultaneously. This term is central to Paper I, where flip-flop interactions in rare-earth-ions are modeled. Such an interaction is represented in Fig. 3.3 between two ions ‘i’ and ‘j’, with two levels $|x\rangle$ and $|y\rangle$.

3.2.3 Decoherence from magnetic interactions

YSO is considered a good crystal host since it has low magnetic noise that can cause decoherence of the qubit. Magnetic noise comes from the nuclear spins of the host ions. Any species in the crystal with a nuclear spin has a magnetic field around it and can influence the state of the qubit ion, Pr. If the spin state changes for any reason, the magnetic field fluctuates, creating magnetic noise. As mentioned in Sec. 2.5, silicon (Si) and oxygen (O) do not have a nuclear spin. Yttrium (Y) has a nuclear spin $\frac{1}{2}$, and a low magnetic moment of $-0.13\mu_N$ while Praseodymium (Pr) is much stronger with a magnetic moment of $4.59\mu_N$ [85].

Magnetic dipole-dipole interactions between Y-Y and Pr-Y can lead to the decoherence of the spin state of Pr, and interactions between Pr-Pr change their spin states. The topic of decoherence due to magnetic dipole-dipole interactions has been widely explored in several references [20, 71, 76, 86–88] and is only briefly described here. In the absence of an external field, the magnetic field experienced by the core Y ions is due to the local Pr ion, which is of the order of ~ 0.1 mT and a change in the spin state of Pr flips the spin state of Y ions. Thus, the dephasing of Pr ions is dominated by neighboring Y ions in the core. When the external field significantly exceeds the field due to the local Pr ion, such flips are minimized, leading to the narrowing of the homogeneous linewidth. By applying an external magnetic field with a specific magnitude and in a specific direction, the Zeeman-shift (see Eq. 3.9) can vanish up to the first order. This drastically reduces the magnetic interactions between Pr and Y, resulting in an increase in coherence time by two orders of magnitude [71].

Chapter 4

Relaxation of nuclear spins of rare-earth-ions

This chapter concerns the mechanisms by which the nuclear spins embedded in a crystal relax to other nuclear spin states. The mechanisms responsible for relaxation can occur via lattice vibrations mediated by phonons (spin-lattice relaxation) or via interactions with neighboring spins (spin-spin relaxation). First, the types of spin-phonon relaxation are briefly described, and then the focus of the chapter shifts to a type of spin-spin interaction known as ‘flip-flops’, which is the crux of Paper I. This interaction is primarily responsible for the relaxation of Pr ions at 1.7 K in the presence of a low magnetic field.

4.1 Spin-lattice relaxation

Spin-lattice relaxation processes are well understood, and the related theory coupled with experimental verification has been described in detail in many other texts [89–91]. Here, these processes are briefly described since flip-flop interactions dominate the relaxation processes in Paper I. There are three main spin-lattice relaxation processes to consider here:

- *Direct*: It involves a single phonon resonant with the energy separation between the hyperfine levels. The rate due to this process scales linearly with temperature and shows a strong dependence on the magnitude and the direction of the magnetic field ($\propto B^2$ in non-Kramers ions and $\propto B^4$ in Kramers ions).

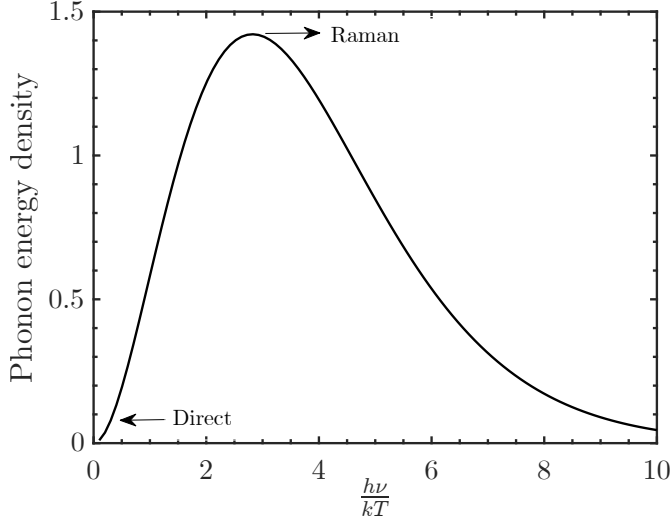


Figure 4.1: Energy density of phonons as a function of $\frac{h\nu}{kT}$, adapted from Ref. [80]. For the *direct* process, $h\nu \ll kT$ and thus much fewer phonons are available than those at higher frequencies for the Raman process.

- *Raman*: This is a two-phonon process strongly dependent on temperature, and its rate is proportional to T^7 in non-Kramers ions and T^9 in Kramers ions.
- *Orbach*: This is also a two-phonon process with a phonon resonance with a crystal-field splitting ' Δ ' between the first excited crystal-field level above the ground state, and its rate is proportional to $e^{-\Delta/kT}$.

In some cases, the *Direct* process can be '*phonon - bottlenecked*' due to the lack of sufficient phonons at the required frequency, thus making the transfer of heat from the spins to the bath slower. In this case, the rate increases quadratically with temperature ($\propto T^2$).

The energy density of phonons, given by the Debye model, is proportional to $\frac{x^3}{(e^x - 1)}$, where $x = \frac{h\nu}{kT}$ and this is plotted in Fig. 4.1. This function peaks at $\frac{h\nu}{kT} = 3$. So, for a given temperature, the maximum density of phonons corresponds to the frequency $\frac{3kT}{h}$. At 2 K, this is ~ 130 GHz. The next crystal field level is $\sim 100\text{cm}^{-1}$ or 3000 GHz away in Pr^{3+} , see Fig. 2.2(a). The hyperfine levels are ~ 10 MHz so, the *Direct* process governs the relaxation at liquid helium temperatures, where $h\nu \ll kT$. As the temperature increases, the two-phonon processes begin to dominate since they scale faster with temperature. The entire phonon spectrum is available for the Raman process at high temperatures. This is the reason why experiments in rare-earth-ions are

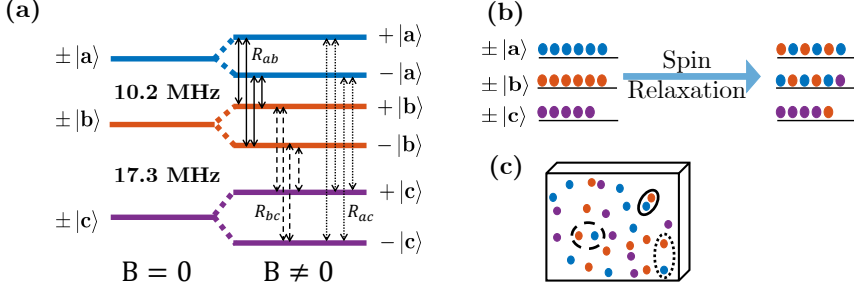


Figure 4.2: Representation of spin relaxation via flip-flop interactions in $\text{Pr}^{3+}:\text{Y}_2\text{SiO}_5$, whereby two neighboring ions interchange their state. (a) Ground state hyperfine levels $\pm|a\rangle$, $\pm|b\rangle$, $\pm|c\rangle$ lose their degeneracy in the presence of an external magnetic field B , forming six levels. The pathways considered for spin relaxation in our simulations are shown with double-sided arrows. (b) Ions occupying $\pm|a\rangle$ and $\pm|b\rangle$ flip-flop strongly with each other, while those in $\pm|c\rangle$ share weak interaction with either of the other hyperfine levels. (c) The interaction strength varies with distance r as r^{-6} , so closely-lying neighbors in the crystal can rapidly flip-flop (shown as solid oval) while ions separated by larger distances share weaker interaction (shown as dashed and dotted ovals).

done below liquid helium temperatures. Overall, the density of phonons in the entire spectrum shoots up at room temperature, making it quite difficult to burn spectral holes.

Spin dynamics of Pr^{3+} in various hosts like LaF_3 [92], LaCl_3 [93], YAlO_3 [94] and YSO [95] has been studied but the focus of these studies has been on spin-lattice relaxation. The general conclusion from these references is that the relaxation is dominated by temperature-independent Pr-Pr flip-flops at ~ 2 K while the Orbach process is thermally activated at higher temperatures (See Sec. 3.2.2 for a description on flip-flop interactions). Modeling of this mechanism has so far been macroscopic, characterized by an average rate describing the relaxation of all ions. In Paper I, a microscopic model of flip-flop interactions is presented, where the interaction is calculated between individual nuclear spins of dopant ions. In the next section, spin relaxation due to flip-flops is described.

4.2 Relaxation via flip-flops

Interactions between Pr-Pr ions are known as ‘flip-flop’ processes whereby two neighboring Pr ions exchange their spins via magnetic dipole-dipole interaction, introduced in Sec. 3.2.2. Pr^{3+} is a spin $\frac{5}{2}$ system with three hyperfine levels in the electronic

ground state 3H_4 , as shown in Fig. 4.2(a). Each hyperfine level is doubly degenerate but the degeneracy is lost in the presence of an external magnetic field, giving rise to six levels in total. It should be noted that conventional labels for the hyperfine levels are $\pm |\frac{1}{2}g\rangle$, $\pm |\frac{3}{2}g\rangle$, $\pm |\frac{5}{2}g\rangle$, but each level is, in reality, an admixture of all six hyperfine wave functions. So I instead use the labels $\pm |a\rangle$, $\pm |b\rangle$, $\pm |c\rangle$. Fifteen unique flip-flop transitions are expected for six levels, but some rates were summed and averaged such that only three effective rates, R_{ab} , R_{bc} and R_{ac} were obtained for each ion ‘ i ’. The details of reducing fifteen rates down to three are described in Paper I. The experiments in Paper I showed that the strongest interaction is between ions occupying $\pm |a\rangle$ and $\pm |b\rangle$ (indicated by solid double-sided arrows), while $\pm |c\rangle$ couples weakly to the other two levels (indicated by dashed and dotted double-sided arrows). Ions initialized in $\pm |a\rangle$ and $\pm |b\rangle$ flip-flop strongly to give somewhat mixed populations (blue and red circles shown in Fig. 4.2 (b)) while ions in $\pm |c\rangle$ (purple circles) flip-flop with either of the other two levels with less likelihood. Fig. 4.2(c) visualizes that the interaction strength decreases with distance. Thus, closely-lying neighbors in a crystal interact strongly (shown as solid oval) while ions far away from each other show weaker interaction (shown as dashed and dotted ovals).

4.3 Modeling of flip-flops

Flip-flop transition rates have traditionally been calculated or modeled using Fermi’s Golden Rule (FGR), following the work by Bloembergen *et al.* [96]. More recent studies in Kramers ions like Er^{3+} and Nd^{3+} have used a macroscopic model to explain spectral hole decay due to flip-flop process by taking a single average rate to be related to the dopant concentration [97] and an average ion-ion distance for the ions in the crystal [98], resulting in a rate $R \propto \frac{n^2}{\langle r \rangle^6}$. However, experiments measuring flip-flop rates in Paper I did not show an exponential decay and a macroscopic model could not be employed to explain the data. As pointed out earlier, non - exponential decay has also been measured in Pr:YSO previously [95], a possible explanation provided by the authors was that not all ions relax at the same rate since flip-flop rates are position-dependent. This effect has not been modeled before in rare-earths and this is where the novelty of Paper I lies. Contributions from all its ‘ j ’ neighbors should be summed and thus the flip-flop rate for ion ‘ i ’ is $R^i \propto \sum_j \frac{1}{r^6}$. This is represented in Fig. 4.3.

Non-exponential decay resulting from flip-flops has also been observed in other fields of research involving spins. Nuclear spin of ^{31}P shows a so-called ‘stretched - exponential’ decay due to spin flip-flops of neighboring ^{29}Si [99]. Spin-polarized muons, which are used as probes to detect local magnetic fields in matter, can show non - exponential decay of polarization [100–102]. The physics involved in this field of research is closely related to Nuclear Magnetic Resonance (NMR) and similar to spin

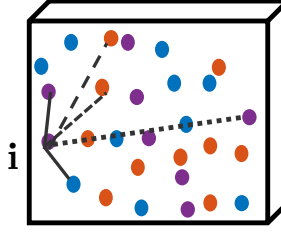


Figure 4.3: An ion ‘i’ can interact with any of its neighbors ‘j’. Depending on the relative orientation and distance to its neighbor, the interaction can be strong (shown as solid lines) or weak (shown as dashed and dotted lines). Contributions from all its ‘j’ neighbors should be summed and thus the flip-flop rate for ion ‘i’ is $R^i \propto \sum_j \frac{1}{r^{6j}}$.

dynamics in RE systems. The polarization of a muon depends on the local magnetic field due to a magnetic species located at different distances from it. This effect can be modeled as an averaged sum of decay due to every magnetic neighbor [102] or as a ‘root - exponential’ of the form $e^{-\sqrt{Rt}}$ [100, 101] in the limit of low concentration of magnetic species. Paper I adopts a model similar to the former approach and uses Fermi’s Golden Rule (FGR) to calculate the flip-flop rates.

4.3.1 Validity of Fermi’s Golden Rule (FGR)

Fermi’s Golden Rule can only be applied in the perturbative limit, implying that $H_{dd} \ll \mathbf{B} \cdot \mathbf{M} \cdot \mathbf{I}$, where H_{dd} is the magnetic dipole-dipole interaction (see Eq. 3.13), $\mathbf{B} \cdot \mathbf{M} \cdot \mathbf{I}$ is the Zeeman term in the spin Hamiltonian, H_{spin} , \mathbf{B} is the external magnetic field, \mathbf{M} is the effective Zeeman tensor, and \mathbf{I} is the vector of nuclear spin operators (see Eq. 3.9). Since $\mathbf{M} \sim 10\text{--}100 \text{ MHz T}^{-1}$ [75], $H_{spin} \sim 10 - 100 \text{ kHz}$ in the presence of a magnetic field $\sim 1 \text{ mT}$. To estimate how large H_{dd} can be, one can look at the magnitude of the interaction H_{dd} between the two nearest Pr ions in any of these states assuming that the hyperfine wavefunctions $\pm |a\rangle$, $\pm |b\rangle$ and $\pm |c\rangle$ are composed of pure $\pm |\frac{1}{2}g\rangle$, $\pm |\frac{3}{2}g\rangle$ and $\pm |\frac{5}{2}g\rangle$ states. Fig. 4.4 shows the distribution of distances between a Pr ion and its first nearest neighbor in a crystal doped with 0.05% concentration (left) and the magnitude of interaction corresponding to three distances $r_1 = 1 \text{ nm}$, $r_2 = 7.5 \text{ nm}$ and $r_3 = 4 \text{ nm}$ (right). These values are chosen as representative values to show how large the interaction can be depending on the separation. Most ions are separated by a distance r_3 while very few ions are separated by r_1 and r_2 . For a given distance, the interaction is proportional to the quantum number $m_I = \frac{1}{2}, \frac{3}{2}, \frac{5}{2}$, i.e., $H_{dd} \propto m_I^i m_I^j$. Thus, the interactions are strongest between ions with $m_I^i = m_I^j = \frac{5}{2}$. If ions are separated by $r_1 = 1 \text{ nm}$, the interaction can be as large as 1 kHz. But, most of the nearest neighbors are located at $r_3 = 4$

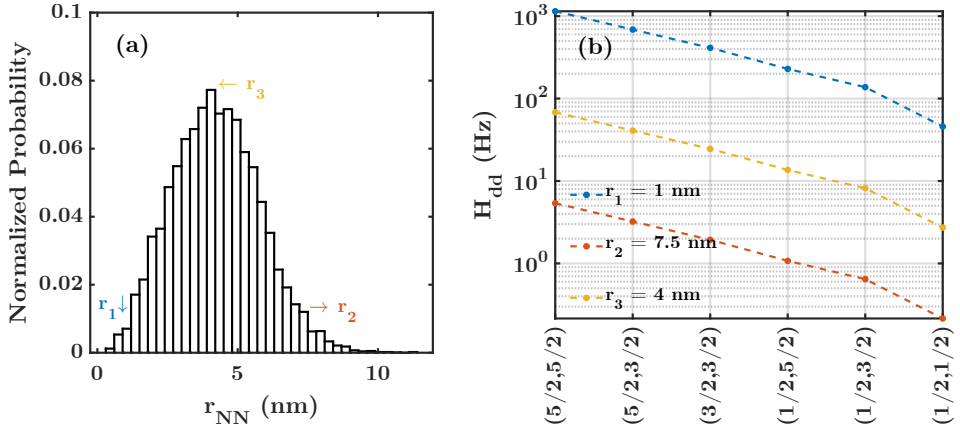


Figure 4.4: (a) Distribution of distances between the first nearest Pr ions in a crystal doped with 0.05% concentration. As representative values, three distances are marked as r_1, r_2, r_3 . (b) The magnitude of interaction as a function of the nuclear spin quantum number m_I of two Pr ions, separated by three values of distances marked as r_1, r_2, r_3 in (a).

nm, where the interaction can vary between 2 - 70 Hz, depending on the value of m_I . This is small compared to H_{spin} , given above, which confirms that we are in the perturbative limit.

It should be noted that solving the full Hamiltonian for the system including all interacting ions is the more valid approach. However, since each ion has six ground levels, directly solving this would require a system with the size of $6^{21} \approx 10^{16}$, which is impossible. Therefore, simplifications must be made. A possible approach would be to solve the case for just the nearest neighbor, then the two closest neighbors etc., and then try to extrapolate from there. This is however not the approach we have chosen for this work. Furthermore, we attempt to study the flip-flop rate of a bulk crystal in a microscopic manner, and since each ion has a unique local environment, we must perform several thousand studies in order to build statistics to get a truthful representation of all the different ions in the crystal.

4.3.2 Microscopic modeling

Having justified the use of FGR, the steps involved in calculating the flip-flop rates for any RE ion are now described:

- i. A small sphere of a host crystal is simulated, where ions are placed according to the crystal lattice structure [77]. It is then randomly doped with a rare-earth

ion with the specified concentration. Alternatively, one could also assume a continuous random distribution function of ions to determine the position of the nearest N^{th} neighbor [103]. More details about modeling the host crystal can be found in Ref. [16]. An ion ‘ i ’ is picked in the sphere and the nearest neighbors ‘ j ’ are found. Nuclear wave functions $|a^i\rangle \dots |c^i\rangle$ and $|a^j\rangle \dots |c^j\rangle$ are calculated to be eigenstates of the spin Hamiltonian H_{spin} and depend on the orientation of the ion in the crystal and the magnetic field.

2. The dipole-dipole interaction Hamiltonian for ion ‘ i ’ due to interaction with neighbors ‘ j ’ is calculated according to Eq. 3.13.
3. The flip-flop rate for any ion ‘ i ’ to flip from a hyperfine state $|x\rangle$ to $|y\rangle$ due to interactions with all its ‘ j ’ neighbors initially in the state $|y\rangle$ is then calculated using Fermi’s Golden Rule (FGR):

$$R_{|x\rangle \rightarrow |y\rangle}^i = \frac{2\pi}{\hbar} \sum_j |\langle y^i \otimes x^j | H_{dd}^{ij} | x^i \otimes y^j \rangle|^2 f(E) \quad (4.1)$$

$|x^i\rangle$ and $|y^j\rangle$ are the eigenstates of the spin Hamiltonian and depend on the external magnetic field \mathbf{B} . They are calculated as described in Ref. [75]. $f(E)$ is the density of initial and final states for transitions between two levels in the continuum of initial and final states $|x^i\rangle \otimes |y^j\rangle$ and $|y^i\rangle \otimes |x^j\rangle$ respectively. The form of density of states used here is:

$$f(E) = \frac{1}{\pi\hbar} \frac{\Gamma_{hom}(\mathbf{B})}{\Gamma_{hom}^2(\mathbf{B}) + [\kappa_{xy}(\mathbf{B})\Gamma_{xy}]^2} \quad (4.2)$$

where Γ_{hom} and Γ_{xy} are the homogeneous and inhomogeneous linewidths of the transition $|x\rangle \leftrightarrow |y\rangle$. Γ_{hom} is a function of external magnetic field \mathbf{B} , and $\kappa_{xy}(\mathbf{B})$ is a phenomenological addition to describe the increase in inhomogeneous linewidths in the presence of a magnetic field. When $\mathbf{B} = 0$, $\kappa_{xy} = 1$ and when $\mathbf{B} \neq 0$, κ_{xy} is some multiplicative factor.

It is worth noting that calculation of the matrix elements $|\langle y^i \otimes x^j | H_{dd}^{ij} | x^i \otimes y^j \rangle|$ for all the pairs of ions makes this model ‘microscopic’, setting it apart from previous similar works, where this was taken as an average value and related to the concentration of dopants in Refs.[97, 98] Also, the form of density of states $f(E)$ used in previous works [97, 98], accounted for the inhomogeneous linewidth only. If only single ions were considered (in a fully microscopic model), the flip-flop interaction

will be limited by the homogeneous linewidth since Γ_{xy} would be zero. A derivation of the form used here is given in an appendix of Paper I.

Two conditions need to be satisfied for two Pr ions to flip-flop: they need to be close to each other spatially in the crystal and they also need to be spectrally close in the spin inhomogeneous profile. The term H_{dd} , which is a function of the distance between ions captures the first condition and $f(E)$ captures the second condition.

In $\text{Pr}^{3+}:\text{Y}_2\text{SiO}_5$, only the ions in site 1 corresponding to the $^3H_4 \rightarrow ^1D_2$ transition at 606 nm were used. The radius of the sphere used was 100 nm, and the flip-flop rate of ion ‘ i ’ was calculated due to the interaction with its twenty nearest neighbors. Since Pr^{3+} has a nuclear spin $\frac{5}{2}$, $\tilde{\mathbf{I}}$ is a (3×1) vector where each element is a (6×6) matrix. The magnetic field was directed along the crystal axis b . Homogeneous linewidths $\Gamma_{hom}(\mathbf{B}) = \frac{1}{\pi T_2}$ were taken from Refs.[71, 73] where the spin coherence time T_2 was measured to be 0.5 ms with zero magnetic field and 6 ms in the presence of a magnetic field of 2 mT. The model contains six unknowns used in the density of states $f(E)$. Three of these are the inhomogeneous spin linewidths $\Gamma_{ab}, \Gamma_{bc}, \Gamma_{ac}$, and the other three are the factors describing their dependence on the magnetic field $\kappa_{ab}, \kappa_{bc}, \kappa_{ac}$.

4.4 Measuring flip-flops

Relaxation between spin levels has been measured using methods that combine optical spectral hole burning and RF fields resonant with a hyperfine transition [92–94]. Another method extracts rate constants for individual transitions using only hole-burning spectra [104] but it requires many fitting parameters for each rate equation to be able to keep track of the initial population of any ion that was excited during the hole-burning. For example, since Pr:YSO has three hyperfine levels in the ground and excited states, a laser at a single frequency on the $^3H_4 \rightarrow ^1D_2$ transition can excite nine different transitions or classes of ions due to the optical inhomogeneous broadening. To extract the rates for the three individual transitions, the method in Ref. [104] requires 21 independent fitting parameters (18 initial spin populations and 3 rates).

The experimental method in Paper I uses spectral hole burning only and significantly reduces the number of fitting parameters by tailoring the spectral window to isolate some ions. First, a transmission window using optical pumping and spectral tailoring techniques was created (see Sec. 5.2). After that, the population was initialized in one of the ground state hyperfine levels within a spectral region of 1 MHz inside the window (see Sec. 5.2). The decay of this state-specific hyperfine population versus its

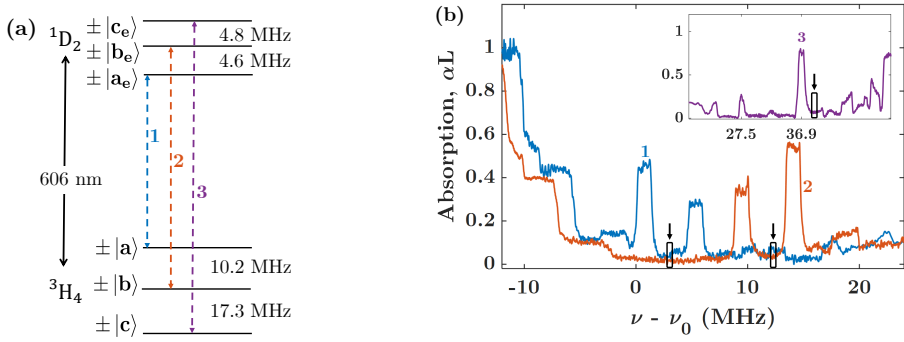


Figure 4.5: Hyperfine energy levels in $\text{Pr}^{3+}:\text{Y}_2\text{SiO}_5$ corresponding to the $^3H_4 \rightarrow ^1D_2$ transition at 606 nm and the absorption spectrum obtained from the experiments. (a) Transitions used for evaluating population decay in this experiment are labeled as ‘1’, ‘2’, ‘3’ (b) Absorption spectrum after initializing the population in $\pm |a\rangle$ (blue), $\pm |b\rangle$ (red) and $\pm |c\rangle$ (inset, purple). Peaks labeled as ‘1’, ‘2’, ‘3’ correspond to the transition shown in (a). An absorption region of width ~ 1 MHz is selected as the background for each of the peaks. These are marked with black arrows at 2 MHz, 12.2 MHz, and 38.9 MHz.

neighboring spectral background was tracked. The experiments were also repeated in the presence of an external magnetic field in the range 5 - 10 mT, directed along the crystal axis b . This method can be advantageous for measurements in rare-earth-ions with more than one ground hyperfine level, where populations of many classes of ions need to be tracked.

All the experiments were done in a $\text{Pr}^{3+}:\text{Y}_2\text{SiO}_5$ crystal with 0.05% concentration and dimensions 10mm x 10mm x 0.8mm along D_1, D_2, b axes respectively. The experimental setup used is described in Paper I. Transitions used for evaluating the population and an example of the absorption structure after the initialization process within a 1 MHz region are shown in Fig. 4.5. The optical transitions labeled as ‘1’, ‘2’, and ‘3’ were used to evaluate the population. Three spectra in blue, red, and purple (inset) show the absorption spectrum after initializing ions in $\pm |a\rangle, \pm |b\rangle$ and $\pm |c\rangle$, respectively. Background absorption level is indicated with black arrows at 2 MHz, 12.2 MHz, and 38.9 MHz. The pulse sequence used for creating the transmission window and population initialization and other experimental details are described in Paper I.

4.4.1 Experimental results

The results of population decay are shown in Fig. 4.6. The figures show the experimental data with error bars indicating the weighted standard deviation of three data sets taken for decay after initializing the populations in each hyperfine level $\pm |a\rangle$

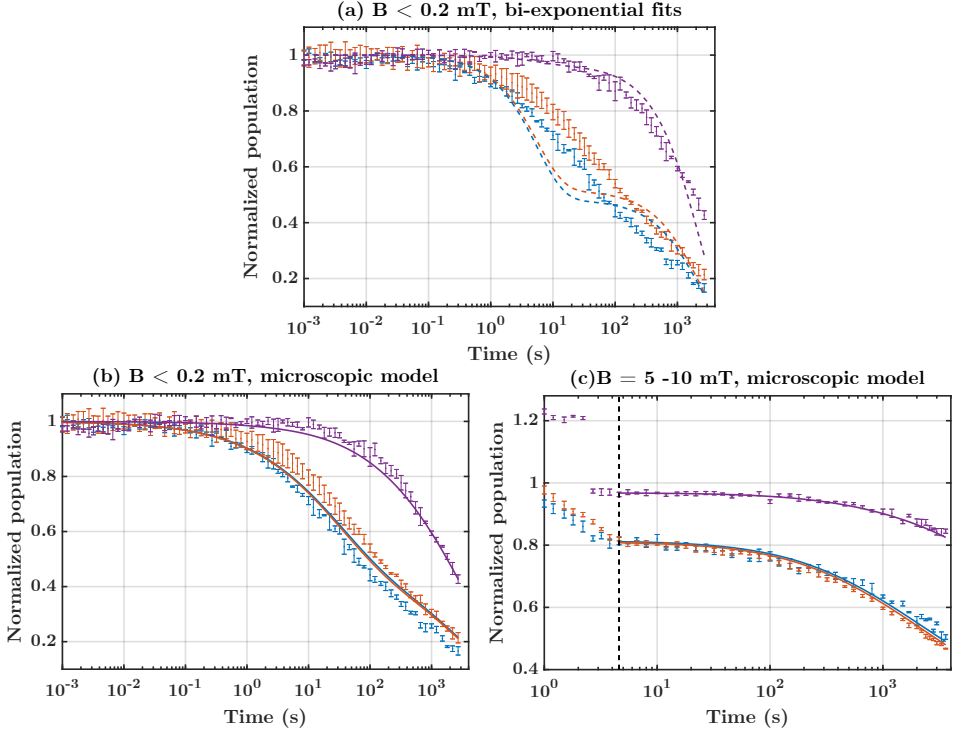


Figure 4.6: Population decay of three ground states is shown in three colors: $\pm |a\rangle$ in blue, $\pm |b\rangle$ in red, and $\pm |c\rangle$ in purple. The experimental data are shown with error bars. (a)) The dashed lines are the best bi-exponential fits. (b) The solid lines are the result of simulation using the microscopic model from Paper I. (c) Experimental data and microscopic model simulations with an external field of 5-10 mT. The vertical dashed black line shows the time t_0 at which \vec{B} is reached after turning it on.

(blue), $\pm |b\rangle$ (red) and $\pm |c\rangle$ (purple). There was no external magnetic field applied in (a) and (b) but previous measurements indicate that there is a residual field < 0.2 mT in the cryostat. To demonstrate the problems with a macroscopic model, the previously used average value method [97, 98] is used here to evaluate the data to get a single average value for R_{ab} , R_{bc} and R_{ac} describing the relaxation of all the ions in the crystal. As an example of the consequence of this ‘macroscopic’ model, an attempt at a bi-exponential fit to our data was done and is plotted using dashed-dotted lines in Fig. 4.6(a). The best fit obtained for $\pm |a\rangle$, $\pm |b\rangle$, $\pm |c\rangle$ respectively was $0.52e^{-t/5.52} + 0.48e^{-t/2193}$ (blue), $0.48e^{-t/5.52} + 0.52e^{-t/2193}$ (red) and $0.03e^{-t/5.52} + 0.97e^{-t/2193}$ (purple), where time t is in seconds. While these curves fit well to many data points, several data points do not follow the fits, especially for $\pm |a\rangle$ and $\pm |b\rangle$.

Each decay curve obtained in Fig. 4.6 is, in fact, an average of many exponential decays of different ions within the 1 MHz peak shown in Fig. 4.5(b). The solid colored lines in Fig. 4.6(b) and (c) show the fits from the simulation of the microscopic model in the absence and presence of a magnetic field respectively. In addition to the list of steps in simulations described in Sec. 4.3.2, a few more steps were followed to be able to compare the simulations with the experiments:

1. Using the rates R_{ab}^i , R_{bc}^i and R_{ac}^i for an ion ' i ', the population decay in the levels $\pm|a\rangle, \pm|b\rangle, \pm|c\rangle$ is calculated from the rate equations derived in Appendix C of Paper I.
2. Steps [1-3] from the list in Sec. 4.3.2 are repeated for $i = 2, 3 \dots N$, where N is the number of ions in the sphere. An average decay of ' N ' ions gives a single decay curve describing the decay of all ions in the crystal. These are the solid colored lines in Fig. 4.6(b) and (c).
3. All of the above steps are repeated for data with an external magnetic field.
4. Parameters $\Gamma_{ab}, \Gamma_{bc}, \Gamma_{ac}, \kappa_{ab}, \kappa_{bc}$ and κ_{ac} are optimized to match the experimental data.

Decay from $\pm|c\rangle$ is slower than $\pm|a\rangle$ or $\pm|b\rangle$ so one can expect R_{ac} and R_{bc} to be lower than R_{ab} . The experiments show little difference between the decay from $\pm|a\rangle$ and $\pm|b\rangle$, indicating that ions occupying these states have the strongest magnetic dipole-dipole interaction. The optimization is relatively insensitive to Γ_{ac} and the relaxation is predominantly governed by the rates R_{ab} and R_{bc} . The optimized values of spin inhomogeneous linewidths, Γ_{ab} and Γ_{bc} were found to be 0.618 and 3.309 kHz, respectively. We now try to understand why these fitted values differ by a factor of ~ 4.4 . A possible contribution to the spin inhomogeneity is the inhomogeneity in the effective quadrupole tensor \mathbf{Q} in Eq. 3.9, which stems from strains or defects. The ratio of the terms Q_{xy} and Q_{yz} should correspond to the ratio of the inhomogeneous linewidths. After the necessary rotations in Eq. 3.11, $Q_{xy} = 0.0982$ MHz and $Q_{yz} = 0.4389$ MHz. The ratio of these values is indeed ~ 4.4 .

The fitted linewidths represent the local spin inhomogeneity and could, perhaps, be less than the measured values $\Gamma_{ab} = 50.5$ kHz, $\Gamma_{bc} = 75.4$ kHz [75] in a bulk crystal, where the measurements are sensitive toward the bulk spin inhomogeneity. On the contrary, our simulations show that the main contribution to the flip-flop process occurs between ions that are in the order of 10 nm apart (see inset of Fig. 4.8(c)). Thus, we speculate that the local spin inhomogeneity between any two ions situated only 10 nm apart is much less than the measured bulk values, i.e., it lies in the range $\nu_{ab} \pm \Gamma_{ab}$, where Γ_{ab} is in the order of kHz. Finally, this means that on larger scales than 10

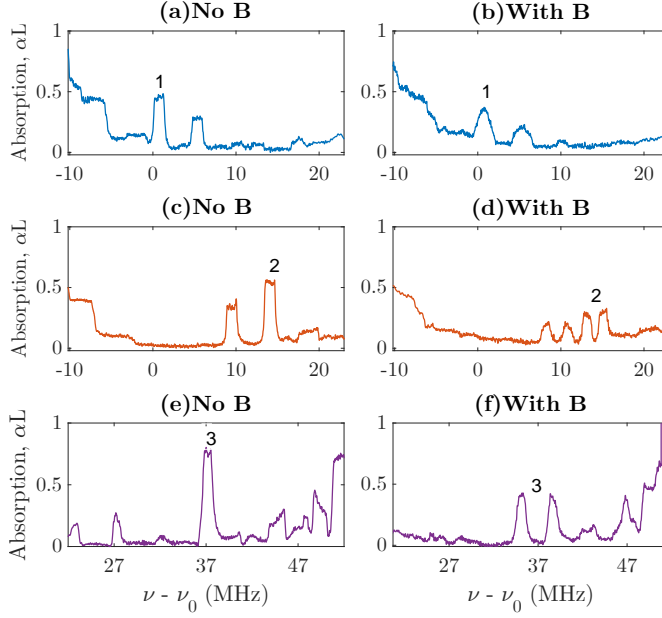


Figure 4.7: Absorption structure showing the Zeeman effect due to which the hyperfine levels split. Peak labelled as ‘1’ corresponds to the transition $\pm|\frac{1}{2}g\rangle \rightarrow \pm|\frac{1}{2}e\rangle$, ‘2’ corresponds to $\pm|\frac{3}{2}g\rangle \rightarrow \pm|\frac{3}{2}e\rangle$ and ‘3’ corresponds to $\pm|\frac{5}{2}g\rangle \rightarrow \pm|\frac{5}{2}e\rangle$. (a), (c) and (e) show the absorption without an external field \mathbf{B} . (b), (d) and (f) show the absorption with an external field \mathbf{B} of 10 mT.

nm, the local average of the spin transition frequency, i.e., ν_{ab} , varies in the order of $\Gamma'_{ab} \approx 50$ kHz such that if two ions that are not spatially close are compared, their inhomogeneity is in the order of the observed bulk inhomogeneity. This description is similar to the one depicted in Fig. 2.3 for optical inhomogeneity. Note, however, that we found no experimental evidence of this hypothesis, and more investigations are needed in order to confirm or deny this hypothesis.

4.4.2 Effect of magnetic field

In the presence of a magnetic field, the doubly degenerate hyperfine levels will lose their degeneracy and the absorption peaks ‘1’, ‘2’ and ‘3’ in Fig. 4.5(b) will split, as discussed in Sec. 3.2.1. The effect of a field of 10 mT on the peaks ‘1’, ‘2’ and ‘3’ is shown in Fig. 4.7. Peak ‘1’ does not completely split but broadens while the largest effect is on peak ‘3’. In the simulations corresponding to the data with field between 5-10 mT, the phenomenological terms κ_{ab} and κ_{bc} introduced earlier in Eq. 4.1 to describe the factor by which inhomogeneity increases in the presence of an external

field are used as fitting parameters. These are the solid colored lines in Fig. 4.6(c). The decay slows down by almost two orders of magnitude in the presence of a magnetic field.

To understand why the rates slow down in a magnetic field, one can infer from Equation (4.1) that the cause could either be the evolution of matrix elements in the dipole-dipole interaction term or a change in density of states $f(E)$. While the matrix elements do not change appreciably with a small field of 5 - 10 mT (or even up to 100 mT), the density of states changes drastically due to the decrease in the homogeneous linewidth by more than a factor of ten, as measured in Ref. [73] and this is attributed to minimizing spin flips of the neighboring Y ions. Another factor contributing to the change in the density of states is the increase in the spin inhomogeneous linewidth [97, 105], characterized by the fitting parameters κ_{ab} and κ_{bc} . The optimized values were found to be 2.6 and 3.6 respectively, with a field between 5-10 mT.

4.4.3 Distribution of Rates

Distribution of ion-ion distance r_{NN} results in a distribution of flip-flop rates. Fig. 4.8(a) and (b) show the histogram of the rates R_{ab} and R_{bc} , with and without a magnetic field. R_{ac} is not shown since R_{ab} and R_{bc} predominantly govern the relaxation. In the absence of a field, R_{ab} is spread over a distribution ranging from $10^{-4} - 10^2$ Hz and peaks at 10^{-2} Hz. R_{bc} is slower, ranging from $10^{-6} - 1$ Hz and peaks at 10^{-4} Hz. Both the rates slow down by two orders of magnitude with a field of 5 - 10 mT. The distribution of r_{NN}^{-6} is shown in Fig. 4.8(c). The inset shows the distribution of r_{NN} , where r is the distance to any of the twenty closest neighbors of any ion considered in the simulations. The number of ions does not increase monotonically with r since only twenty neighbors are considered.

4.4.4 Effect of concentration

The ion-ion distance r_{NN} in Fermi's rule in Eq. 4.1 varies with dopant concentration; thus, the flip-flop rates strongly depend on the dopant concentrations. Although the experiments were not performed in samples with different concentrations, one can simulate this effect. This discussion looks at the impact on the two main terms in Eq. 4.1 separately, namely the matrix element term, $\sum_j |\langle y^i \otimes x^j | H_{dd}^{ij} | x^i \otimes y^j \rangle|^2$ and the density of states, $f(E)$.

The matrix element term is directly proportional to r_{NN}^{-6} , where r_{NN} is ion-ion distance. The effect of concentration on r_{NN}^{-6} and matrix element term is shown in Fig. 4.9. This results from a simulation of the distances between the twenty nearest neigh-

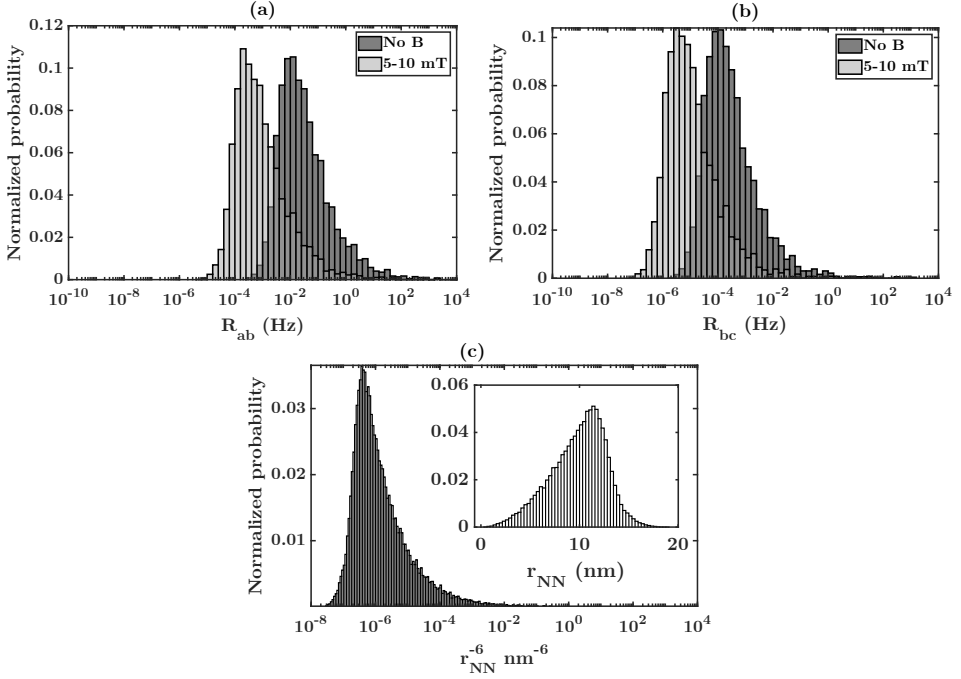


Figure 4.8: Distribution of flip-flop rates. (a)-(b) show a histogram of R_{ab} and R_{bc} respectively, for two cases: residual field < 0.2 mT and external applied field of 5-10 mT. In the presence of a residual field, R_{ab} peaks at 10^{-2} Hz while R_{bc} peaks at 10^{-4} Hz. Both the rates slow down by about two orders of magnitude with a field of 5-10 mT. The distribution of r^{-6} for the twenty closest neighboring ions considered in the simulations is shown in (c). The inset shows the histogram of r , the ion-ion distance.

bors in a 100 nm sphere of YSO. The peak of the distribution of r_{NN} in the inset of part (a) decreases from 19, 14 to 11 nm for concentrations of 0.01% (purple), 0.025% (red), and 0.05% (blue) respectively. Thus, r_{NN} (and hence the flip-flop rate) scales quadratically with concentration, as taken in the macroscopic model [97]. The area under each distribution is not the same since the total number of dopants differs in each case. In part (b), the matrix element term decreases by more than an order of magnitude when the concentration is decreased from 0.05% to 0.01%.

The effect of concentration on the density of states is difficult to predict without more experimental data but one can make some qualitative predictions from other non-Kramers ions like Eu^{3+} . The spin inhomogeneous linewidth is expected to increase as concentration increases, as evidenced in some experimental measurements in Eu^{3+} : Y_2SiO_5 [76, 86, 106, 107]. However, the homogeneous linewidth does not show such dependence on dopant concentration but is mainly dependent on excitation densities

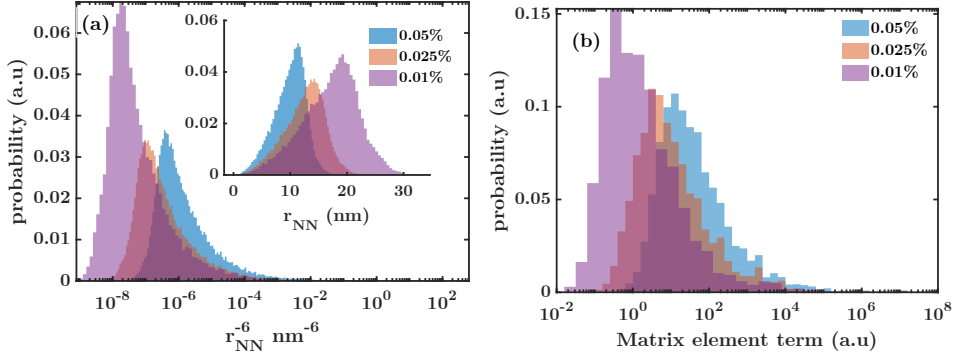


Figure 4.9: The effect of dopant concentration on ion-ion distance and magnetic dipole interaction for three different dopant concentrations of 0.05% (blue), 0.025% (red) and 0.01% (purple) (a) Histogram of r_{NN}^{-6} for twenty closest neighbors and r_{NN} in the inset, where r_{NN} is the ion-ion distance (b) Histogram of the matrix element term in Eq. 4.1.

and external magnetic field [68]. So overall, the density of states could decrease as the concentration is increased.

Chapter 5

Ensemble qubits and coherent control

This chapter describes some tools used to control ensemble qubits, which are relevant for Papers II and III. The type of pulses used to perform operations on ensemble qubits is introduced, then the process of creating a transparent spectral window in Pr:YSO and Eu:YSO is described. This step is necessary before the initialization of a qubit in the desired state. The readout method, sources of noise in the detection, and errors due to the post-processing of transmission signal (called deconvolution) are discussed.

5.1 Control pulses

All operations to manipulate the spin states of rare-earth-ions in this work have been done using optical pulses. A simple square pulse performs poorly for this purpose since it can have several frequency components that can off-resonantly excite unwanted ions. Pulses with more complex shapes, called ‘sechyp’ and ‘sechscan’ are discussed below. Another type of pulse referred to as ‘shortcut’ pulses, is used in Paper II and described later in Ch.6.

5.1.1 Sechyp

Efficient population transfers robust against variations in the electromagnetic field amplitude have been achieved using complex secant hyperbolic or ‘sechyp’ pulses, first introduced in the context of NMR and inhomogeneities in magnetic field [108]

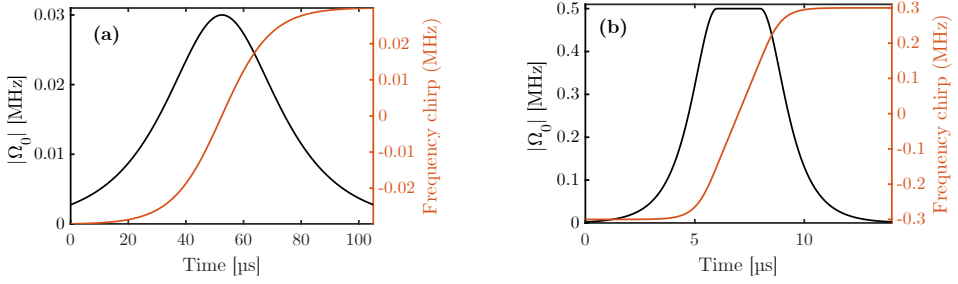


Figure 5.1: Profile of Rabi Frequency amplitude $|\Omega_0|$ and Frequency chirp of a (a) sechyp and (b) sechscan pulse.

and later applied to the case of rare-earth materials [109]. They have been shown to perform exceptionally well in inverting populations while simultaneously being resilient to inhomogeneity in optical frequency [21, 56, 109]. The Rabi frequency of a sechyp pulse varies as:

$$\Omega(t) = \Omega_0 \text{sech}[\beta(t - t_0)]^{1-i\mu} \quad (5.1)$$

where Ω_0 is the maximum Rabi frequency. μ and β are related to the full width at half maximum of the intensity of the sechyp envelope, t_{fwhm} , and the frequency width of the sechyp the frequency chirp, f_{width} :

$$\beta = \frac{2\ln(1 + \sqrt{2})}{t_{fwhm}} \quad (5.2)$$

$$\mu = \frac{\pi f_{width}}{\beta} \quad (5.3)$$

An example of the sechyp shape is shown in Fig. 5.1(a). The pulse parameters used here are: $f_{width} = 60$ kHz, $t_{fwhm} = 30$ μ s, $t_{cutoff} = 105$ μ s, $|\Omega_0|_{max} = 30$ kHz, where t_{cutoff} is the total duration of the pulse.

5.1.2 Two-color pulses

Sechyp pulses are good at performing population transfers between ground states but to create and manipulate superposition states, one needs to use two sechyp pulses simultaneously resonant on two transitions, as shown in Fig. 5.2(a). Both pulses have the same Rabi frequency Ω_0 . By varying the phase ϕ between the two pulses, one can

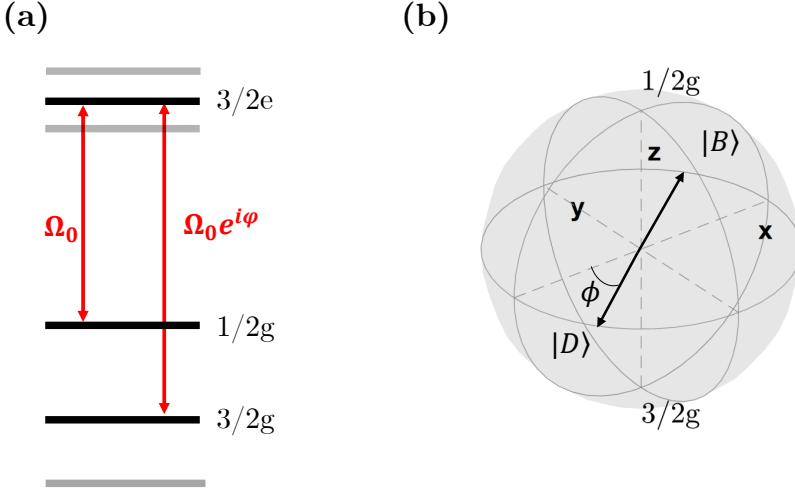


Figure 5.2: (a) Transitions for the two-color pulses. (b) Bloch sphere showing the bright and dark states, $|B\rangle$ and $|D\rangle$, respectively. $1/2g$ corresponds to $|0\rangle$ and $3/2g$ corresponds to $|1\rangle$.

create a pair of states called bright $|B\rangle$ and dark states $|D\rangle$. Due to the interference of the two light fields, $|B\rangle$ interacts with the light, and $|D\rangle$ does not interact with the light. They are written as:

$$|B\rangle = \frac{1}{\sqrt{2}}(|0\rangle + e^{-i\phi}|1\rangle)$$

$$|D\rangle = \frac{1}{\sqrt{2}}(|0\rangle - e^{-i\phi}|1\rangle)$$

One two-color (TC) pulse takes the ‘bright’ part of the wavefunction of the ensemble qubit to the excited state and another two-color pulse phase-shifted by $\pi - \theta$ brings it down to $|B\rangle$ with an added phase $e^{i\theta}$. In the basis of $|B\rangle$ and $|D\rangle$ states, this operation is written as:

$$U_{TC}^{BD} = \begin{bmatrix} e^{i\theta} & 0 \\ 0 & 1 \end{bmatrix} = e^{i\theta} |B\rangle \langle B| + |D\rangle \langle D| \quad (5.4)$$

If one looks at the Bloch sphere representation where $|0\rangle$ and $|1\rangle$ lie at the poles of the sphere, $|B\rangle$ and $|D\rangle$ will lie in the equatorial plane, diametrically opposite to each

other. This is shown in Fig. 5.2(b). One pair of such two-color pulses result in rotations of the initial state around $|D\rangle$ on the Bloch sphere. Arbitrary rotations can be performed by varying the $|D\rangle$ state (i.e., varying ϕ). Additional phase-compensation pulses will be needed so that another pair of TC pulses target the dark part of the wavefunction, $|D\rangle$. $|B\rangle$ will remain untouched in this stage and $|D\rangle$ acquires the same spread in phases as $|B\rangle$ did in the first pair of TC pulses. This sequence is used to perform arbitrary gate operations and fidelities ranging between 92-96 % have been obtained in Ref. [21]. It will also be used in Paper III but using sechscan pulses instead of sechyp.

5.1.3 Sechscan

The oscillator strength of Eu^{3+} , doped into YSO, is much weaker than Pr^{3+} , which demands pulses with higher laser intensity to reach the same Rabi frequency. Another way to reach the required pulse area is to use a longer pulse, but may not achieve good inversion over the entire qubit peak, and longer pulses are not good because of increased decoherence. One needs to design a way to invert the entire qubit peak while not compromising on the duration of the pulse too much. For this purpose, the sechyp pulses were modified so that there are three regions in the profile of Ω : a rising edge which is one-half of a sechyp pulse, a region of constant amplitude over which frequency is linearly chirped and a falling edge which is the next half of a sechyp pulse. Such pulses have earlier been used with the name ‘sechscan’ pulse in [56] and ‘hyperbolic-square-hyperbolic pulse’ in [110]. It has also been used for simulating two-qubit interaction gates in Ref. [15].

The Rabi frequency Ω and instantaneous phase, ϕ , of the pulse are defined[15] below, where $\Omega(t) = |\Omega_0(t)|e^{-i\phi(t)}$:

$$|\Omega(t)| = \begin{cases} \Omega_0 \text{sech}[\beta(t - t_0)], & 0 \leq t < t_0, \\ \Omega_0, & t_0 \leq t \leq t_0 + t_{\text{scan}} \\ \Omega_0 \text{sech}[\beta(t - t_0 - t_{\text{scan}})], & t_0 + t_{\text{scan}} < t < t_{\text{cutoff}} \\ 0, & \text{otherwise} \end{cases} \quad (5.5)$$

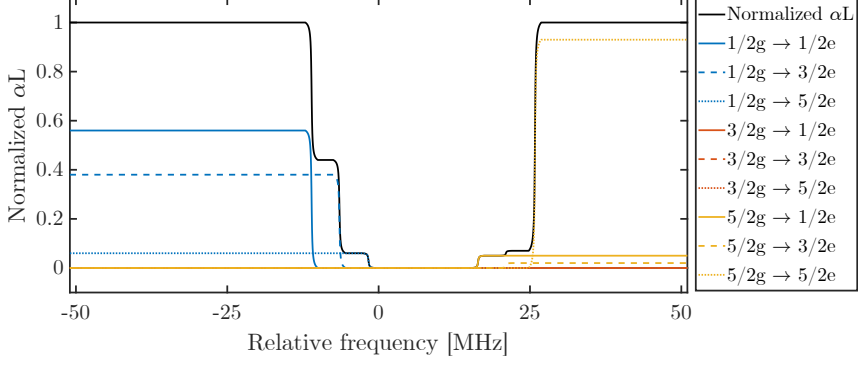


Figure 5.3: Simulation of the absorption spectrum of the optimal transparent spectral window (TSW). The black line shows the total absorption while colored lines show the absorption corresponding to a particular transition, indicated in the legend. The qubit ions now live in the $|\frac{5}{2}g\rangle$ state (yellow lines) to the right side of the TSW, ready for the initialization step.

$$\phi(t) = \begin{cases} -\mu \ln\{\text{sech}[\beta(t - t_0)]\} - \frac{2\pi f_{\text{scan}}}{2}t, & 0 \leq t < t_0, \\ \frac{2\pi f_{\text{scan}}}{2}(-t + \frac{(t-t_0)^2}{t_{\text{scan}}}), & t_0 \leq t \leq t_0 + t_{\text{scan}} \\ -\mu \ln\{\text{sech}[\beta(t - t_0)]\} \\ + \frac{2\pi f_{\text{scan}}}{2}[-t_0 + (t - t_0 + t_{\text{scan}})], & t_0 + t_{\text{scan}} < t < t_{\text{cutoff}} \\ 0, & \text{otherwise.} \end{cases} \quad (5.6)$$

The parameters t_0 and t_{scan} are defined as:

$$t_{\text{scan}} = \frac{2\pi f_{\text{scan}}}{\mu\beta^2} \quad (5.7)$$

$$t_0 = \frac{t_{\text{cutoff}} - t_{\text{scan}}}{2} \quad (5.8)$$

where f_{scan} is the range of the linear frequency chirp applied for the duration, t_{scan} .

An example of is sechscan pulse is shown in Fig. 5.1(b). The parameters used to plot this pulse are: $f_{\text{width}} = 300$ kHz, $f_{\text{scan}} = 300$ kHz, $t_{fwhm} = 1.75 \mu$ s, $t_{\text{cutoff}} = 14 \mu$ s, $|\Omega_0|_{\text{max}} = 0.5$ MHz. This pulse has been used to perform transfers in Paper III and the performance of this pulse will be discussed in Sec. 6.3.6.

5.2 Creating ensemble qubits

There are two steps involved in creating ensemble qubits :

1. **Creating a transparent spectral window (TSW):** This step pumps away any unwanted ions spectrally close to the qubit ions so that there are no ions absorbing in the region spectrally close to the qubits.
2. **Initialize qubit ions:** The qubit ions are targeted and initialized to the desired state.

The basic principles in creating the TSW are optical pumping and spectral hole burning. A brief and simplified description is given here using Pr:YSO as an example, and the reader is referred to Ref. [18] for a thorough explanation. The laser can couple to nine different transitions from the ground to the excited state (shown in Fig. 2.2(b)) at a given frequency due to the optical inhomogeneous broadening. Let us call the ions excited at the nine different transitions different ‘classes’ of ions. The objective is to isolate one class of ions that we can use as the ensemble qubit and the other eight classes (the non-qubit ions) need to be pumped away to other hyperfine levels to limit off-resonant excitations.

When the laser excites ions repeatedly at one frequency, a spectral hole is created since the ions are pumped away to another hyperfine level. This hole lives quite long since the hyperfine lifetime is long. If such an excitation occurs over a range of frequencies, a transparent spectral window (just a wider hole) can be created, where the ions have been pushed away to other levels in a wide spectral region. One can create an optimal set of pulses to do this in a way that creates the widest transmission window possible [18]. A simulated optimal pit in Pr:YSO is shown in Fig. 5.3. The qubit class of ions has been shelved in the $|\frac{5}{2}g\rangle$ state to the right of the transparent window (shown as the yellow lines) and the non-qubit ions have been pushed to the $|\frac{1}{2}g\rangle$ state (shown as the blue lines). The qubit ions are now ready to be initialized into the desired state. The type of pulses used in this thesis are sechscan pulses, described in Sec. 5.1.3, and the exact sequence of pulses used in Pr:YSO and Eu:YSO is described below.

5.2.1 Pr:YSO

Fig. 2.2(b) is used as a reference here for the energy levels. The complete sequence of pulses [III] to create a TSW in Pr:YSO, used in Paper I and II is listed in Tab. 5.1. The pulse parameters used here are: $f_{\text{width}} = 500$ kHz, $t_{fwhm} = 3 \mu\text{s}$, $t_{\text{cutoff}} = 86 \mu\text{s}$. The frequency scan range is f_{scan} , set by the start and end frequencies ν_{start} and ν_{end} ,

Table 5.1: Sequence of pulses used for creating the transmission window in Pr:YSO, with the start and end frequencies of f_{scan} . The intensity for each pulse is adjusted to target the transitions listed in the column Transition. The energy levels referred to here are shown in Fig. 2.2(b).

Pulse	ν_{start} (MHz)	ν_{end} (MHz)	Transition
BurnPit1	+32	+24	$\pm \frac{3}{2}g\rangle \rightarrow \pm \frac{1}{2}e\rangle$
BurnPit2	+24	+16	$\pm \frac{3}{2}g\rangle \rightarrow \pm \frac{5}{2}e\rangle$
BurnPit3	+16.1	+7.5	$\pm \frac{3}{2}g\rangle \rightarrow \pm \frac{5}{2}e\rangle$
BurnPit4	-17	-9	$\pm \frac{5}{2}g\rangle \rightarrow \pm \frac{5}{2}e\rangle$
BurnPit5	-9	-1	$\pm \frac{5}{2}g\rangle \rightarrow \pm \frac{1}{2}e\rangle$
BurnPit6	+7.5	-1.1	$\pm \frac{3}{2}g\rangle \rightarrow \pm \frac{1}{2}e\rangle$
BurnPit7	-1.1	+7.5	$\pm \frac{5}{2}g\rangle \rightarrow \pm \frac{1}{2}e\rangle$
BurnPit8	+7.5	+15.95	$\pm \frac{5}{2}g\rangle \rightarrow \pm \frac{1}{2}e\rangle$

respectively. The intensity of each pulse is adjusted to target the transitions listed in column ‘Transition’. These pulses (‘BurnPit’) are repeated in the following sequence:

1. Repeat 120 times: BurnPit4 and BurnPit5.
2. Repeat 90 times: BurnPit1-3 and BurnPit5-8.
3. Repeat 40 times: BurnPit1-3 and BurnPit5.
4. Repeat 60 times: BurnPit4 and BurnPit6-8.
5. Repeat 60 times: BurnPit7.

A waiting pulse of 1000 μs follows each pulse to allow the system to decay to the ground states. This step empties the $\pm |\frac{1}{2}g\rangle$ and $\pm |\frac{3}{2}g\rangle$ levels and shelves the ions to $\pm |\frac{5}{2}g\rangle$, as shown in Fig. 5.3. The absorption profile after this step in the experiments is shown in Fig. 5.4(a). This can be compared with the simulated result in Fig. 5.3. The region between 0 – 15 MHz is transparent, where the qubit ions can be initialized.

For population initialization in either $\pm |\frac{1}{2}g\rangle$ or $\pm |\frac{3}{2}g\rangle$, a weak sechscan pulse (‘Burn-Back’) targeting the transition $\pm |\frac{5}{2}g\rangle \rightarrow \pm |\frac{1}{2}e\rangle$ was used repeatedly. This sequence ‘burns back’ ions to $\pm |\frac{1}{2}g\rangle$ and $\pm |\frac{3}{2}g\rangle$. Depending on the target initialization state, ions in $\pm |\frac{1}{2}g\rangle$ or $\pm |\frac{3}{2}g\rangle$ are cleaned away. The absorption profile after this step is shown in Fig. 5.4(b). It shows two traces: the blue shows that the qubit is in $\pm |\frac{1}{2}g\rangle$ and the red shows it in $\pm |\frac{3}{2}g\rangle$. For the blue trace, there are three peaks corresponding to ions absorbing to the three excited states and the height varies since the relative

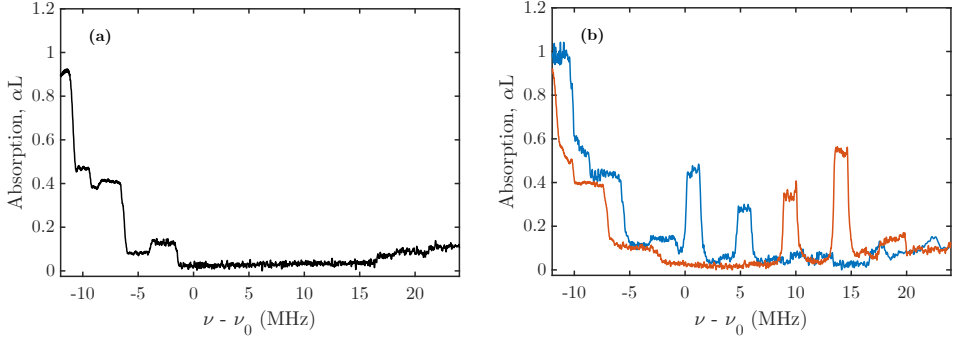


Figure 5.4: (a) Transparent spectral window in Pr:YSO, after emptying the qubit states $|0\rangle$ and $|1\rangle$ in experiments. (b) Qubit peaks $|0\rangle$ (blue) and $|1\rangle$ (red), after the initialization.

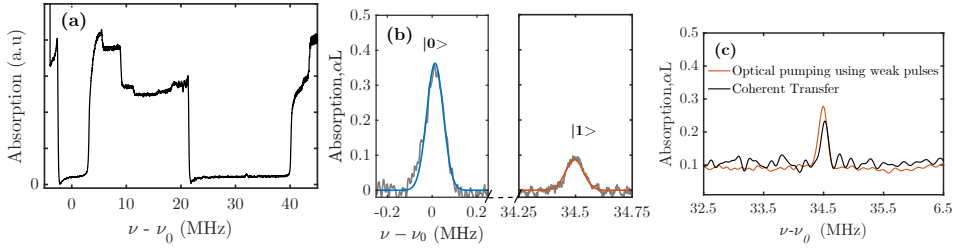


Figure 5.5: (a) Transparent spectral wells in Eu:YSO, after emptying the qubit states $|0\rangle$ and $|1\rangle$. (b) Absorption profile showing qubit peak in $|0\rangle$ (blue) corresponding to $|\frac{1}{2}g\rangle \rightarrow |\frac{5}{2}e\rangle$ at 0 MHz and qubit peak in $|1\rangle$ corresponding to $|\frac{3}{2}g\rangle \rightarrow |\frac{5}{2}e\rangle$ (red) at 34.5 MHz. The blue and red lines are Gaussian fits. (c) Qubit initialization using two methods: coherent transfer and optical pumping.

oscillator strength for each transition is different, see Tab. 2.2. The blue trace has only two transitions within the TSW. The frequency shift between the red and blue traces is an error from the analysis.

To initialize ions in $\pm |\frac{5}{2}g\rangle$, the transmission window is created by shifting all the ‘BurnPit’ pulses by $f_0 = -27.5$ MHz to target another class of ions and empty the $\pm |\frac{5}{2}g\rangle$ level. Then, ions are initialized in $\pm |\frac{3}{2}g\rangle$ by burning back from the transition $\pm |\frac{1}{2}g\rangle \rightarrow |\frac{5}{2}e\rangle$ at $f_0 + (4.8 + 4.6)$ MHz. Any ions absorbing inside the transmission window that belong to a different ion class than intended are cleaned away using sechscan pulses with the same parameters as the ‘BurnPit’ pulses. The pulse parameters for the ‘burn back’ pulses used here are: $f_{\text{width}} = 120$ kHz, $t_{fwhm} = 11.6 \mu\text{s}$, $t_g = 150 \mu\text{s}$, $f_{\text{scan}} = 1$ MHz.

Table 5.2: The sequence of pulses used for creating the transparent wells in Eu:YSO, with the start and end frequencies of f_{scan} . The intensity used for each pulse was the maximum value available for use in the experiments. The energy levels referred to here, are shown in Fig. 2.2(c).

Pulse	ν_{start} (MHz)	ν_{end} (MHz)
BurnPit1	-2.5	+2.5
BurnPit2	+21.54	+28.34
BurnPit3	+28.24	+33.34
BurnPit4	33.14	+39.34

5.2.2 Eu:YSO

Fig. 2.2(c) is used as a reference here for the energy levels. The excited state frequency splitting in Eu:YSO is higher than that of the ground state so there are two ‘transparent wells’ created around the qubit transitions $\pm |\frac{1}{2}g\rangle \rightarrow \pm |\frac{5}{2}e\rangle$ and $\pm |\frac{3}{2}g\rangle \rightarrow \pm |\frac{5}{2}e\rangle$. The sequence of pulses in this case, is not as sophisticated as in Pr:YSO, but the unwanted ions in a wide spectral region are cleared away. The complete sequence of pulses, used in Paper III is listed in Tab. 5.2. The pulse parameters used here are: $f_{\text{width}} = 500$ kHz, $t_{fwhm} = 4$ μ s, $t_{\text{cutoff}} = 86$ μ s. The frequency scan range is f_{scan} , set by the start and end frequencies ν_{start} and ν_{end} , respectively. The intensity of each pulse is adjusted to target the transitions listed in column ‘Transition’. These pulses (‘BurnPit1-4’) are repeated sequentially 120 times. A wait pulse of 2 ms follows each pulse to allow the system to decay to the ground states and the sequence ends with a wait pulse of duration of 3 ms. A longer wait time may have been better since the lifetime of the excited state is 1.9 ms. The absorption profile after this step is shown in Fig. 5.5(a). A region of about ± 2.5 MHz around 0 MHz is transparent and the qubit $|0\rangle$ will be initialized at 0 MHz. The transparent well around 34.5 MHz is wider - about 13 MHz on the left and about 5 MHz on the right. The qubit $|1\rangle$ will be initialized at 34.5 MHz.

Two methods were tried for qubit initialization. To initialize the qubit in $\pm |\frac{3}{2}g\rangle$, the first method involves optical pumping on the transitions $|\frac{1}{2}g\rangle \rightarrow |\frac{1}{2}e\rangle$ and $|\frac{3}{2}g\rangle \rightarrow |\frac{1}{2}e\rangle$ repeatedly, with weak pulses separated by a delay of 2 ms. Since the pulses are weak, the off-resonant excitations are not significant. The second method involves coherently transferring ions from $|\frac{5}{2}g\rangle \rightarrow |\frac{1}{2}e\rangle$ and then $|\frac{1}{2}e\rangle \rightarrow |\frac{3}{2}g\rangle$, without any delay. The result of doing this is shown in Fig. 5.5(c). The second method relies on the transfer efficiency of the pulse used. In contrast, the first method is not limited by the transfer efficiency of the pulse since the pulses are repeated several times, resulting in qubit peaks with higher absorption. The first method was chosen in Paper III.

5.3 Calibrating the available Rabi frequency

Having created an ensemble qubit, one needs to calibrate the available Rabi frequency (corresponding to the available laser power) for the qubit transitions and check if the ions experience an optimal value of Rabi frequency. One way of doing this is to run a Rabi flopping sequence on each of the qubit transitions. The idea is to target the qubit transition with a sequence of square pulses with increasing pulse areas. By reading out the population after each pulse is sent, one can judge how much population is left in each state. In the case of rare-earth ensemble qubits, a square pulse will not achieve a full π pulse (see Sec. 5.1). However, one can still use this method to judge what is the maximum Rabi frequency available for each transition and the gate operations need to be designed using this calibration. Additionally, there could be a large inhomogeneity in the Rabi frequency experienced by the ions due to Gaussian propagation through the crystal (discussed in Paper III) and it is good to estimate an average value for all the ions.

For the case of Pr:YSO, the calibration between the laser power and Rabi frequency is pretty well established in the lab here in Lund. Rabi flopping is routinely used to adjust the position of the light focus inside the crystal. Optimally, the focal plane should be in the center of the crystal so that the ions experience maximum Rabi frequency. If it is far from the optimal position, Rabi flopping will occur at a frequency lower than expected. A square pulse of duration $2 \mu\text{s}$ targets the qubit transition $|\frac{1}{2}g\rangle \rightarrow |\frac{1}{2}e\rangle$. By varying the Rabi frequency of this pulse, one can determine the value needed to completely flip the population from $|\frac{1}{2}g\rangle$ to $|\frac{1}{2}e\rangle$. The result of doing this is shown in Fig. 5.6(a) and the flop occurs at 273 kHz. Note that the y-axis here is the area of the peak corresponding to the above transition. When it is maximum, ions are completely in $|\frac{1}{2}g\rangle$, and when it is at its minimum, the ions have been transferred to $|\frac{1}{2}e\rangle$.

For the case of Eu:YSO, we knew from calculations, that we may not have enough Rabi frequency to do a good flop and we may need to use the maximum laser power. For this purpose, the amplitude of the square pulse was fixed to the maximum available power and the duration was varied between 400 ns and $4.8 \mu\text{s}$. The result of Rabi-flopping the $|\frac{1}{2}g\rangle \rightarrow |\frac{5}{2}e\rangle$ transition is shown in Fig. 5.6(b). The flop occurs at 800 ns, which implies that the Rabi frequency $\Omega/2\pi$ is 625 kHz. The frequency bandwidth of the square pulse may not cover the entire peak width (100 kHz) toward the end of the sequence. However, it still gives enough information to capture the first flop. Similarly, for the transition $|\frac{1}{2}g\rangle \rightarrow |\frac{5}{2}e\rangle$, it was measured to be 357 kHz. This information is used to design the gate operations and is discussed in Paper III.

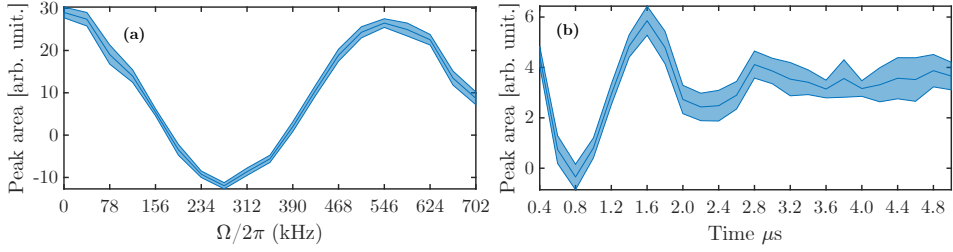


Figure 5.6: Calibration of Rabi frequency on the transition (a) $|\frac{1}{2}g\rangle \rightarrow |\frac{1}{2}e\rangle$ in Pr:YSO (b) $|\frac{1}{2}g\rangle \rightarrow |\frac{5}{2}e\rangle$ transition in Eu:YSO.

5.4 Readout

The readout was done using chirped readout techniques developed in [112, 113]. The pulse is chirped in frequency at constant amplitude. Due to the fast readout scan rate, the transmission signal contains Free Induction Decay from each peak that needs to be deconvoluted as described in [112]. To resolve a spectral feature of width f_{res} , the readout pulse needs to be as long as $T_{\text{after feature}} = \frac{1}{f_{\text{res}}}$ after it encounters the spectral feature. This is due to the fact that a square pulse of duration T has a sinc shape in its Fourier space (frequency) with a majority of its frequency content within $[\frac{-1}{T}, \frac{1}{T}]$. If the available detector bandwidth is f_{det} , the maximum scan rate one can use is $S_{\text{max}} = \frac{f_{\text{det}}}{T_{\text{after feature}}}$.

5.5 Detection

To choose a detector in general, some important questions to ask are :

- What is the required SNR?
- What is the required gain and frequency bandwidth?
- How much noise can you tolerate?
- Is your signal shot noise limited?

Answers to these questions have been answered in several places throughout this thesis and some of them are discussed in this section.

All the experiments in this thesis involve the use of two detectors, one to measure the transmission signal from the crystal and the other is used as a reference before the

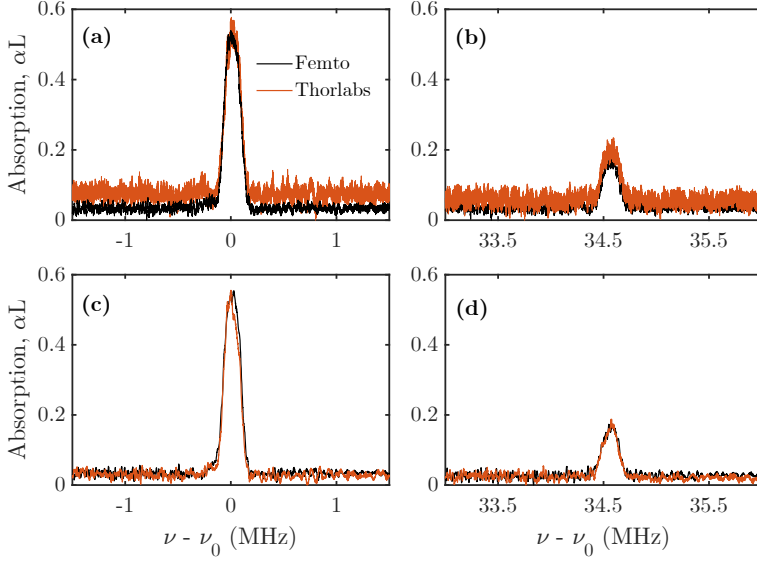


Figure 5.7: Comparison of noise between detection using the Femto amplifier (black trace) and Thorlabs PDB150A (orange trace). The plots on the left correspond to $|0\rangle$ and on the right, to $|1\rangle$. The plots on the top and bottom are the data taken without and with frequency filters, respectively. (a) $|0\rangle$, no filtering (b) $|1\rangle$, no filtering (c) $|0\rangle$, with filtering (d) $|1\rangle$, with filtering.

crystal to record the fluctuations in laser power. The transmission signal is divided by the reference to remove any correlated noise. For paper I, Thorlabs PDB150A was used as both the reference and transmission detector. For paper II, Thorlabs PDB150A was used as the reference detector and for the transmission detector, a combination Si PIN photodiode (Hamamatsu, S5973-02) and a current amplifier (Femto, DHPCA-100) were chosen. The latter was used for both reference and transmission in Paper III due to higher demands on the noise level. (Only one Femto amplifier was available during the experiments in Paper II but another became available for the experiments in Paper III.)

Thorlabs PDB150A has a bandwidth of 5 MHz at a transimpedance gain of 10^5 V/A. The responsivity is ~ 0.4 A/W at 600 nm and the Noise Equivalent Power is 12 pW/ $\sqrt{\text{Hz}}$ (in other words, the input noise current density or the background noise is 4.8 pA/ $\sqrt{\text{Hz}}$). The Si diode also has a photosensitivity of 0.4 A/W and the Femto amplifier has a bandwidth of 1.8 MHz at a transimpedance gain of $R = 10^6$ V/A. This amplifier has low input noise current density ($i_{n,b}$), equal to 140 fA/ $\sqrt{\text{Hz}}$ and the Johnson noise is 122 fA/ $\sqrt{\text{Hz}}$. All the values are taken from their respective data sheets from the supplier.

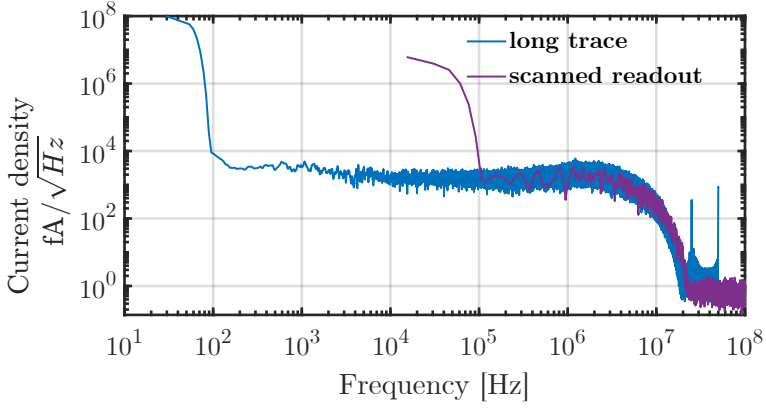


Figure 5.8: Noise spectrum obtained using homodyne detection using readout pulse which was $\sim 100\mu\text{s}$ long (purple) and a longer trace of duration $\sim 100\text{ms}$ (blue). See text for details.

The noise level of both the choices was compared by reading out the qubits $|0\rangle$ and $|1\rangle$ in Eu:YSO and is plotted in Fig. 5.7. The plots on the left correspond to $|0\rangle$ and on the right, to $|1\rangle$. The plots on the top and bottom are the data taken without and with frequency filters (3 dB at 7.25 MHz), respectively. From the plots on the top, it is evident that the Femto amplifier performs much better. The noise can be further reduced with additional spectral filtering by the oscilloscope during the data acquisition. For paper III, where the absorption and SNR were low, it was essential to minimize the noise in the detection.

5.5.1 Noise characterization

Next, one needs to characterize the sources of noise in the measurements using the Femto amplifier, and below, it is shown that the detection was limited by shot noise. Details are described, for the reference of another student, if they want to repeat similar measurements. The characterization was done using homodyne detection, where the signal was split into two parts S_1 and S_2 , using a 50:50 beamsplitter and detected using a detector on each arm of the beamsplitter. The signal consisted of the readout pulse $\sim 100\mu\text{s}$ long or a longer trace of duration $\sim 100\text{ms}$ to capture low-frequency noise. S_1 and S_2 were recorded using an oscilloscope and divided by each other to eliminate any correlated noise like laser noise and the current spectral density was generated using the 'pwelch' function in Matlab and the result is shown in Fig. 5.8. It has a fairly flat profile, about $1000\text{ fA}/\sqrt{\text{Hz}}$ in the frequency range 1 kHz - 1 MHz.

The expected shot noise that could add up to the above value can be calculated as follows. The optical signal on each of the two detectors (readout pulse or 100ms long trace) was $\sim 1.7\mu\text{W}$, generating a current $i_s = 0.7\mu\text{A}$ in the photodiode (since the photosensitivity is 0.4 A/W). The shot noise is given as [114]:

$$i_{n,s} = \sqrt{2qi_s\Delta f}$$

where $\Delta f = \frac{1}{\Delta t}$ and Δt is the time spent measuring the spectral feature, calculated as $\Delta t = \frac{f_{\text{res}}}{\text{scan rate}}$. In Paper III, $f_{\text{res}} = 30\text{ kHz}$ and scan rate = $50\text{ kHz}/\mu\text{s}$. The current density in Fig. 5.8 is in units of $\text{fA}/\sqrt{\text{Hz}}$ so one can also write the above formula as $i_{n,s} = 0.57 \times 10^6 \sqrt{i_s} \text{ fA}/\sqrt{\text{Hz}}$, where i_s is in A. Thus, the shot noise in signal S_1 is $480 \text{ fA}/\sqrt{\text{Hz}}$, which is larger than the input noise current density of the amplifier. It can thus be concluded that the measurements are shot noise limited ¹. The total noise (shot noise $i_{n,s}$, input noise current density $i_{n,b}$ and Johnson noise $i_{n,j}$) after the two signals S_1 and S_2 are divided can be added in quadrature [114], as follows:

$$i_{n,tot} = \sqrt{i_{n,s1}^2 + i_{n,s2}^2 + i_{n,b1}^2 + i_{n,b2}^2 + i_{n,j1}^2 + i_{n,j2}^2} \approx 727 \text{ fA}/\sqrt{\text{Hz}}$$

In Fig. 5.8, the noise level is $\sim 1000 \text{ fA}/\sqrt{\text{Hz}}$, which is fairly close to the calculated value.

The electrical SNR can then be calculated using the values noted above:

$$\text{SNR} = \frac{i_s}{i_{n,tot}} = \frac{i_s}{\sqrt{2qi_s\Delta f}} \approx 1000$$

However, the SNR in the absorption signal after post-processing (deconvolution, discussed in Sec. 5.6) is only about 10 and not as impressive. This is evident in Fig. 5.5(b) when one compares the height of the absorption peaks $|0\rangle$ and $|1\rangle$ to the noise floor.

5.6 Deconvolution errors

The readout chirp rate is fast relative to the width of the qubit peak, and the Free Induction Decay from the qubit peak distorts the transmission signal. To retrieve the spectral shape of the peak, a deconvolution algorithm[112] is used. However, it is designed for an optically thin medium and can introduce some errors if the absorption is high. It does not handle sharp changes in absorption very well. One consequence

¹A good rule of thumb for shot noise limited detection in photodiodes is to have a signal voltage above 200 mV or $0.4\mu\text{A}$ in our case. See Tab. 18.2 in Ref. [114].

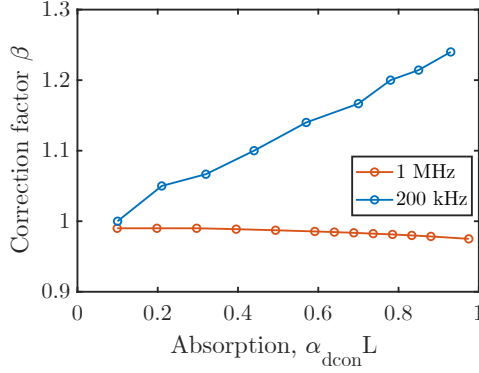


Figure 5.9: The deconvolution algorithm overestimates the absorption of a peak of width 200 kHz and underestimates the absorption of a peak of width 1 MHz. The correction factor shown here is defined in Eq. 5.9.

is that spectral peaks with higher absorption have some artifacts. Some artifacts are discussed below using simulations with the Lindblad equation, including the effects of propagation in an absorbing material. The Lindblad equation to describe the evolution of a quantum system will be introduced in Sec. 6.1.

Six levels of Pr^{3+} doped into a YSO crystal were used in the simulations. The value of the absorption coefficient, α was fixed. An ensemble peak of optically inhomogeneous ions was initialized in one of the ground states. The peak was read out using a chirped pulse of constant amplitude, and the transmission signal was obtained after propagation through the crystal. The transmission signal is in the units of intensity, and the standard method is to convert it to the absorption depth, αL , where L is the length of the crystal. After the deconvolution, the absorption depth obtained was $\alpha_{\text{dcon}} L$. α_{dcon} can be different from α if the absorption is high. One must introduce a dimensionless correction factor labeled here as β . To recover the ‘true’ absorption α , the following correction needs to be made:

$$\alpha = \frac{\alpha_{\text{dcon}}}{\beta} \quad (5.9)$$

The simulations can be repeated for different values of absorption and width of the spectral peak. The result is shown in Fig. 5.9, for two peaks of width 1 MHz and 200 kHz (These widths were chosen because they were used in Paper I and II, respectively). The y-axis of Fig. 5.9 is the correction factor β that needs to be divided by the absorption αL value obtained from the deconvolution. The absorption of a 1 MHz peak is slightly under-estimated, but that of a 200 kHz peak is over-estimated by a more significant margin.

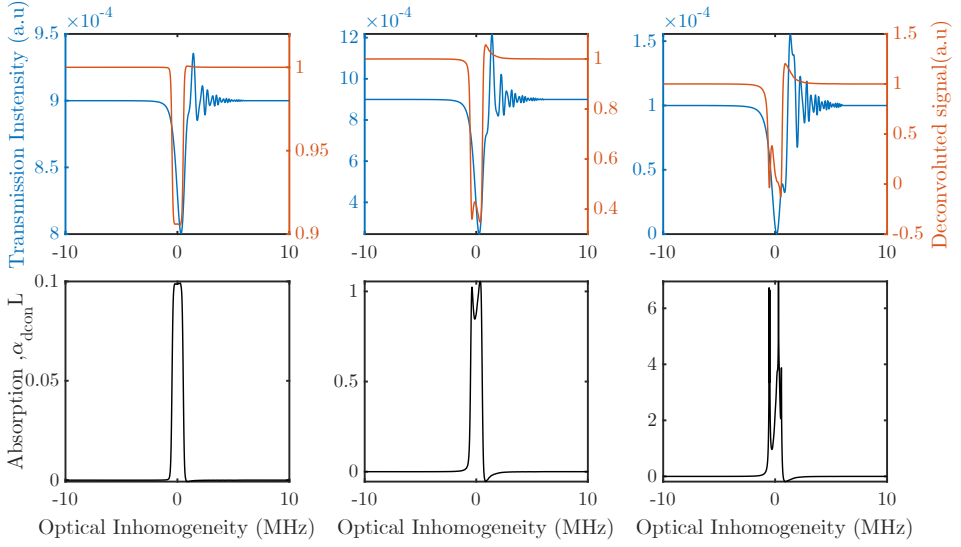


Figure 5.10: Results of a simulation of a chirped pulse reading out a spectral peak of width 1 MHz, with varying absorption, after propagation through a crystal. (Top) The blue lines are the simulated transmission signal of the chirped pulse, and the orange lines are the signal after the blue lines are deconvoluted. (Bottom) The deconvoluted signal shown in the plots above is converted to Absorption $\alpha_{\text{conv}}L$, according to Beer - Lambert's law. Plots on the top and bottom share a common x-axis.

Another artifact is discussed in Paper II, where features with negative absorption are present. This results in an error in the calculated peak area or the population, but the propagated error in calculating the fidelity of an operation is within the error bars. An example of such a negative feature is shown in Fig. 5.10. Peaks of varying absorption were simulated. The plots on the top show the transmission signal (blue) and the result after deconvolution (orange). The deconvoluted signal is converted to the absorption αL using the equation $I = I_0 e^{-\alpha L}$, where I is the transmission intensity and I_0 is the input intensity. The negative feature on the left part of each peak becomes prominent with increased absorption. Also, the top of the peak is not so flat and starts to 'split' as absorption in the crystal increases. This will also be evident in Paper I, where the top of the peak at 36.9 MHz shows a similar split feature.

Several of the errors mentioned above occur since the deconvolution algorithm used here is based on linear signal processing[112], and some of the irregularities have been addressed in another work [115] based on nonlinear signal processing techniques.

Chapter 6

High fidelity transfers

This chapter concerns the transfer of population between two quantum states. Coherent control of atoms is imperative for efficient population transfers since incoherent radiation can result in, at best, an efficiency of 50%. Coherent resonant pulses result in Rabi oscillation of the population between the two states but are highly sensitive to errors in pulse areas.

There are several challenges in designing pulses for highly efficient population transfers in RE systems:

1. The pulse needs to be robust against variations in pulse area or variations in Rabi frequency. The variation can result from various factors, as will be detailed in Sec. 6.3.4.
2. The pulse needs to work well all across the ensemble qubit width with minimal off-resonant excitations.
3. Population needs to be transferred between two hyperfine states via an electronically excited state which has a finite coherence time. Thus, the time for which the excited state is occupied needs to be minimized in order to limit dephasing errors.
4. An additional challenge in working with Eu^{3+} is that it has a low transition dipole moment and thus there is a cap on attainable Rabi frequencies due to limited laser power.

Problems (1), (2), and (4) can be solved by pulses based on adiabatic following [116, 117]. Paper III follows this approach by using ‘sechscan’ pulses. Composite pulses

[118, 119] are also robust albeit long. Problem (3) above can be solved by designing short pulses, a solution offered by hard resonant pulses but they are not robust against inhomogeneities. Several techniques combine the speed of resonant pulses and robustness of adiabatic pulses, for example, optimal control theory [58, 120] and ‘Shortcut to Adiabaticity’ [121, 122]. While different techniques [123–125] exist to achieve a shortcut to adiabaticity, the approach used in Paper II is a combination of inverse engineering based on Lewis-Reisenfeld (LR) invariants and optimization of pulse parameters.

This chapter is structured in the following manner: First, the Lindblad master equation is introduced, which will be used in all the simulations in this chapter. Then, the concepts involved in Paper II are described - ‘LR invariant’, ‘inverse engineering’, and ‘shortcut to adiabaticity’. The main results of Paper II are discussed. Then, the focus of this chapter shifts to Paper III. The compromises to be made in order to design an experiment to achieve high fidelity are discussed. The results of simulations and experiments in Paper III are summarized.

6.1 Evolution of a quantum system using Lindblad equation

In this section, the evolution of a two-level quantum system is described. A simple description using two levels is given but the concept can be extended to all the simulations in this chapter. The need for using the Lindblad equation is briefly motivated and two examples are shown, where this equation is relevant.

A quantum state evolves in time according to the Schrödinger equation:

$$i\hbar \frac{\partial}{\partial t} |\psi(t)\rangle = H(t) |\psi(t)\rangle \quad (6.1)$$

where $\psi(t)$ is the wave-function of a pure state and $H(t)$ is the system Hamiltonian. The simulations in this chapter involve ensembles, so the density matrix formalism is used to describe the ensemble qubit, where $\rho \equiv \sum_i p_i |\psi_i\rangle \langle \psi_i|$. For a two-level system with one ground and one excited state, $|g\rangle$ and $|e\rangle$, respectively, the density matrix is:

$$\rho = \begin{pmatrix} \rho_{11} & \rho_{12} \\ \rho_{21} & \rho_{22} \end{pmatrix} = \begin{pmatrix} |p_g|^2 & p_g p_e^* \\ p_e p_g^* & |p_e|^2 \end{pmatrix} \quad (6.2)$$

The diagonal elements $|p_g|^2$ and $|p_e|^2$ are the populations and the off-diagonal elements describe the coherences. The Schrödinger equation, Eq. 6.1 can be written using the density matrix as:

$$\dot{\rho}(t) = -\frac{i}{\hbar}[H, \rho(t)] \quad (6.3)$$

To describe any effects that include the interaction of the quantum system with the environment, Eq. 6.1 is not used since it describes closed systems without accounting for the environment. Instead, the Lindblad master equation [126] is used as a standard approach to describing the evolution of an open system, which is the combination of the quantum system and its environment.

$$\frac{d\rho}{dt} = -\frac{i}{\hbar}[H, \rho] + \sum_j [2L_j\rho L_j^\dagger - \{L_j^\dagger L_j, \rho\}] \quad (6.4)$$

where, $\{x, y\} = xy + yx$ is an anticommutator, H is the system Hamiltonian as before and represents the coherent part of the dynamics, and L_j are the Lindblad operators representing the interaction of the system with the environment, summed over ‘ j ’ interactions. Two examples of the interaction of a two-level system with the environment will be described below to show the form of the Lindblad operator used in this work [127]:

1. Pure dephasing without relaxation

Let us assume that the lifetime of the excited state $|e\rangle$ is infinite and the ground state $|g\rangle$ has infinite coherence. The dephasing is governed by the coherence time $T_{2,opt}$ of the optically excited state, $|e\rangle$. The Lindblad operator for pure dephasing in the basis $|e\rangle$ and $|g\rangle$ is:

$$L_{\text{dephase}} = \begin{pmatrix} \frac{1}{\sqrt{2T_{2,opt}}} & 0 \\ 0 & \frac{1}{\sqrt{2T_{2,opt}}} \end{pmatrix} \quad (6.5)$$

2. Relaxation without additional dephasing

Let us now assume that the lifetime of the excited state $|e\rangle$ is $T_{1,opt}$. The Lindblad operator for relaxation without pure dephasing ($T_{2,opt} = \infty$) in the basis $|e\rangle$ and $|g\rangle$ is:

$$L_{\text{relax}} = \begin{pmatrix} 0 & 0 \\ \frac{1}{\sqrt{T_{1,opt}}} & 0 \end{pmatrix} \quad (6.6)$$

All the simulations in this chapter are done using software developed in the Quantum Information group here in Lund, based on Eq. 6.4. Values of T_1 and T_2 are given in

each section when relevant. If more than two levels are used in the simulations, the decay will also be governed by the relative oscillator strengths for the transitions, as listed in Tab. 2.2.

6.2 Shortcut to Adiabaticity

6.2.1 Lewis-Reisenfeld Invariants

According to the Lewis-Reisenfeld theory [128], any linear summation of the eigenstates of an invariant is also a solution to Eq. 6.1. The shortcut method based on Lewis-Reisenfeld invariants drives the initial state (chosen to be $|1\rangle$ in this work) to the final state $|\psi_{tg}\rangle = \sin\theta |0\rangle + \cos\theta e^{i\phi} |1\rangle$, along the eigenstate of a dynamical invariant $I(t)$ such that the following condition is satisfied[123, 129]:

$$\frac{dI}{dt} \equiv \frac{\partial I(t)}{\partial t} + \frac{1}{i\hbar}[I(t), H(t)] = 0 \quad (6.7)$$

This method is employed in a three-level system, as shown in Fig. 6.1(a). The Hamiltonian with the rotating wave approximation in the basis $|1\rangle$, $|e\rangle$ and $|0\rangle$ is:

$$H(t) = -\frac{\hbar}{2} \begin{bmatrix} 0 & \Omega_p(t)e^{i\phi} & 0 \\ \Omega_p(t)e^{-i\phi} & 0 & \Omega_s(t) \\ 0 & \Omega_s(t) & 0 \end{bmatrix} \quad (6.8)$$

, where $\Omega_i = \frac{\mu_i E_i}{\hbar}$ ($i = p, s$) is the Rabi frequency, μ is the transition dipole moment, E is the electric field of the laser and ϕ is the phase applied to the field Ω_p .

The invariant $I(t)$, is given by:

$$I(t) = \frac{\hbar\Omega_0}{2} \begin{bmatrix} 0 & \cos(\gamma) \sin(\beta) e^{i\phi} & -i \sin(\gamma) e^{i\phi} \\ \cos(\gamma) \sin(\beta) e^{-i\phi} & 0 & \cos(\gamma) \cos(\beta) \\ i \sin(\gamma) e^{i\phi} & \cos(\gamma) \cos(\beta) & 0 \end{bmatrix} \quad (6.9)$$

, where Ω_0 is a constant in units of frequency, γ and β are auxiliary parameters. $I(t)$ has three eigenstates and one is chosen for this work, given by:

$$|\phi_0(t)\rangle = \begin{bmatrix} \cos(\gamma) \cos(\beta) e^{i\phi} \\ -i \sin(\gamma) \\ -\cos(\gamma) \sin(\beta) \end{bmatrix} \quad (6.10)$$

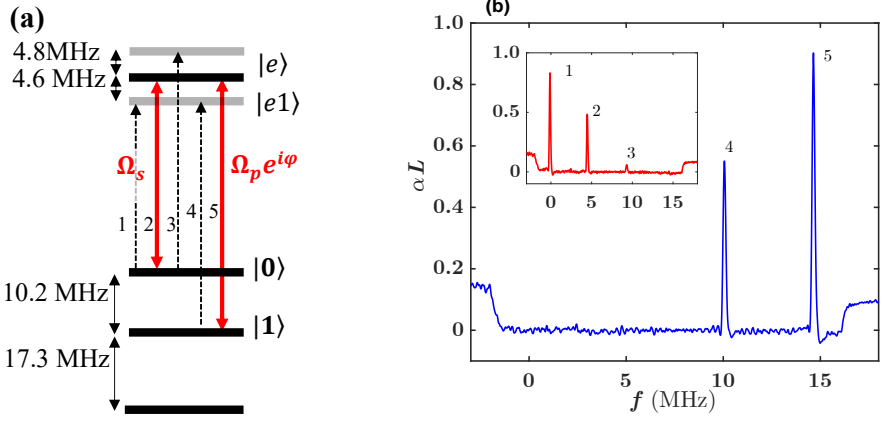


Figure 6.1: (a) The qubit is represented by ground state levels $|0\rangle$ and $|1\rangle$. They are coupled through optical transitions $|0\rangle \rightarrow |e\rangle$ and $|1\rangle \rightarrow |e\rangle$, driven with Rabi frequencies Ω_s and Ω_p , respectively. (b) Absorption spectrum showing the qubit initialized in $|1\rangle$, represented by the peaks ‘4’ and ‘5’. The inset shows the qubit in $|0\rangle$, represented by the peaks ‘1 - 3’.

One can ensure that $H(t)$ drives the initial state $|1\rangle$ along $|\phi_0(t)\rangle$ such that it coincides with the final state $|\psi_{tg}\rangle$. This is done by imposing some boundary conditions and engineering the functional form of Ω_p and Ω_s , based on the restrictions of the physical system. This is termed ‘inverse engineering’ and is discussed in the next section.

6.2.2 Inverse engineering

The physical system used was 0.5% doped $\text{Pr}^{3+}:\text{Y}_2\text{SiO}_5$ and the transition was $^3\text{H}_4 \rightarrow ^1\text{D}_2$ at 606 nm. The hyperfine structure of this transition and the qubit levels are marked in Fig. 6.1(a). The different conditions considered for the ‘inverse engineering’ of transfer pulses in this work are:

1. To ensure the initial state is $|1\rangle$ and the final state is an arbitrary superposition state $|\psi_{tg}\rangle = \sin\theta |0\rangle + \cos\theta e^{i\phi} |1\rangle$, the boundary conditions chosen are: $\gamma(0) = 0, \gamma(t_f) = \pi, \beta(0) = 0, \beta(t_f) = \pi - \theta$ [124].
2. There is some freedom to choose the functional form of the auxiliary parameters γ and β as long as they satisfy the above boundary conditions [124]. The form

chosen in Paper II are:

$$\gamma(t) = \frac{\pi}{t_f} \sum_{n=1}^{n=8} a_n \sin\left(\frac{n\pi}{t_f} t\right) \quad (6.11)$$

$$\beta(t) = \frac{(\pi - \theta)}{2} [1 - \cos \gamma(t)] \quad (6.12)$$

Practically, the various sinusoidal components are generated using Acousto-optic-modulators. Starting from Eqn.6.7, 6.8 and 6.9, the form of the Rabi frequencies can be written as:

$$\Omega_p = -\dot{\gamma}(t)[(\pi - \theta) \cos \gamma(t) \sin \beta(t) + 2 \cos \beta(t)] \quad (6.13)$$

$$\Omega_s = -\dot{\gamma}(t)[(\pi - \theta) \cos \gamma(t) \cos \beta(t) - 2 \sin \beta(t)] \quad (6.14)$$

3. One can also ensure that the pulses start and end at zero amplitude so that there are no unwanted frequency components. Thus, $\Omega_p(0) = \Omega_p(t_f) = 0$ and $\Omega_s(0) = \Omega_s(t_f) = 0$. This implies the following conditions:

$$a_1 + 3a_3 + 5a_5 + 7a_7 = 0 \quad (6.15)$$

$$a_2 + 2a_4 + 3a_6 + 4a_8 = -0.5 \quad (6.16)$$

As long as the above conditions Eq. 6.11, 6.15 and 6.16 on the values of a_n are satisfied, a transfer is achieved from $|1\rangle$ to $|\psi_{tg}\rangle$. However, to ensure high transfer efficiencies that are robust against the imperfections in the system, one should optimize the values of a_n . The optimization was done using a simulation of a six-level system, which includes the optical inhomogeneity of the Pr ions and the optical lifetime and coherence time, listed in Tab. 2.2. The fidelity was maximized for a region of ions within ± 500 kHz of the ensemble peak while minimizing any effect on the population of ions outside the TSW (discussed in Sec. 5.2). The pulse length was set to $t_f = 4 \mu s$ and the shape of the optimized pulses is shown in Fig. 6.2. Three cases of transfers were considered in this work:

- Case 1: $|1\rangle \rightarrow |0\rangle$. The envelopes and phases of Ω_p and Ω_s are interchanged for transfers from $|0\rangle \rightarrow |1\rangle$.
- Case 2: $|1\rangle \rightarrow |\psi_{tg}^{sup}\rangle$. The ' a_n ' parameters are the same for any superposition state but a different constant phase $e^{i\phi}$ is applied to Ω_p depending on the target final state.
- Case 3: $|\psi_{tg}^{sup}\rangle \rightarrow |1\rangle$

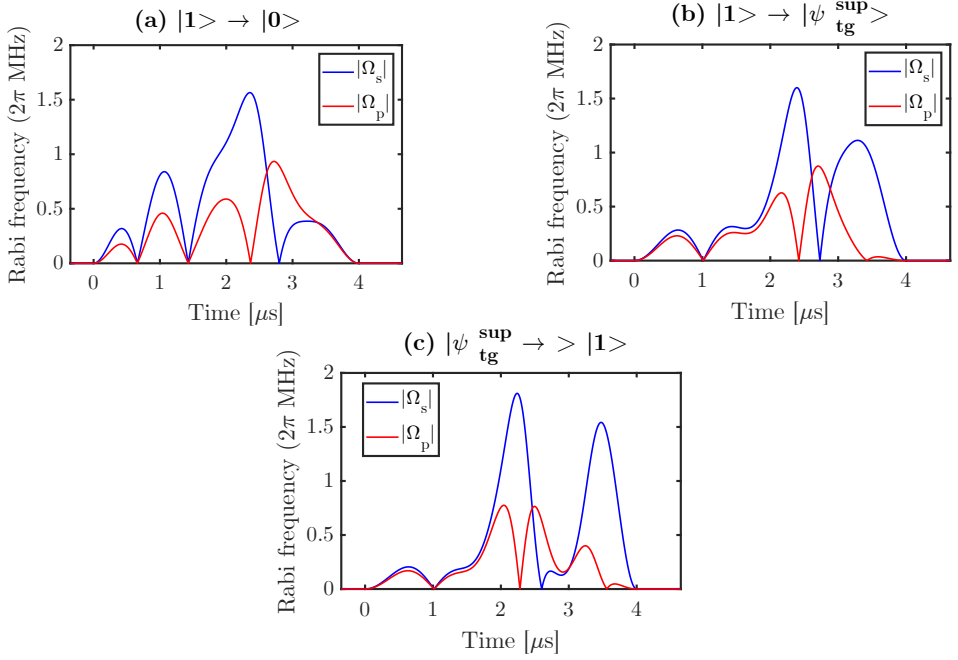


Figure 6.2: Profile of the pulses used for the shortcut transfers. Ω_s and Ω_p are the Rabi frequencies which couple the optical transitions $|0\rangle \rightarrow |e\rangle$ and $|1\rangle \rightarrow |e\rangle$, respectively. (a) Transfer from $|1\rangle \rightarrow |0\rangle$ (b) Transfer from $|1\rangle \rightarrow |\psi_{tg}^{sup}\rangle$. (c) Transfer from $|\psi_{tg}^{sup}\rangle \rightarrow |1\rangle$.

6.2.3 Experimental implementation

This section describes the steps involved in implementing the method of inverse engineering Shortcut to Adiabaticity based on LR invariants in experiments with rare-earth-ion-doped crystals. The experimental setup used is described in Paper II. A schematic of the pulse sequences used is shown in Figure 6.3. Each step is described below:

1. **Create a TSW:** A transparent spectral window (TSW) is first created. The basic principle involved here is optical pumping, where the ions are shelved into a third ground state outside the TSW, which is not involved in the qubit operations (see Sec. 5.2). This window remains transparent for several seconds, which is much longer than the operations to follow.
2. **Create a qubit in state $|1\rangle$:** An ensemble qubit of width 170 kHz is created in $|1\rangle$, by burning back some ions from the third ground state. A qubit initialized in $|1\rangle$ has two absorption peaks inside the TSW, shown in blue in Figure 6.1(b).

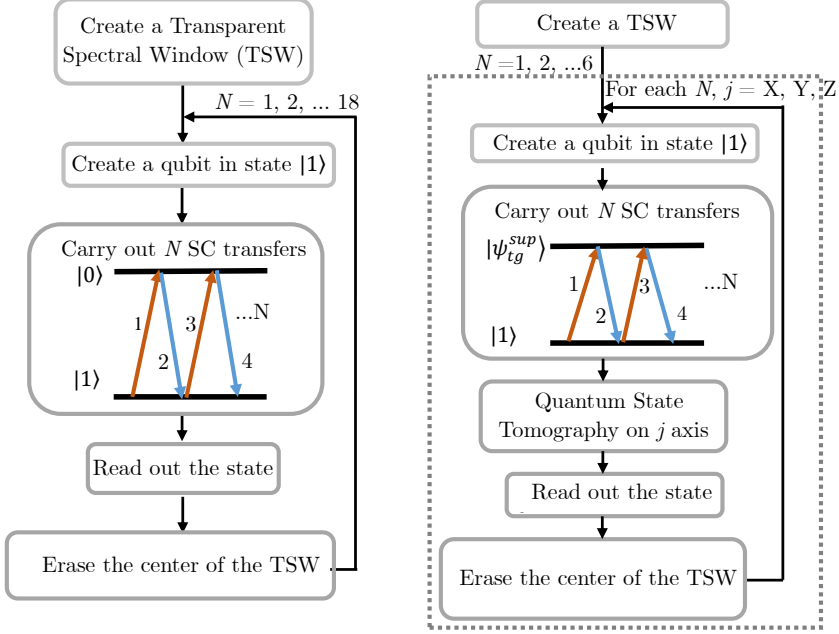


Figure 6.3: Schematic of the pulse sequence used in the experiments. SC stands for shortcut. Steps on the left show the case for transfers between $|1\rangle \leftrightarrow |0\rangle$ and on the right, the case for transfers between $|1\rangle \leftrightarrow |\psi_{tg}^{sup}\rangle$ is shown.

3. **Perform Shortcut transfer:** ‘N’ consecutive transfers are performed between $|1\rangle$ and the target state using the shortcut pulses described earlier. The target state is either $|0\rangle$ or one of the four superposition states $(|0\rangle + |1\rangle)/\sqrt{2}$, $(|0\rangle - |1\rangle)/\sqrt{2}$, $(|0\rangle + i|1\rangle)/\sqrt{2}$ or $(|0\rangle - i|1\rangle)/\sqrt{2}$.
4. **Readout:** A frequency scanning pulse of low intensity is used to read out the populations in $|0\rangle$ and $|1\rangle$. If a superposition state is being read out, full Quantum State Tomography [21] is performed before reading out the state.
5. **Erase the center of the TSW:** Strong pulses are sent in to erase the center of the TSW, resetting the conditions to step 2 above. Thereafter, the above procedure is repeated until ‘N’ transfers are completed.

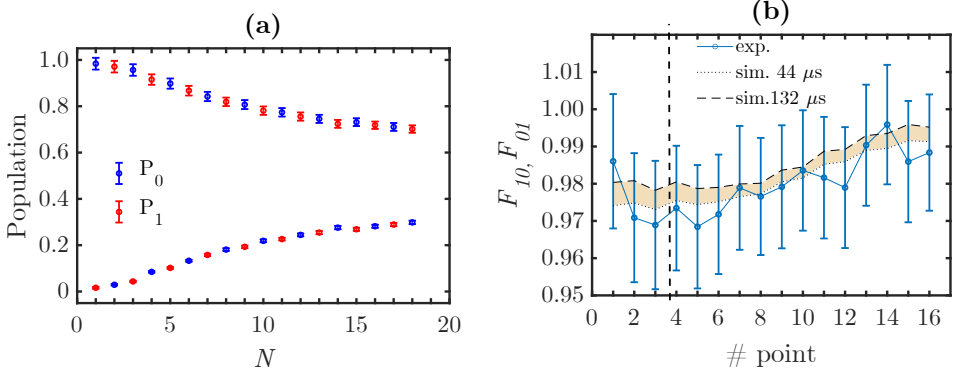


Figure 6.4: Results of population transfer between $|1\rangle$ and $|0\rangle$. (a) Populations in $|1\rangle$ and $|0\rangle$ are shown in red and blue respectively. (b) Fidelity of transfer, F_{01} (equal to F_{10}): Blue line is calculated from experiments and the shaded region is a result of simulation.

6.2.4 Experimental results

6.2.4.1 Transfers between two ground states

The results of population transfer between $|1\rangle$ and $|0\rangle$ are shown in Fig. 6.4(a). The decoherence error increases with the number of transfers as the time spent by ions in the excited state increases. Additionally, a small portion of the total population is lost to the third ground state as the number of transfers increases. In Fig. 6.4(b), the operational Fidelity F_{01} or F_{10} is plotted using the product $F_{01}F_{10}$ in the following equation:

$$F_{01}F_{10} = \frac{F(N+2)}{F(N)}, N = 1, 2, 3 \dots 16 \quad (6.17)$$

The above equation is an approximation that holds true for the first six transfers or the first four points in Fig. 6.4(b). The average fidelity for these points is $97 \pm 2\%$. The shaded region is the result of the simulation assuming two different optical coherence times, 44 μs and 132 μs . This range is chosen to account for the effects of instantaneous spectral diffusion[72], whereby the coherence time of some ions in the ensemble qubit is affected by the excitation of their neighboring ions due to dipole-dipole interaction.

6.2.4.2 Transfer between ground and superposition state

For reading out a superposition state, QST is performed but the two-color pulses used for QST can have state-dependent errors resulting in a fidelity of about $\sim 95\%$.

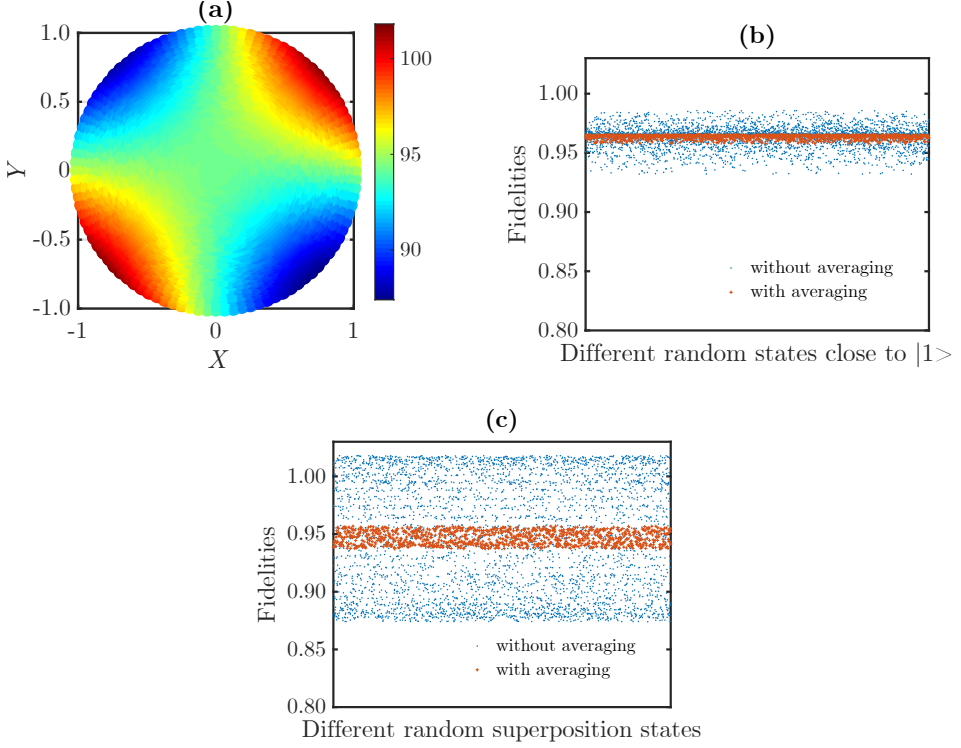


Figure 6.5: (a) QST fidelity of reading out a superposition state randomly located in the XY plane of the Bloch sphere (b)QST fidelity of randomly generated states close to $|1\rangle$ (c) QST fidelity of randomly generated superposition states, with and without averaging.

This needs to be accounted for before calculating the operational fidelity. Results of simulating the error due to the tomography pulses are shown in Fig. 6.5. The QST fidelity for reading out a state depends on the angle by which the state is rotated, with respect to the $+X$, $+Y$, $-X$, and $-Y$ axes (see Fig. 6.5(a)). However, when the fidelity due to reading out the states rotated by the same angle with respect to the $+X$, $+Y$, $-X$, and $-Y$ axes are averaged, the error is drastically reduced. The error is larger for superposition states (see Fig. 6.5(c)) than for states close to the ground state $|1\rangle$ (see Fig. 6.5(b)). Thus, it was concluded that the QST error can be minimized if the fidelity of creating all four superposition states was averaged. The average fidelity, $F(N)$, is shown in Fig. 6.6(a). This depends on the fidelity of transfer from $|1\rangle \rightarrow |\psi_{tg}^{sup}\rangle$, F_{1s} , the fidelity of transfer from $|\psi_{tg}^{sup}\rangle \rightarrow |1\rangle$, F_{s1} , and the fidelity of QST for reading out superposition and ground states, QT_s and QT_1 respectively. $F(N)$ is given as:

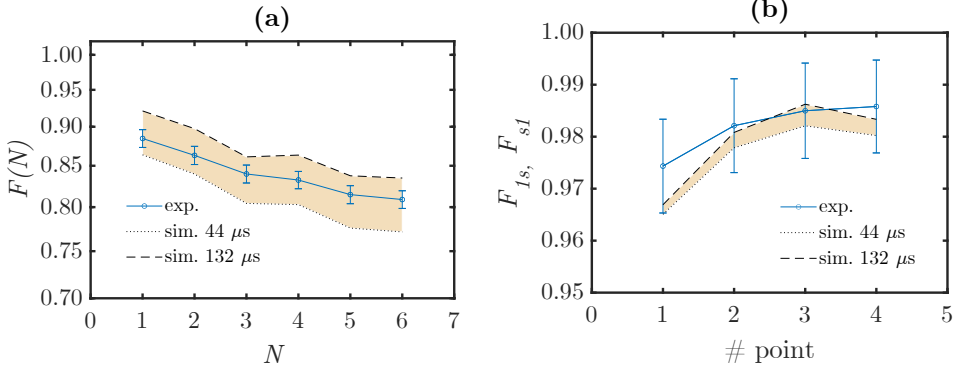


Figure 6.6: Results of transfer between $|1\rangle$ and $|\psi_{tg}^{sup}\rangle$ (a) The fidelity $F(N)$ (including the QST fidelity) as a function of the number of transfers. (b) The calculated transfer fidelity F_{1s} or F_{s1} . The simulations are shown with a shaded region and are done using two values of coherence times, $44 \mu s$ and $132 \mu s$.

$$F(N) = F_{1s}^{(N+1)/2} F_{s1}^{(N-1)/2} QT_s, \quad N = 1, 3, 5 \quad (6.18)$$

$$F(N) = F_{1s}^{N/2} F_{s1}^{N/2} QT_1, \quad N = 2, 4, 6 \quad (6.19)$$

The division of $F(N+2)/F(N)$ gives the product $F_{1s}F_{s1}$:

$$F_{1s}F_{s1} = F(N+2)/F(N), \quad N = 1, 2, 3, 4 \quad (6.20)$$

Assuming $F_{1s} = F_{s1}$, the fidelity for transfer between $|1\rangle$ and $|\psi_{tg}^{sup}\rangle$ can be obtained and is shown in Fig. 6.6(b). The average value is $98 \pm 1\%$.

6.2.5 Conclusions

The experiments in Paper II are an implementation of a protocol that combines inverse engineering based on LR invariants and optimization of transfer pulse parameters. The main advantage of this method is that the known boundary conditions i.e., the known initial and target states, allow the use of shorter pulses and thus minimize the dephasing errors. In comparison with an earlier work [21], the error in fidelity is reduced from $\sim 7\%$ to 2% . Although the shortcut pulses used here cannot be used to perform arbitrary gate operations, they can be used, for example, in the state initialization of ancilla qubits in a quantum error correction protocol. Additionally, state-dependent errors of the pulses used for QST were identified and characterized.

6.3 Adiabatic Approach

This section describes the technical and fundamental challenges towards achieving high fidelities in REQC using ensemble qubits in $^{151}\text{Eu}^{3+}:\text{Y}_2\text{SiO}_5$. An adiabatic approach is employed by designing long pulses that do not need very high laser intensities. The section begins by describing the material properties of $^{151}\text{Eu}^{3+}:\text{Y}_2\text{SiO}_5$ and the reasons for choosing this crystal. Then, the details of the power budget which leads to limited Rabi frequency as well as its variation across the crystal are outlined. The pulses used for creating ensemble qubits, the design of efficient state transfers robust against variations in Rabi frequency, and the details of shot noise limited detection are also given. Experimental results of state transfers and gate operations are presented. The section ends with comments on limitations that are relevant for achieving high fidelity in ensemble qubits.

6.3.1 Choice of material

$^{153}\text{Eu}^{3+}:\text{Y}_2\text{SiO}_5$ at site 1 is considered the best candidate for high-fidelity gate operations in the Roadmap for rare-earth quantum computing [13]. It has long optical [68] and spin coherence times [86] and a large separation between the energy levels that allow for shorter pulses in time to minimize gate errors. However, the required frequency bandwidth could not be achieved experimentally (explained in Sec. 6.3.3). So another isotope, $^{151}\text{Eu}^{3+}$ with lower energy splitting between the qubit levels was used. The transition used was $^5\text{D}_0 \rightarrow ^7\text{F}_0$ transition in $^{151}\text{Eu}^{3+}:\text{Y}_2\text{SiO}_5$, site 1 at 580 nm, shown in Figure 6.7. The transitions $|\frac{1}{2}g\rangle \rightarrow |\frac{5}{2}e\rangle$ and $|\frac{3}{2}g\rangle \rightarrow |\frac{5}{2}e\rangle$, with relative oscillator strengths of 0.75 and 0.20, respectively are used for qubit manipulation and are marked in blue. The transitions marked in red, $|\frac{5}{2}g\rangle \rightarrow |\frac{1}{2}e\rangle$ and $|\frac{3}{2}g\rangle \rightarrow |\frac{1}{2}e\rangle$ were used for initializing the qubit in $|1\rangle$ using optical pumping. Relevant optical properties are listed earlier in Section 2.5.

6.3.2 Trade-off in experimental design

There are several things to think about while designing an experiment to measure high fidelity. These are discussed below:

1. **Absorption Signal:** To maximize the signal, a sample with maximum absorption should ideally be chosen. Ref. [68] shows the dependence of absorption coefficient and optical inhomogeneous linewidth on the doping concentration of Eu ions. While the optical inhomogeneous broadening increases with concentration, the absorption coefficient does not change very much for concen-

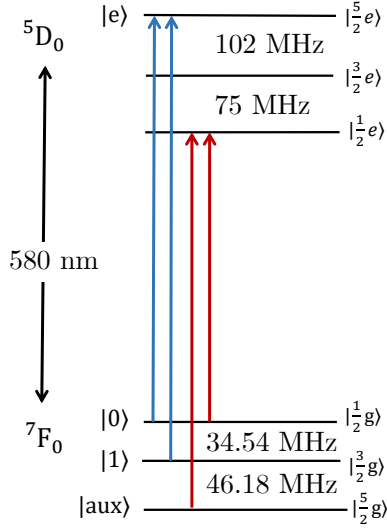


Figure 6.7: Hyperfine structure of the $^5D_0 \rightarrow ^7F_0$ transition at 580 nm in $^{151}\text{Eu}:\text{YSO}$, site 1. The transitions marked in blue are used for qubit manipulation and red are used for initializing the qubit in $|1\rangle$.

trations between 0.1 and 1%. This means that a higher concentration increases the number of qubit channels but the absorbed signal does not simultaneously increase. Additionally, a higher concentration can also result in a larger spin inhomogeneity, causing more gate errors (This will be discussed later in Section 6.3.8). Thus, it is a balance between maximizing the absorption signal and minimizing gate errors, so 0.1% is ideal.

2. **Crystal length:** The length of the crystal determines how large the absorption signal, αL can be. A longer crystal would increase the absorption signal but also increases the inhomogeneity in Rabi frequency across the length of the crystal. For a doping concentration of 0.1%, the expected absorption at the center of the inhomogeneous linewidth is $\alpha = 3.5 \text{ cm}^{-1}$ [68]. After optical pumping for the qubit initialization process, the expected absorption from the qubit peak is reduced to about one-third of this value. Due to the different relative oscillator strengths (0.75 and 0.2), the expected absorption signal for the qubit two peaks in $|0\rangle$ and $|1\rangle$ is respectively, $\alpha_{|0\rangle} = 0.88 \text{ cm}^{-1}$ and $\alpha_{|1\rangle} = 0.23 \text{ cm}^{-1}$. If the crystal length is at least 5 mm, $\alpha L_{\text{signal},|0\rangle} \sim 0.43$ and $\alpha L_{\text{signal},|1\rangle} \sim 0.11$.
3. **SNR:** The detection is ensured to be limited by shot noise since the readout power normally used is $\sim \mu\text{W}$. The readout is done using chirped techniques [112]. Since the chirp is fast, the transmission signal from the crystal contains

Free Induction Decay from the qubit peak, which needs to be deconvoluted. The SNR after this step needs to be good enough to measure high fidelity. This work aims to achieve an SNR of at least 10 when the qubits are initialized in $|1\rangle$ and $|0\rangle$. The upper limit on the noise floor can be estimated as below:

$$\alpha L_{noise} \leq \frac{\alpha L_{signal}}{SNR}$$

4. **Rabi frequency:** Optical coherence time is long for the chosen material but it also means that the oscillator strength is low and relatively high laser intensity is required to drive the transition. Two ways to maximize the Rabi frequency from the available laser power are to focus tightly and place the crystal in a cavity (for example, by coating the surfaces with reflective material).

The first method leads to inhomogeneity in Rabi frequency in the longitudinal direction. The transfer pulses can be designed to work well beyond a threshold Rabi frequency and the transfer efficiency will be limited by the ions experiencing a Rabi frequency lower than the threshold (discussed in Sec. 6.3.6). The second method of using a cavity leads to standing waves in the crystal. At the position of nodes, there will be no absorption of light by ions. Thus, this option is not ideal.

Optimizing the above factors independently does not always lead to minimizing errors since the factors are interconnected. One could choose a longer crystal to increase the absorption signal and use a very tight focus to maximize Rabi frequency but both options increase the inhomogeneity in Rabi frequency. One could also increase the doping concentration but there is also evidence that spin inhomogeneous broadening increases with concentration (discussed in detail in Sec. 6.3.8) and can decrease gate fidelity. There is thus a trade-off to be made in choosing various values to obtain optimal transfer efficiencies. In the next section, the choices made for the setup and consequent challenges are discussed.

6.3.3 Technical challenges and experimental setup

The chosen sample was an isotopically pure bulk crystal of $^{151}\text{Eu}^{3+}$ (site 1) with dimensions $5 \times 5 \times 8$ mm along the crystal axes b , D_1 and D_2 , respectively and light propagated along the b axis. The electric field of light was chosen to be parallel to the crystal axis D_1 since it has a higher absorption coefficient than the other two axes [68]. The absorption coefficient was measured to be 2.7cm^{-1} along D_1 . There was also an attempt at using a shorter crystal, of length 3 mm (0.1% concentration, grown in P. Goldner's group in Paris) but the absorption signal was much lower than expected. Thus, this sample was not investigated further.

Eu:YSO has a long optical coherence time but this also means that the oscillator strength is rather weak. Thus, it is difficult to drive the chosen transition and requires high laser intensity. The maximum laser power from the dye laser used for these experiments is ~ 1 W at 580 nm but this is reduced to 30 mW at the position of the crystal, thus aggravating the problem of the availability of enough laser power to drive the transitions. C.D Hobbs aptly said [114] :

Photons are like money: A certain number are needed for the job at hand, and they're easier to lose than to gain back.

The various stages of power losses are listed below:

- A PM (polarization-maintaining) fiber needs to be used directly after the laser output to clean the mode before being guided to the AOMs (Acousto-optic modulator). This step eats away $\sim 50\%$ of the power but improves the spatial mode coupling to AOM1.
- AOM1 is used in double-pass configuration to avoid the 'beam walk' seen in single-pass when the frequency is changed. This also increases the frequency bandwidth but the diffraction efficiency can, at best be about 50%. Thus we have about 250 mW remaining.
- AOM2 is used to create the two-color pulses separated by 34.5 MHz. A challenge here is to overlap the two colors in the crystal. An alternate method is to couple both colors simultaneously into a PM fiber which will also clean the mode. This requires a short focal length of 75mm, giving a focal spot size of $100\mu\text{m}$ inside the AOM. Although the quoted diffraction efficiency is about 80%, practically only about 60% was achieved. If we wish to increase the bandwidth to more than 34.5 MHz, the diffraction efficiency of AOM's reduces further.
- The experimental fiber, has a coupling efficiency of only 50%, probably due to sub-optimal spatial modes after the AOMs. Thus, only about 75 mW is obtained on the cryostat table.
- Further loss due to polarization optics and cryostat windows occur and at the crystal position inside the cryostat, about 30 mW is available.

Limited laser power requires focusing of the beam at the center of the crystal to maximize the intensity and hence the available Rabi frequency. There is a limit on how tight the focus can be since a tighter focus also results in a larger variation in intensity across the length of the crystal. For this experiment, the focus was decided so that the length of the crystal x_L is less than twice the Rayleigh length z_R given by $z_R = \frac{n\pi w_0^2}{\lambda}$,

where w_0 is the beam waist radius and λ is the wavelength of light in vacuum and n is the refractive index of YSO (1.8). Since $x_L = 5$ mm (along crystal axis b), the beam waist radius was decided to be $w_0 = 20$ μm which has a Rayleigh length $z_R = 3.9$ mm. The expected maximum intensity at the focal plane is:

$$I = \frac{1}{2} \epsilon_0 n c \left(\frac{\Omega \hbar}{\mu \sqrt{f_{\text{rel}}}} \right)^2$$

and thus the Rabi frequency is:

$$\Omega = \frac{\mu \sqrt{f_{\text{rel}}}}{\hbar} \sqrt{\frac{2}{\epsilon_0 n c} \frac{P}{\pi w_0^2}}$$

, where ‘P’ is the available power (about 30 mW), ‘n’ is the refractive index of YSO, w_0 is the beam waist radius, μ is the optical transition dipole moment for the transition $^7\text{F}_0 \rightarrow ^5\text{D}_0$ (7.2×10^{-33} Cm) and ‘ f_{rel} ’ is the relative oscillator strength. For the strongest transition i.e., $|0\rangle \rightarrow |e\rangle$ with relative oscillator strength 0.8, the available Rabi frequency was $\Omega = 890$ kHz, and for the weakest transition i.e., $|1\rangle \rightarrow |e\rangle$ with relative oscillator strength 0.2, $\Omega = 445$ kHz. After the above considerations, the setup used in the experiments is detailed in Paper III.

6.3.4 Inhomogeneity in Rabi Frequency

Tight focusing of light in the crystal leads to a large variation across the crystal length due to Gaussian propagation. In addition, light is absorbed as it propagates a distance ‘L’ through the crystal, estimated by the equation $I = I_0 e^{-\alpha L}$. Figure 6.8 shows the variation in intensity due to Gaussian propagation in free space and in an absorbing medium ($\alpha_{|0\rangle} = 0.88 \text{ cm}^{-1}$). Edges of the crystal are shown as red lines at ± 2.5 mm. After absorption, the intensity varies between $0.83I_0 - 0.46I_0$ (shown as a solid black line) and the Rabi frequency is $0.91\Omega_0 - 0.68\Omega_0$ since it scales with intensity as $\Omega = \sqrt{I}$ (shown as solid blue line). A similar calculation for $\alpha_{|1\rangle} = 0.23 \text{ cm}^{-1}$ results in a variation from $0.97I_0 - 0.80I_0$ and $0.94\Omega_0 - 0.64\Omega_0$. For the strongest transition, it drops to the range 605 – 810 kHz and for the weakest transition, it drops from 445 kHz to the range 284 – 418 kHz. The transfer pulses can be designed to work well beyond a threshold Rabi frequency. However, the transfer efficiency will still be limited by the ions experiencing Rabi frequency lower than the threshold in the wings of a Gaussian beam in the transverse direction.

Since the beam has a Gaussian profile, there is also variation in intensity in the transverse plane. The transfer pulses will not work efficiently for the ions sitting at the wings of this Gaussian profile. In previous works where the focal spot diameter was

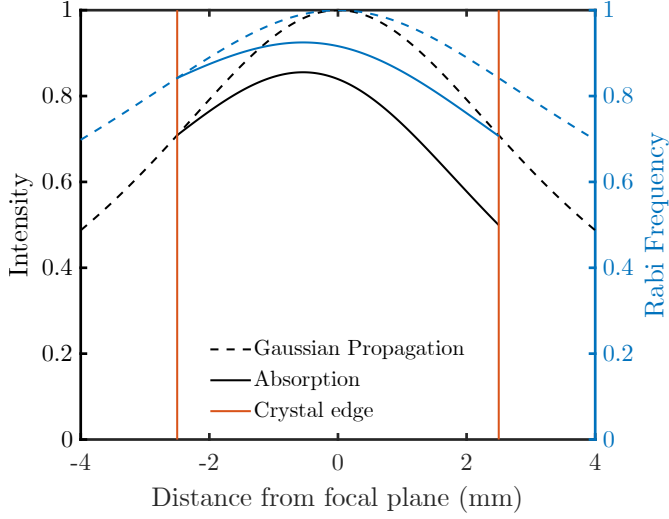


Figure 6.8: Variation in intensity for a Gaussian beam focused down to a spot with a diameter $40\text{ }\mu\text{m}$. The intensity drops by 50% at a distance equal to its Rayleigh length $z_R = 3.9\text{ mm}$, shown as the black dashed line. By introducing the crystal (red lines), a further drop in intensity occurs due to absorption, shown as the solid black line. The lines in blue show a similar drop in Rabi frequencies.

$100\text{ }\mu\text{m}$ [21, 56], this problem was solved by imaging the central portion of the beam using a $50\text{ }\mu\text{m}$ pinhole, where the intensity varied by less than 20%. Using a similar spatial filtering technique could be difficult here since the focal spot is quite small and a pinhole would reduce the signal further.

6.3.5 Creating and reading out ensemble qubits

It is possible to empty a spectral region of $\pm 2.8\text{ MHz}$ around $|0\rangle$ and -14.3 to $+5.8\text{ MHz}$ around $|1\rangle$. An ensemble qubit of width 100 kHz was created, also using optical pumping with many weak sechyp pulses targeting $|\frac{5}{2}g\rangle \rightarrow |\frac{1}{2}e\rangle$ and $|\frac{1}{2}g\rangle \rightarrow |\frac{1}{2}e\rangle$, thus shelving ions to $|\frac{3}{2}g\rangle$. Any unwanted ions absorbing close to the qubit transition at $|\frac{3}{2}g\rangle \rightarrow |\frac{5}{2}e\rangle$ were cleaned away. The sechyp pulse parameters used for creating the qubit peak were $f_{\text{width}} = 60\text{ kHz}$, $t_{\text{fwhm}} = 30\text{ }\mu\text{s}$, $t_{\text{cutoff}} = 105\text{ }\mu\text{s}$, $|\Omega_0|_{\text{max}} = 30\text{ kHz}$, where t_{cutoff} is the total duration of the pulse. The definitions of these parameters follow from Sec. 5.1.1. The profile shape in amplitude and frequency is shown in Figure 5.1(a) and the population transferred to the excited state is shown in Figure 6.9. In the experiments, the width of the peak created using this pulse was broader than f_{width} since this sechyp pulse was repeated several times to create the peak (see

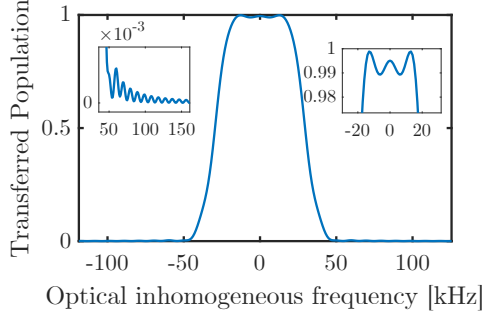


Figure 6.9: Population transferred from ground to excited state using the sechyp pulse shown in Fig. 5.1(a), with insets showing details zoomed into different spectral regions.

Sec. 5.2). The width was measured to be 93 kHz.

For the readout, we used $50 \text{ kHz}/\mu\text{s}$, which has a frequency resolution of $f_R = 30 \text{ kHz}$. The Rabi frequency of the readout pulse was less than 3% of a π pulse so as to minimize disturbing the spectral feature.

6.3.6 Transfer Pulse design

The pulse parameters were optimized using a two-level simulation to include the effects of dephasing, decay, and robustness against inhomogeneity in optical and Rabi frequencies. The aim here is to invert a 300 kHz wide peak and it should work well for a Rabi frequency of 284 kHz and above. Thus, f_{width} and f_{scan} were both fixed to 300 kHz and the other parameters were optimized manually to achieve the highest fidelity by numerically solving the Lindblad master equation (see Eq. 6.4). The simulation here was done in a two-level system with one ground and excited state, with a lifetime of 1.9 ms and coherence time $400 \mu\text{s}$. During the optimization, there is a trade-off to be made between having a short pulse, which reduces the dephasing errors, and a long pulse, which is necessary if the available laser power is low. Manual optimization of the parameters resulted in the following parameters: $f_{\text{width}} = 300 \text{ kHz}$, $f_{\text{scan}} = 300 \text{ kHz}$, $t_{fwhm} = 1.75 \mu\text{s}$, $t_{\text{cutoff}} = 14 \mu\text{s}$. The pulse profile is plotted in Figure 5.1(b) using $|\Omega_0|_{\text{max}} = 0.5 \text{ MHz}$. The transfer efficiency due to a single transfer pulse from $|g\rangle \rightarrow |e\rangle$ as a function of Rabi frequency is plotted in 6.10. The pulse works rather poorly for $|\Omega_0| < 0.2 \text{ MHz}$ but for higher values, one can expect efficiencies between 0.97 – 0.992.

We now look at the performance of this pulse for two consecutive transfers: $|1\rangle \rightarrow |e\rangle$ and $|e\rangle \rightarrow |0\rangle$, repeated ‘N’ times. The simulation was done using the four lev-

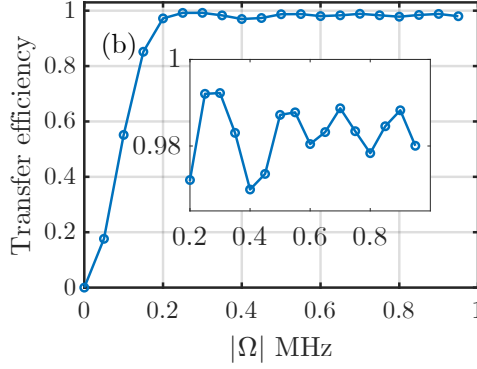


Figure 6.10: Transfer efficiency of the sechscan pulse shown in Fig. 5.1(b), as a function of its Rabi frequency amplitude Ω in the range 0-1 MHz.

els $|\frac{5}{2}e\rangle$, $|\frac{1}{2}g\rangle$, $|\frac{3}{2}g\rangle$ and $|\frac{5}{2}g\rangle$, as described in Sec. 6.1. The qubit peak used was a Gaussian with optical inhomogeneous broadening 93 kHz (equal to the experimentally measured value). The lifetime of optically excited state $|\frac{5}{2}e\rangle$, $T_{1,\text{opt}}$ was 1.9 ms (see Tab. 2.1) and the coherence time $T_{2,\text{opt}}$ was 400 μs (measured by P. Goldner's group). The relative oscillator strength of the three ground state levels $|\frac{1}{2}g\rangle$, $|\frac{3}{2}g\rangle$ and $|\frac{5}{2}g\rangle$ are 0.75, 0.20 and 0.05 respectively, as listed in Tab. 2.2. The sequence used in simulations is as follows:

1. Initialize qubit in $|1\rangle$.
2. Apply the pulses $|1\rangle \rightarrow |e\rangle$, immediately followed by $|e\rangle \rightarrow |0\rangle$ and wait for 10 ms to allow any ions left behind in $|e\rangle$ to relax back to the ground states $|0\rangle$, $|1\rangle$ or $|aux\rangle$.
3. Depending on whether another transfer is to be made, one of the two steps needs to follow:
 - If another transfer is to be made, send two more pulses: $|0\rangle \rightarrow |e\rangle$, immediately followed by $|e\rangle \rightarrow |1\rangle$ and a 10 ms long wait pulse.
 - If no more transfers are to be made, wait another 10 ms and read out the populations in $|0\rangle$ and $|1\rangle$. This is the end of the sequence.
4. Repeat steps 2-3.

The above sequence was repeated for up to 10 consecutive transfers in the simulations. Figure 6.11(a) shows the result for ions experiencing either the lower or the upper limits of available Rabi frequency across the crystal, as discussed earlier in Sec. 6.3.4. Red

lines indicate the population in $|1\rangle$ and the blue lines represent population in $|0\rangle$. The solid lines indicate the populations for the case of ions experiencing maximum values of $|\Omega_0|$ and $|\Omega_1|$ while the dashed lines indicate the populations for the case of ions experiencing minimum values. For the stronger transition $|0\rangle \rightarrow |e\rangle$, $|\Omega_{0,max}| = 810$ kHz and $|\Omega_{0,min}| = 605$ kHz. For the weaker transition $|1\rangle \rightarrow |e\rangle$, $|\Omega_{1,max}| = 418$ kHz and $|\Omega_{1,min}| = 284$ kHz. The region between these lines represents the range one can expect across the length of the crystal at the center of the Gaussian profile in the longitudinal direction. The effect due to variation in the transverse direction is not included in this simulation. Such variations need to be taken care of using spatial filtering in the experiments. Thus, when an ensemble of ions is probed in the crystal, one can expect 97-99% of the population transferred from $|1\rangle \rightarrow |0\rangle$ and 94-96% after the next transfer from $|0\rangle \rightarrow |1\rangle$.

There are several things to understand in Fig. 6.11(a), which are discussed in the following sections.

Effect of different relative oscillator strengths:

There is a difference in efficiency for the blue and red lines. This is due to the fact that the relative oscillator strengths for the two transitions $|0\rangle \rightarrow |e\rangle$ and $|1\rangle \rightarrow |e\rangle$ are quite different, i.e., 0.75 and 0.20. Since there is a delay of 20 ms before the readout, the ions preferentially relax to $|0\rangle$ and thus the blue lines lie higher than the red ones.

Effect of $|aux\rangle$ state

The total population, in $|0\rangle$ and $|1\rangle$ steadily declines due to the loss to the third ground state, $|aux\rangle$. This is shown clearly in Fig. 6.11(b), drawn as a black dashed line corresponding to simulations with $|\Omega_{0,max}| = 810$ kHz and $|\Omega_{1,max}| = 418$ kHz. About 0.2% of the total population is lost to $|aux\rangle$ after every transfer.

Effect of delay between transfers:

One could argue that a wait pulse between every transfer is unnecessary. State transfers or operations occur consecutively without any delay between the operations in any quantum algorithm. A standard method to infer gate errors and optimize gate fidelities in superconducting qubits, known as ‘randomized benchmarking’ [130] uses a long sequence of operations done consecutively. Thus, in order to measure the true efficiency from a sequence of transfers, there should not be any delays between the transfers and before the readout. Instead, one should do a full quantum state tomography (QST) on the state to obtain the fidelity of any gate. In the case of RE quantum computing, QST requires the ability to do arbitrary rotations on the Bloch sphere using two-color pulses, the efficiency of which is limited due to spin inhomogeneity, as will be described later in Sec. 6.3.8. In the current work, the focus is on obtaining

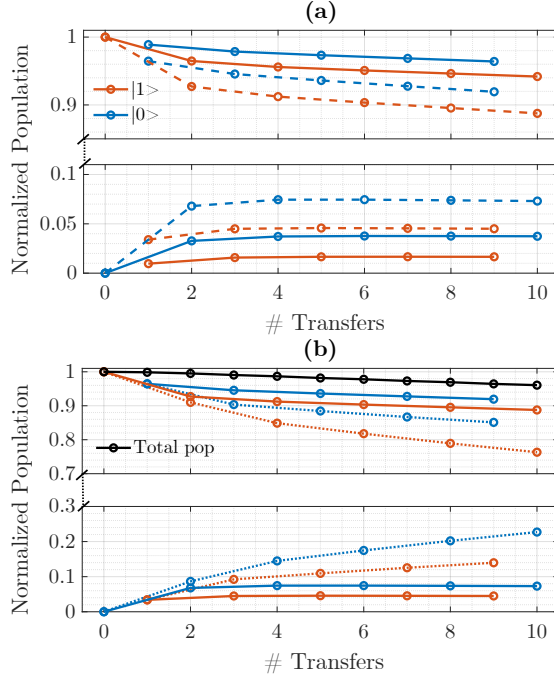


Figure 6.11: (a) Populations in $|0\rangle$ (blue) and $|1\rangle$ (red) after different numbers of state transfers, shown for the range of ions experiencing different values of Rabi frequencies across the length of the crystal. The solid lines show the case of ions experiencing maximum Rabi frequency $|\Omega_0| = 810$ kHz, $|\Omega_1| = 418$ kHz and the dashed lines show the case of ions experiencing minimum values $|\Omega_0| = 605$ kHz, $|\Omega_1| = 284$ kHz. (b) Simulations showing the effect of delay between transfers. The dashed blue and red lines correspond to the case of ions experiencing maximum Rabi frequency: $|\Omega_0| = 810$ kHz, $|\Omega_1| = 418$ kHz and 10 ms delay after each transfer between the qubit states. The dashed black line shows the corresponding total population after every transfer. The dotted lines show the same simulation without a delay of 10 ms between every transfer.

transfer efficiency only.

The result of a simulation showing the effect of a delay between transfers is shown in Fig. 6.11(b), using $|\Omega_{0,max}| = 810$ kHz and $|\Omega_{1,max}| = 418$ kHz. The dotted lines have no delay while the dashed lines show the same simulation with a delay of 10 ms between transfers. Both have a delay of 20 ms before the readout. For the case without any delay, the transfer efficiency falls quite rapidly due to build-up of errors from dephasing. For the case with the delay, any coherence between the excited state

and two ground states is lost after every transfer since the duration of delay is longer than $T_{i,\text{opt}}$ and the efficiency does not fall as fast. The population left behind after every transfer grows continuously if there is no delay (evident from the dotted lines in the bottom half of Fig. 6.11(b)). Whereas, the dashed lines remain stagnant after the first two transfers.

6.3.7 Experimental Results

Absorption profile of the ensemble qubit peaks after initializing in the states $|1\rangle$ and after one transfer to $|0\rangle$ is shown in Fig. 5.5(b). The grey line is the readout from a single shot and the blue/red lines are Gaussian fits to the mean of three data sets. The noise floor at 200 kHz to the left of each peak is about 0.015. The SNR on both peaks can now be calculated:

$$\text{SNR}_{|0\rangle} = \frac{0.358}{0.015} \approx 23 \qquad \text{SNR}_{|1\rangle} = \frac{0.097}{0.015} \approx 6$$

The above values correspond to when 100% of the population is in $|0\rangle$ or $|1\rangle$. If the population in $|1\rangle$ falls to $\frac{1}{6}$ th of this value or 16%, $\text{SNR}_{|0\rangle}$ will fall below 1. Similarly, $\text{SNR}_{|1\rangle}$ will be less than 1, if the population in $|0\rangle$ falls below 4%. For this reason, one cannot rely on looking at the population left behind in either of the states to estimate the transfer efficiency. The population transferred over to the other state will need to be the only measure of transfer efficiency.

Results of repeated transfers

Once the qubit peak is initialized in $|1\rangle$, the population was transferred to $|0\rangle$ using two sechscan pulses as described earlier in Sec. 6.3.6. After reading out the population in both states, the ions were transferred back to $|1\rangle$ and such transfers were repeated back and forth up to 100 times. The power for each pulse was adjusted experimentally so that the population transferred was maximized. It was found that the laser power required for the transfer $\Omega_{0 \rightarrow e}$ was about twice as high as in the opposite direction $\Omega_{e \rightarrow 0}$. This method of optimization had low sensitivity to the true transfer efficiency since there was a delay before readout and ions preferentially fall down to $|0\rangle$ due to the stronger relative oscillator strength. A better way to optimize the values experimentally is to do a readout immediately after the transfer pulse.

The readout was done after every transfer for the first ten transfers and subsequently, the readout was only done after the 20th, 21st, 30th, 39th, 40th, 99th, and 100th transfers. The results are shown in Fig. 6.12. The red circles represent population in $|1\rangle$ and blue circles represent $|0\rangle$. The solid lines are simulations where the Rabi frequency was adjusted to match the experimental results, specifically the red circles

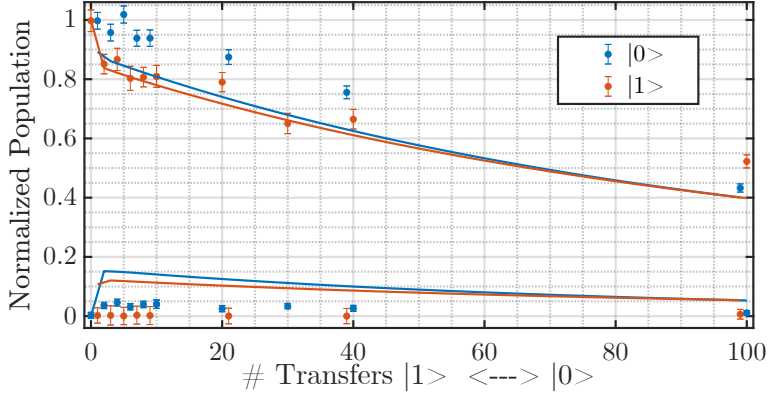


Figure 6.12: Each red and blue dot with error bars represents the experimentally measured population in $|1\rangle$ and $|0\rangle$ respectively. The solid lines are a result of simulation, as described in Sec. 6.3.6. See text for details.

for even # of transfers. The adjusted values are $\Omega_0 = 810$ kHz and $\Omega_1 = 161$ kHz. These values are different in comparison with the calculated values in Sec. 6.3.4. The experimental results and the simulations do not match and there are several reasons for this. Ions in the wings of the Gaussian cross-section experience much lower Rabi frequency than the calculated values and these ions will limit the observed transfer efficiency. The correct way to match the experimental results with the simulations would be to run many simulations with different values of Rabi frequencies and then average the results based on how much of the signal corresponds to a certain value of Rabi frequency.

For the analysis in this work, the efficiency due to the first transfer from $|1\rangle$ to $|0\rangle$ is assumed to be 100%, but this is not reasonable to do. The reason we still chose to do this is that the ratio of the absorption peaks in $|0\rangle$ and $|1\rangle$ after a single transfer is 3.94 ± 0.18 and this is equal to the ratio of their relative oscillator strengths $\frac{0.75}{0.2} = 3.75$ [78]. If the transfer efficiency was not 100%, the ratio of the peaks should be less than the ratio of their relative oscillator strengths. This could explain why the blue circles (experiments) are consistently above the blue solid line (simulation) for the odd number of transfers. Another way to judge the transfer efficiency is to look at the population left behind in $|1\rangle$ after the first transfer. Due to the poor SNR for low absorption, the population left behind in $|1\rangle$ seems to be zero but one cannot be certain of this. This could explain the mismatch between the simulations and experiments for such points.

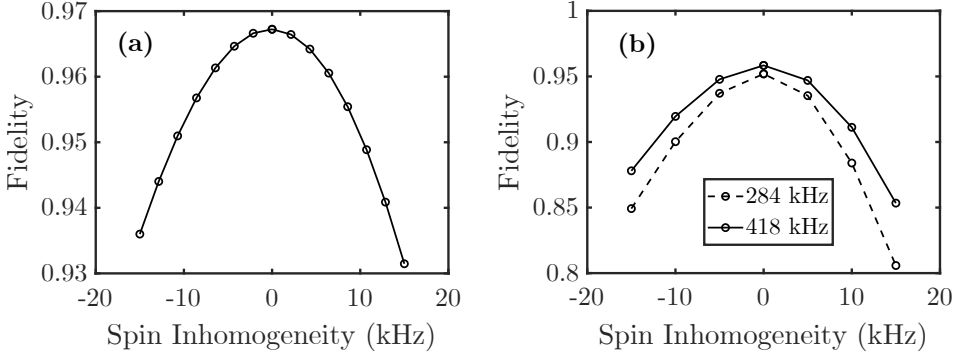


Figure 6.13: Simulations of gate fidelities of a two-color (TC) sequence for arbitrary rotations on the Bloch sphere as a function of spin inhomogeneity (a) Gate fidelity of TC sequence used in Pr:YSO in Ref. [21], as a function of spin inhomogeneity (b) TC with sechscan pulses in Eu:YSO for different values of Rabi frequency amplitude Ω .

6.3.8 Performance of two-color gates

The next step in demonstrating high fidelities is looking at the fidelity of a gate operation or arbitrary rotations on the Bloch sphere using the two-color (TC) pulse scheme described in Sec. 5.1.2. While this scheme compensates for optical inhomogeneity, it is not specifically designed to be robust against spin inhomogeneity. For example, gate fidelity as a function of spin inhomogeneity was simulated and plotted in Fig. 6.13. Part (a) shows the performance in Pr:YSO using the sechyp pulse parameters in [21]. The spin linewidth is 50 kHz [75], and the fidelities achieved in [21] were in the same range as seen here in the simulations. Part (b) in Fig. 6.13 shows the case of TC sequence using sechscan pulses in Eu:YSO, where the spin inhomogeneity is 27 kHz [76]. Fidelity with two different values of Rabi frequencies 284 and 418 kHz on both transitions are plotted. Fidelities obtained can range between 0.8 – 0.95. Two-color pulses were tried in the experiments. A full QST was not performed, but the population transferred was measured to be 0.89 at best. One way to overcome the problems due to spin inhomogeneity is to use materials with lower spin inhomogeneous linewidths. There is evidence that this could depend on the doping concentration [76, 86, 106, 107]. Lower doping concentration will also lead to a lower absorption signal and poorer SNR, so this must be considered.

6.3.9 Summary of challenges and outlook

Sechscan pulses are exceptionally efficient for population inversion, but it is pretty challenging to achieve inversion better than 0.992, given our system's limitations for

ensemble qubits. Several trade-offs in the experimental design have been identified. The main limitation to achieving high transfer efficiencies is the considerable variation of Rabi frequency in the transverse direction. As for the gate operations, a scheme that also optimizes against spin inhomogeneity is needed to achieve high fidelities. Interestingly, it is possible that the spin inhomogeneity can be as low as 7 kHz if the concentration is 0.01% [131], but that would lead to a lower absorption signal and poorer SNR.

In the bigger context of REQC, scalability can only be achieved for single ion qubits, where the robustness of sechyp pulses is not necessarily required. TC gates could be used for gate operations provided the spin transition frequencies of the single ions are known and can be addressed with a resolution better than at least a few kHz. Shorter pulses can potentially be used, as described in detail in other works [15]. As discussed in Sec. 1.2, the case of ensemble qubits could still be useful in stoichiometric crystals [17] and ensemble-based operations in atomic frequency comb (AFC) quantum memories [31–33].

Chapter 7

Conclusions

- **Paper I:** A new method to measure and model flip-flop rates was presented. An average flip-flop rate cannot be used to describe the relaxation dynamics of all the ions in a crystal. There is a distribution of flip-flop rates originating from the fact that every ion in the crystal has a unique environment and is located at different distances and orientations from its neighbor. A potential explanation for the effect of an external magnetic field on the flip-flop rates was given by using a different form of density of states compared to earlier works. A general tool to model interactions at the microscopic level has been developed for future use in the Quantum Information group here in Lund. One can model interactions in other rare-earth-ions using the recipe presented in this paper.
- **Paper II:** The experiments in Paper II are an implementation of a protocol that combines inverse engineering based on Lewis-Reisenfeld invariants and optimization of transfer pulse parameters. Compared with an earlier work [21], the error in fidelity is reduced from $\sim 7\%$ to 2% . However, the pulses in Ref. [21] were designed for arbitrary gate operations. The shortcut pulses used here cannot be used for this purpose since shortcut pulses require the knowledge of the initial and final states before performing a transfer. They can be used, for example, in the state initialization of ancilla qubits in a quantum error correction protocol.

Additionally, the errors in the tomography pulses were identified. These are essentially two-color sechyp pulses, the same kind used in Ref. [21]. Averaging the fidelities of superposition states is not ideal, and this is not how one envisions compensating for errors in a quantum computer. A way to deal with this error more robustly and systematically needs to be developed.

- **Paper III:** Several trade-offs were identified to design an experiment to achieve high-fidelity operations in ensemble qubits. The experiments need some improvements to measure the true fidelity of the sechscan pulses. There should be no delay between the transfer pulses and the reading out of the states. Ideally, a full QST needs to be performed to measure fidelity. The Rabi frequency on each transition needs to be optimized by reading out the population in each state immediately after the transfer pulse without any delay. It would also help if ways to minimize losses in laser power were implemented.

While the two-color scheme [21] is not exclusively designed to be robust against spin inhomogeneity, it inherently reduces some error due to spin inhomogeneity, as identified in Ref. [132]. Still, the errors are not entirely minimized, and spin inhomogeneity was identified as the bottleneck to achieving high fidelity in operations on ensemble qubits. A new method that is simultaneously robust against spin inhomogeneity and all other inhomogeneities needs to be developed. The technique in Paper II could potentially be used, but this would restrict the case to operations between known states. It is possible that the spin inhomogeneity can be as low as 7 kHz if the concentration is 0.01% [131], but that would lead to a lower absorption signal and poorer SNR.

7.1 Personal perspective

When I started my thesis, I knew I would be working on projects related to Quantum Information in rare-earth-ions, but the project details were not very well defined, and I was lucky to have the freedom to explore. There were several times during my Ph.D. when I felt like the work I was involved in was very exciting - when I saw liquid helium boil, when I got my first frostbite from liquid nitrogen, when I tuned the laser to change color from green to yellow to red, when I first detected a photon echo, when I burnt an 11 kHz narrow hole in Eu:YSO, when the hyperfine relaxation project finally came together... Some of these thrilling times would get normalized over time, especially when I was battling equipment, fixing things, and playing detective to find out what was going wrong during the experiments. But, the excitement would revive when I discussed and shared knowledge and learned new things. I learned more when teaching the Quantum control/Quantum Information lab than when I sat in my office reading about it. For all of these times, I am grateful. But, some things were not fruitful, and several took longer than planned. Below, I share some thoughts on the progress and timeline of each paper.

The measurements on hyperfine relaxation (Paper I) started in November 2017 as one of those things one can quickly do but developed in ways I had not planned. We were

expecting a double-exponential decay and were baffled that the decay curves did not follow this expectation. We tried hard for some time and thought there was something wrong with the measurements. After ruling out such possibilities, we concluded that it could be related to the fact that the relaxation cannot be described by one or two rates for all the ions in the crystal since it depends on the position/orientation of each ion with respect to its neighbors. There were two routes to take; one was to model this effect exactly using dipole-dipole interactions. And the other was to use a distribution of neighbor-neighbor distances with some fitting parameters to match the experimental data. We tried the first route for a long time. This required understanding spin hamiltonians and dipole-dipole interactions. These concepts were partly new to the group, and I am glad the project developed in this direction since it was what I enjoyed the most. But this approach did not entirely work. In the end, we combined the two approaches. It wasn't until we discussed the nuances of Fermi's Golden Rule with a theoretical physicist, Prof. Peter Samuelsson, that things started to fall into place. There were quite a few stumbles along the way, but we used a form of density of states that had not been used previously. We gained several insights about nonexponential decay, and I was happy with the results. I started working on this project a few months before the start of my Ph.D., and it wasn't until the last year of my Ph.D. that we submitted the manuscript.

The project on shortcut pulses (Paper II) was a collaboration with Dr. Ying Yan, who did her Ph.D. in our lab several years ago and has now moved to China. A first attempt at the experiments had been made during the summer of 2017 and the knowledge gained was used in the next try in the summer of 2018, which was when I joined the experiments. There were several unexpected hurdles that delayed the progress. We had weird frequency components on the pulses, and the cryostat decided to give up on us, so it had to be heated up and cooled again (twice). The laser is always a bit upset in the summers because we sometimes do not get cold enough water to the labs, and the stabilization does not work super well. The dye had to be changed in the middle of the experimental run, and Yan had to return to China before the experiments were finished. For several months after the experiments, we scratched our heads about the tomography data and found state-dependent errors for the two-color pulses. Long-distance communication and collaboration were also challenging, but chatting with Yan was always a delight. It wasn't until the winter of 2020 that this manuscript was submitted.

The high-fidelity project (Paper III) left me with *high*-disappointments. It had always been said that Eu was the star ion with its long coherence times, but there was also a flip side. The crystal we had ordered was stuck in China when Covid hit. We started to do experiments with another sample from Paris. To begin with, none of the pulses I had optimized worked. The Rabi frequency was lower than expected, and a new pulse

had to be designed. The crystal from China finally arrived, but it had lower absorption than expected, so we continued to use the backup crystal from Paris. Running the experiments alone in the lab was also quite challenging and demanding. There are always continuous discussions with other group members, but having a partner while doing the experiments can make a big difference, especially when there is limited lab time. We were fooled by the experimental results and lulled into thinking we had excellent results. Some discussions later, we realized we should have done the experiments without any delays between the transfers. It was a pity that the gate operations did not work well but we identified the cause to be spin inhomogeneity. Maybe the next student who comes in can find new solutions.

References

- [1] R. P. Feynman, “Simulating physics with computers,” *International Journal of Theoretical Physics*, vol. 21, no. 6-7, pp. 467–488, 1982.
- [2] F. Arute and et al, “Quantum supremacy using a programmable superconducting processor,” *Nature*, vol. 574, pp. 505–510, Oct. 2019.
- [3] “IBM Quantum Computing.” <https://www.ibm.com/quantum>. Accessed: 2022-11-09.
- [4] “Rigetti Computing.” <https://www.rigetti.com/research>. Accessed: 2022-11-09.
- [5] L. Egan, D. M. Debroy, C. Noel, A. Risinger, D. Zhu, D. Biswas, M. Newman, M. Li, K. R. Brown, M. Cetina, and C. Monroe, “Fault-tolerant control of an error-corrected qubit,” *Nature*, vol. 598, pp. 281–286, Oct. 2021.
- [6] I. Pogorelov, T. Feldker, C. D. Marciniak, L. Postler, G. Jacob, O. Kriegelsteiner, V. Podlesnic, M. Meth, V. Negnevitsky, M. Stadler, B. Höfer, C. Wächter, K. Lakhmanskiy, R. Blatt, P. Schindler, and T. Monz, “Compact ion-trap quantum computing demonstrator,” *PRX Quantum*, vol. 2, p. 020343, Jun 2021.
- [7] P. Niroula, R. Shaydulin, R. Yalovetzky, P. Minssen, D. Herman, S. Hu, and M. Pistoia, “Constrained quantum optimization for extractive summarization on a trapped-ion quantum computer,” *Sci Rep*, vol. 12, p. 17171, Oct. 2022.
- [8] S. Bartolucci, P. M. Birchall, M. Gimeno-Segovia, E. Johnston, K. Kieling, M. Pant, T. Rudolph, J. Smith, C. Sparrow, and M. D. Vidrighin, “Creation of Entangled Photonic States Using Linear Optics,” June 2021. arXiv:2106.13825 [quant-ph].
- [9] L. S. Madsen, F. Laudenbach, M. F. Askarani, F. Rortais, T. Vincent, J. F. F. Bulmer, F. M. Miatto, L. Neuhaus, L. G. Helt, M. J. Collins, A. E. Lita, T. Gerrits, S. W. Nam, V. D. Vaidya, M. Menotti, I. Dhand, Z. Vernon, N. Quesada,

- and J. Lavoie, “Quantum computational advantage with a programmable photonic processor,” *Nature*, vol. 606, pp. 75–81, June 2022.
- [10] M. H. Abobeih, Y. Wang, J. Randall, S. J. H. Loenen, C. E. Bradley, M. Markham, D. J. Twitchen, B. M. Terhal, and T. H. Taminiau, “Fault-tolerant operation of a logical qubit in a diamond quantum processor,” *Nature*, vol. 606, pp. 884–889, June 2022.
- [11] “Google Quantum AI.” <https://quantumai.google/>. Accessed: 2022-11-09.
- [12] “IonQ Trapped Ion Computing.” <https://ionq.com/>. Accessed: 2022-11-09.
- [13] A. Kinos, D. Hunger, R. Kolesov, K. Mølmer, H. de Riedmatten, P. Goldner, A. Tallaire, L. Morvan, P. Berger, S. Welinski, K. Karrai, L. Rippe, S. Kröll, and A. Walther, “Roadmap for rare-earth quantum computing,” *arXiv*, March 2021.
- [14] D. P. DiVincenzo, “The Physical Implementation of Quantum Computation,” *Fortschr. Phys.*, vol. 48, pp. 771–783, Sept. 2000. arXiv:quant-ph/0002077.
- [15] A. Kinos, L. Rippe, S. Kröll, and A. Walther, “Designing gate operations for single-ion quantum computing in rare-earth-ion-doped crystals,” *Phys. Rev. A*, vol. 104, p. 052624, Nov 2021.
- [16] A. Kinos, L. Rippe, A. Walther, and S. Kröll, “Microscopic treatment of instantaneous spectral diffusion and its effect on quantum gate fidelities in rare-earth-ion-doped crystals,” *Phys. Rev. A*, vol. 105, p. 032608, Mar 2022.
- [17] R. L. Ahlefeldt, M. J. Pearce, M. R. Hush, and M. J. Sellars, “Quantum processing with ensembles of rare-earth ions in a stoichiometric crystal,” *Phys. Rev. A*, vol. 101, p. 012309, Jan 2020.
- [18] M. Nilsson, L. Rippe, S. Kröll, R. Klieber, and D. Suter, “Hole-burning techniques for isolation and study of individual hyperfine transitions in inhomogeneously broadened solids demonstrated in $\text{Pr}^{3+}:\text{Y}_2\text{SiO}_5$,” *Phys. Rev. B*, vol. 70, p. 214116, Dec 2004.
- [19] R. Oswald, M. G. Hansen, E. Wiens, A. Y. Nevsky, and S. Schiller, “Characteristics of long-lived persistent spectral holes in $\text{Eu}^{3+}:\text{Y}_2\text{SiO}_5$ at 1.2 K,” *Phys. Rev. A*, vol. 98, p. 062516, Dec 2018.
- [20] M. Zhong, M. P. Hedges, R. L. Ahlefeldt, J. G. Bartholomew, S. E. Beavan, S. M. Wittig, J. J. Longdell, and M. J. Sellars, “Optically addressable nuclear

- spins in a solid with a six-hour coherence time,” *Nature*, vol. 517, pp. 177–180, Jan. 2015.
- [21] L. Rippe, B. Julsgaard, A. Walther, Y. Ying, and S. Kröll, “Experimental quantum-state tomography of a solid-state qubit,” *Phys. Rev. A*, vol. 77, p. 022307, Feb 2008.
 - [22] N. Ohlsson, R. Krishna Mohan, and S. Kröll, “Quantum computer hardware based on rare-earth-ion-doped inorganic crystals,” *Opt. Commun.*, vol. 201, no. 1, pp. 71–77, 2002.
 - [23] J. H. Wesenberg, K. Mølmer, L. Rippe, and S. Kröll, “Scalable designs for quantum computing with rare-earth-ion-doped crystals,” *Phys. Rev. A*, vol. 75, p. 012304, Jan 2007.
 - [24] A. Kinos, L. Rippe, D. Serrano, A. Walther, and S. Kröll, “High-connectivity quantum processor nodes using single-ion qubits in rare-earth-ion-doped crystals,” *Phys. Rev. A*, vol. 105, p. 032603, Mar 2022.
 - [25] B. Casabone, C. Deshmukh, S. Liu, D. Serrano, A. Ferrier, T. Hümmer, P. Goldner, D. Hunger, and H. de Riedmatten, “Dynamic control of Purcell enhanced emission of erbium ions in nanoparticles,” *Nat Commun*, vol. 12, p. 3570, June 2021.
 - [26] K. Xia, F. Sardi, C. Sauerzapf, T. Kornher, H.-W. Becker, Z. Kis, L. Kovacs, D. Dertli, J. Foglszinger, R. Kolesov, and J. Wrachtrup, “Tunable microcavities coupled to rare-earth quantum emitters,” *Optica*, vol. 9, pp. 445–450, Apr 2022.
 - [27] T. Zhong, J. M. Kindem, J. G. Bartholomew, J. Rochman, I. Craiciu, V. Verma, S. W. Nam, F. Marsili, M. D. Shaw, A. D. Beyer, and A. Faraon, “Optically addressing single rare-earth ions in a nanophotonic cavity,” *Phys. Rev. Lett.*, vol. 121, p. 183603, Oct 2018.
 - [28] M. Raha, S. Chen, C. M. Phenicie, S. Ourari, A. M. Dibos, and J. D. Thompson, “Optical quantum nondemolition measurement of a single rare earth ion qubit,” *Nat Commun*, vol. 11, p. 1605, Mar. 2020. Number: 1 Publisher: Nature Publishing Group.
 - [29] R. L. Ahlefeldt, W. D. Hutchison, N. B. Manson, and M. J. Sellars, “Method for assigning satellite lines to crystallographic sites in rare-earth crystals,” *Phys. Rev. B*, vol. 88, p. 184424, Nov 2013.
 - [30] M. Yamaguchi, K. Koyama, T. Suemoto, and M. Mitsunaga, “Perturbed ion sites in $\text{Eu}^{3+}:\text{YAlO}_3$ studied by optical-rf double-resonance spectroscopy,” *Phys. Rev. B*, vol. 59, pp. 9126–9131, Apr 1999.

- [31] M. Gündoğan, P. M. Ledingham, K. Kutluer, M. Mazzera, and H. de Riedmatten, “Solid state spin-wave quantum memory for time-bin qubits,” *Phys. Rev. Lett.*, vol. 114, p. 230501, Jun 2015.
- [32] N. Timoney, I. Usmani, P. Jobez, M. Afzelius, and N. Gisin, “Single-photon-level optical storage in a solid-state spin-wave memory,” *Phys. Rev. A*, vol. 88, p. 022324, Aug 2013.
- [33] M. Alqedra, *Towards Single-Ion Detection and Single-Photon Storage in Rare-Earth-Ion-Doped Crystals*. PhD thesis, Lund University, 2022.
- [34] M. Nilsson and S. Kröll, “Solid state quantum memory using complete absorption and re-emission of photons by tailored and externally controlled inhomogeneous absorption profiles,” *Opt. Commun.*, vol. 247, no. 4, pp. 393–403, 2005.
- [35] M. Nicolle, J. N. Becker, C. Weinzetl, I. A. Walmsley, and P. M. Ledingham, “Gigahertz-Bandwidth Optical Memory in $\text{Pr}^{3+}:\text{Y}_2\text{SiO}_5$,” *Opt. Lett.*, vol. 46, p. 2948, June 2021.
- [36] M. Afzelius and C. Simon, “Impedance-matched cavity quantum memory,” *Phys. Rev. A*, vol. 82, p. 022310, Aug. 2010.
- [37] R. L. Ahlefeldt, M. J. Pearce, M. R. Hush, and M. J. Sellars, “Quantum processing with ensembles of rare-earth ions in a stoichiometric crystal,” *Phys. Rev. A*, vol. 101, p. 012309, Jan 2020.
- [38] M. Grimm, A. Beckert, G. Aeppli, and M. Müller, “Universal quantum computing using electronuclear wavefunctions of rare-earth ions,” *PRX Quantum*, vol. 2, p. 010312, Jan 2021.
- [39] C. Simon, H. de Riedmatten, M. Afzelius, N. Sangouard, H. Zbinden, and N. Gisin, “Quantum repeaters with photon pair sources and multimode memories,” *Phys. Rev. Lett.*, vol. 98, p. 190503, May 2007.
- [40] H. de Riedmatten, M. Afzelius, M. U. Staudt, C. Simon, and N. Gisin, “A solid-state light–matter interface at the single-photon level,” *Nature*, vol. 456, pp. 773–777, Dec. 2008.
- [41] M. Gündoğan, P. M. Ledingham, K. Kutluer, M. Mazzera, and H. de Riedmatten, “Solid state spin-wave quantum memory for time-bin qubits,” *Phys. Rev. Lett.*, vol. 114, p. 230501, Jun 2015.
- [42] F. Bussi eres, C. Clausen, A. Tiranov, B. Korzh, V. B. Verma, S. W. Nam, F. Marsili, A. Ferrier, P. Goldner, H. Herrmann, C. Silberhorn, W. Sohler,

- M. Afzelius, and N. Gisin, “Quantum teleportation from a telecom-wavelength photon to a solid-state quantum memory,” *Nat. Photon*, vol. 8, pp. 775–778, Oct. 2014.
- [43] B. Kraus, W. Tittel, N. Gisin, M. Nilsson, S. Kröll, and J. I. Cirac, “Quantum memory for nonstationary light fields based on controlled reversible inhomogeneous broadening,” *Phys. Rev. A*, vol. 73, p. 020302, Feb 2006.
- [44] Y. Li, H. Zhang, C. Kim, K. H. Wagner, P. Hemmer, and L. V. Wang, “Pulsed ultrasound-modulated optical tomography using spectral-hole burning as a narrowband spectral filter,” *Appl. Phys. Lett.*, vol. 93, p. 011111, July 2008.
- [45] H. Zhang, M. Sabooni, L. Rippe, C. Kim, S. Kröll, L. V. Wang, and P. R. Hemmer, “Slow light for deep tissue imaging with ultrasound modulation,” *Appl. Phys. Lett.*, vol. 100, p. 131102, Mar. 2012.
- [46] Xiao Xu, Sri-Rajasekhar Kothapalli, Honglin Liu, and Lihong V. Wang, “Spectral hole burning for ultrasound-modulated optical tomography of thick tissue,” *J. Biomed. Opt.*, vol. 15, pp. 1–5, Nov. 2010.
- [47] C. Venet, M. Bocoum, J.-B. Laudereau, T. Chaneliere, F. Ramaz, and A. Louchet-Chauvet, “Ultrasound-modulated optical tomography in scattering media: flux filtering based on persistent spectral hole burning in the optical diagnosis window,” *Opt. Lett.*, vol. 43, p. 3993, Aug. 2018.
- [48] D. Hill, A. Bengtsson, T. Erlöv, M. Cinthio, and S. Kröll, “Acousto-optic interaction strengths in optically scattering media using high pressure acoustic pulses,” *Biomed. Opt. Express*, vol. 12, p. 3196, June 2021.
- [49] Q. Zhan, J. Qian, H. Liang, G. Somesfalean, D. Wang, S. He, Z. Zhang, and S. Andersson-Engels, “Using 915 nm Laser Excited $\text{Tm}^{3+}/\text{Er}^{3+}/\text{Ho}^{3+}$ -Doped NaYbF_4 Upconversion Nanoparticles for *in Vitro* and Deeper *in Vivo* Bioimaging without Overheating Irradiation,” *ACS Nano*, vol. 5, pp. 3744–3757, May 2011.
- [50] P. B. Sellin, N. M. Strickland, J. L. Carlsten, and R. L. Cone, “Programmable frequency reference for subkilohertz laser stabilization by use of persistent spectral hole burning,” *Opt. Lett.*, vol. 24, p. 1038, Aug. 1999.
- [51] T. Böttger, G. J. Pryde, and R. L. Cone, “Programmable laser frequency stabilization at 1523 nm by use of persistent spectral hole burning,” *Opt. Lett.*, vol. 28, p. 200, Feb. 2003.

- [52] M. J. Thorpe, L. Rippe, T. M. Fortier, M. S. Kirchner, and T. Rosenband, “Frequency stabilization to 6×10^{-16} via spectral-hole burning,” *Nat. Photonics*, vol. 5, pp. 688–693, Nov. 2011.
- [53] S. P. Horvath, C. Shi, D. Gustavsson, A. Walther, A. Kinos, S. Kröll, and L. Rippe, “Slow light frequency reference cavities - proof of concept for reducing the frequency sensitivity due to length fluctuations,” *New J. Phys.*, Feb. 2022.
- [54] O. Gobron, K. Jung, N. Galland, K. Predehl, R. Le Targat, A. Ferrier, P. Goldner, S. Seidelin, and Y. Le Coq, “Dispersive heterodyne probing method for laser frequency stabilization based on spectral hole burning in rare-earth doped crystals,” *Opt. Express*, vol. 25, p. 15539, June 2017.
- [55] G. J. Pryde, M. J. Sellars, and N. B. Manson, “Solid state coherent transient measurements using hard optical pulses,” *Phys. Rev. Lett.*, vol. 84, pp. 1152–1155, Feb 2000.
- [56] L. Rippe, M. Nilsson, S. Kröll, R. Klieber, and D. Suter, “Experimental demonstration of efficient and selective population transfer and qubit distillation in a rare-earth-metal-ion-doped crystal,” *Phys. Rev. A*, vol. 71, p. 062328, June 2005.
- [57] L. Rippe, *Quantum computing with naturally trapped sub-nanometre-spaced ions*. PhD thesis, Lund University, 2006.
- [58] A. Walther, B. Julsgaard, L. Rippe, Y. Ying, S. Kröll, R. Fisher, and S. Glaser, “Extracting high fidelity quantum computer hardware from random systems,” *Phys. Scr.*, vol. T137, p. 014009, Dec. 2009.
- [59] A. Walther, A. N. Nilsson, Q. Li, L. Rippe, and S. Kröll, “Fast all-optical nuclear spin echo technique based on EIT,” *Eur. Phys. J. D*, vol. 70, p. 166, Aug. 2016.
- [60] A. Alexander, J. Longdell, M. Sellars, and N. Manson, “Coherent information storage with photon echoes produced by switching electric fields,” *Journal of Luminescence*, vol. 127, no. 1, pp. 94–97, 2007. Proceedings of the Ninth International Meeting on Hole Burning, Single Molecule, and Related Spectroscopies: Science and Applications.
- [61] J. J. Longdell and M. J. Sellars, “Experimental demonstration of quantum-state tomography and qubit-qubit interactions for rare-earth-metal-ion-based solid-state qubits,” *Phys. Rev. A*, vol. 69, p. 032307, Mar 2004.

- [62] J. J. Longdell, M. J. Sellars, and N. B. Manson, "Demonstration of conditional quantum phase shift between ions in a solid," *Phys. Rev. Lett.*, vol. 93, p. 130503, Sep 2004.
- [63] A. Kinos, *Light-Matter Interaction and Quantum Computing in Rare-Earth-Ion-Doped Crystals*. PhD thesis, Lund University, 2018.
- [64] W. T. Carnall, G. L. Goodman, K. Rajnak, and R. S. Rana, "A systematic analysis of the spectra of the lanthanides doped into single crystal LaF₃," *The Journal of Chemical Physics*, vol. 90, pp. 3443–3457, Apr. 1989.
- [65] G. H. Dieke and H. M. Crosswhite, "The Spectra of the Doubly and Triply Ionized Rare Earths," *Appl. Opt.*, vol. 2, p. 675, July 1963.
- [66] G. Liu and B. Jacquier, eds., *Spectroscopic properties of rare earths in optical materials*. No. 83 in Springer series in materials science, Berlin ; New York: Springer, 2005.
- [67] C. Thiel, T. Böttger, and R. Cone, "Rare-earth-doped materials for applications in quantum information storage and signal processing," *Journal of Luminescence*, vol. 131, no. 3, pp. 353–361, 2011. Selected papers from DPC'10.
- [68] F. Könz, Y. Sun, C. W. Thiel, R. L. Cone, R. W. Equall, R. L. Hutcheson, and R. M. Macfarlane, "Temperature and concentration dependence of optical dephasing, spectral-hole lifetime, and anisotropic absorption in Eu³⁺:Y₂SiO₅," *Phys. Rev. B*, vol. 68, p. 085109, Aug 2003.
- [69] R. W. Equall, R. L. Cone, and R. M. Macfarlane, "Homogeneous broadening and hyperfine structure of optical transitions in Pr³⁺:Y₂SiO₅," *Phys. Rev. B*, vol. 52, pp. 3963–3969, Aug 1995.
- [70] C. W. Thiel, R. M. Macfarlane, Y. Sun, T. Böttger, N. Sinclair, W. Tittel, and R. L. Cone, "Measuring and analyzing excitation-induced decoherence in rare-earth-doped optical materials," *Laser Phys.*, vol. 24, p. 106002, Oct. 2014.
- [71] E. Fraval, M. J. Sellars, and J. J. Longdell, "Method of extending hyperfine coherence times in Pr³⁺:Y₂SiO₅," *Phys. Rev. Lett.*, vol. 92, p. 077601, Feb 2004.
- [72] R. W. Equall, Y. Sun, R. L. Cone, and R. M. Macfarlane, "Ultralow optical dephasing in Eu³⁺:Y₂SiO₅," *Phys. Rev. Lett.*, vol. 72, pp. 2179–2182, Apr 1994.
- [73] E. Fraval, M. Sellars, A. Morrison, and A. Ferris, "Pr–Y interaction in Pr³⁺:Y₂SiO₅," *J. Lumin.*, vol. 107, no. 1, pp. 347–350, 2004. Proceedings of the 8th International Meeting on Hole Burning, Single Molecule, and Related Spectroscopies: Science and Applications.

- [74] F. R. Graf, A. Renn, G. Zumofen, and U. P. Wild, “Photon-echo attenuation by dynamical processes in rare-earth-ion-doped crystals,” *Phys. Rev. B*, vol. 58, pp. 5462–5478, Sep 1998.
- [75] M. Lovrić, P. Glasenapp, and D. Suter, “Spin Hamiltonian characterization and refinement for $\text{Pr}^{3+}:\text{YAlO}_3$ and $\text{Pr}^{3+}:\text{Y}_2\text{SiO}_5$,” *Phys. Rev. B*, vol. 85, p. 014429, Jan. 2012.
- [76] P. Jobez, C. Laplane, N. Timoney, N. Gisin, A. Ferrier, P. Goldner, and M. Afzelius, “Coherent spin control at the quantum level in an ensemble-based optical memory,” *Phys. Rev. Lett.*, vol. 114, p. 230502, Jun 2015.
- [77] P. Villars and K. Cenzual, “ Y_2SiO_5 ($\text{Y}_2[\text{SiO}_4]\text{O}$ ht) Crystal Structure: Datasheet from ‘Pauling File Multinaries in SpringerMaterials,’ 2012.
- [78] E. Z. Cruzeiro, J. Etesse, A. Tiranov, P.-A. Bourdel, F. Fröwis, P. Goldner, N. Gisin, and M. Afzelius, “Characterization of the hyperfine interaction of the excited $^5\text{D}_0$ state of $\text{Eu}^{3+}:\text{Y}_2\text{SiO}_5$,” *Phys. Rev. B*, vol. 97, p. 094416, Mar. 2018.
- [79] C. Slitchter, *Principles of Magnetic Resonance*. Springer, Berlin, Heidelberg, 1990.
- [80] A. Abragam and B. Bleaney, *Electron paramagnetic resonance of transition ions*. Oxford: Oxford University Press, 2012.
- [81] N. Bloembergen, E. M. Purcell, and R. V. Pound, “Relaxation effects in nuclear magnetic resonance absorption,” *Phys. Rev.*, vol. 73, pp. 679–712, Apr 1948.
- [82] M. Teplov, “Magnetic resonance on Pr^{141} nuclei in a $\text{Pr}_2(\text{SO}_4)_3 \cdot 8\text{H}_2\text{O}$ single crystal,” *Soviet Physics JETP*, vol. 26, 1968.
- [83] J. G. Bartholomew, R. L. Ahlefeldt, and M. J. Sellars, “Engineering closed optical transitions in rare-earth ion crystals,” *Phys. Rev. B*, vol. 93, p. 014401, Jan. 2016.
- [84] N. Bloembergen, “On the interaction of nuclear spins in a crystalline lattice,” *Physica*, vol. 15, pp. 386–426, May 1949.
- [85] W. H. Chambers, R. E. Sheriff, and D. Williams, “The Nuclear Magnetic Moment of Praseodymium 141,” *Phys. Rev.*, vol. 78, pp. 482–483, May 1950.
- [86] A. Arcangeli, M. Lovrić, B. Tumino, A. Ferrier, and P. Goldner, “Spectroscopy and coherence lifetime extension of hyperfine transitions in $^{151}\text{Eu}^{3+}:\text{Y}_2\text{SiO}_5$,” *Phys. Rev. B*, vol. 89, p. 184305, May 2014.

- [87] R. L. Ahlefeldt, W. D. Hutchison, and M. J. Sellars, “Eu³⁺ superhyperfine structure due to magnetic dipole–dipole interactions with Nd³⁺ in Nd³⁺:EuCl₃·6H₂O,” *Journal of Luminescence*, vol. 130, no. 9, pp. 1594–1597, 2010.
- [88] B. Car, L. Veissier, A. Louchet-Chauvet, J.-L. Le Gouët, and T. Chanelière, “Selective optical addressing of nuclear spins through superhyperfine interaction in rare-earth doped solids,” *Phys. Rev. Lett.*, vol. 120, p. 197401, May 2018.
- [89] R. Orbach and B. Bleaney, “Spin-lattice relaxation in rare-earth salts,” *Proceedings of the Royal Society of London. Series A. Mathematical and Physical Sciences*, vol. 264, pp. 458–484, Dec. 1961.
- [90] G. H. Larson and C. D. Jeffries, “Spin-Lattice Relaxation in Some Rare-Earth Salts. I. Temperature Dependence,” *Phys. Rev.*, vol. 141, pp. 461–478, Jan. 1966.
- [91] G. H. Larson and C. D. Jeffries, “Spin-Lattice Relaxation in Some Rare-Earth Salts. II. Angular Dependence, Hyperfine Effects, and Cross Relaxation,” *Phys. Rev.*, vol. 145, pp. 311–324, May 1966.
- [92] R. M. Shelby, R. M. Macfarlane, and C. S. Yannoni, “Optical measurement of spin-lattice relaxation of dilute nuclei LaF₃:Pr³⁺,” *Phys. Rev. B*, vol. 21, pp. 5004–5011, June 1980.
- [93] T. L. Bohan and H. J. Stapleton, “Temperature and Magnetic Field Dependence of the Spin-Lattice Relaxation Rates for Er³⁺, Pr³⁺ and, Tb³⁺ in Anhydrous LaCl₃,” *Phys. Rev.*, vol. 182, pp. 385–394, June 1969.
- [94] T. Blasberg and D. Suter, “Nuclear spin relaxation of Pr³⁺ in YAlO₃. A temperature-dependent optical-rf double-resonance study,” *Chem. Phys. Lett.*, vol. 2, no. 6, p. 6, 1993.
- [95] K. Holliday, M. Croci, E. Vauthey, and U. P. Wild, “Spectral hole burning and holography in an Y₂SiO₅:Pr³⁺ crystal,” *Phys. Rev. B*, vol. 47, pp. 14741–14752, June 1993.
- [96] N. Bloembergen, S. Shapiro, P. S. Pershan, and J. O. Artman, “Cross-relaxation in spin systems,” *Phys. Rev.*, vol. 114, pp. 445–459, Apr 1959.
- [97] E. Z. Cruzeiro, A. Tiranov, I. Usmani, C. Laplane, J. Lavoie, A. Ferrier, P. Goldner, N. Gisin, and M. Afzelius, “Spectral hole lifetimes and spin population relaxation dynamics in neodymium-doped yttrium orthosilicate,” *Phys. Rev. B*, vol. 95, p. 205119, May 2017.

- [98] B. Car, L. Veissier, A. Louchet-Chauvet, J.-L. Le Gouët, and T. Chanelière, “Optical study of the anisotropic erbium spin flip-flop dynamics,” *Phys. Rev. B*, vol. 100, p. 165107, Oct. 2019.
- [99] E. S. Petersen, A. M. Tyryshkin, J. J. L. Morton, E. Abe, S. Tojo, K. M. Itoh, M. L. W. Thewalt, and S. A. Lyon, “Nuclear spin decoherence of neutral ^{31}P donors in silicon: Effect of environmental ^{29}Si nuclei,” *Phys. Rev. B*, vol. 93, p. 161202, Apr 2016.
- [100] F. S. Dzheparov, J. F. Jacquinot, and S. V. Stepanov, “Nuclear relaxation via paramagnetic impurities,” *Phys. Atom. Nuclei*, vol. 65, pp. 2052–2063, Nov. 2002.
- [101] Y. J. Uemura, T. Yamazaki, D. R. Harshman, M. Senba, and E. J. Ansaldo, “Muon-spin relaxation in aFe and CuMn spin glasses,” *Phys. Rev. B*, vol. 31, pp. 546–563, Jan 1985.
- [102] R. C. Johnson, B. Z. Malkin, J. S. Lord, S. R. Giblin, A. Amato, C. Baines, A. Lascialfari, B. Barbara, and M. J. Graf, “Evolution of spin relaxation processes in $\text{LiY}_{1-x}\text{Ho}_x\text{F}_4$ studied via ac-susceptibility and muon spin relaxation,” *Phys. Rev. B*, vol. 86, p. 014427, July 2012.
- [103] L. Gomes, L. C. Courrol, L. V. G. Tarelho, and I. M. Ranieri, “Cross-relaxation process between $+3$ rare-earth ions in LiYF_4 crystals,” *Phys. Rev. B*, vol. 54, pp. 3825–3829, Aug. 1996.
- [104] R. Klieber, A. Michalowski, R. Neuhaus, and D. Suter, “All-optical measurement of nuclear-spin relaxation,” *Phys. Rev. B*, vol. 68, p. 054426, Aug. 2003.
- [105] E. Saglamyurek, T. Lutz, L. Veissier, M. P. Hedges, C. W. Thiel, R. L. Cone, and W. Tittel, “Efficient and long-lived zeeman-sublevel atomic population storage in an erbium-doped glass fiber,” *Phys. Rev. B*, vol. 92, p. 241111, Dec 2015.
- [106] N. Timoney, I. Usmani, P. Jobez, M. Afzelius, and N. Gisin, “Single-photon-level optical storage in a solid-state spin-wave memory,” *Phys. Rev. A*, vol. 88, p. 022324, Aug 2013.
- [107] H. Q. Fan, K. H. Kagalwala, S. V. Polyakov, A. L. Migdall, and E. A. Goldschmidt, “Electromagnetically induced transparency in inhomogeneously broadened solid media,” *Phys. Rev. A*, vol. 99, p. 053821, May 2019.
- [108] M. S. Silver, R. I. Joseph, and D. I. Hoult, “Selective spin inversion in nuclear magnetic resonance and coherent optics through an exact solution of the Bloch-Riccati equation,” *Phys. Rev. A*, vol. 31, pp. 2753–2755, Apr 1985.

- [109] I. Roos and K. Mølmer, “Quantum computing with an inhomogeneously broadened ensemble of ions: Suppression of errors from detuning variations by specially adapted pulses and coherent population trapping,” *Phys. Rev. A*, vol. 69, p. 022321, Feb 2004.
- [110] M. Tian, T. Chang, K. D. Merkel, and W. Randall, “Reconfiguration of spectral absorption features using a frequency-chirped laser pulse,” *Appl. Opt.*, vol. 50, pp. 6548–6554, Dec 2011.
- [111] A. Walther, *Coherent processes in rare-earth-ion-doped solids*. PhD thesis, Lund University, 2008.
- [112] T. Chang, M. Tian, R. K. Mohan, C. Renner, K. D. Merkel, and W. R. Babbitt, “Recovery of spectral features readout with frequency-chirped laser fields,” *Opt. Lett.*, vol. 30, p. 1129, May 2005.
- [113] F. Wolf, “Fast sweep experiments in microwave spectroscopy,” *J. Phys. D: Appl. Phys.*, vol. 27, pp. 1774–1780, Aug. 1994.
- [114] P. C. Hobbs, *Optical Detection*. John Wiley & Sons, Ltd, 2009.
- [115] L. J. Oberto, Z. W. Barber, and W. R. Babbitt, “Nonlinear recovery of narrow spectral features with fast chirped readout,” *J. Opt. Soc. Am. B*, vol. 35, p. 2963, Dec. 2018.
- [116] K. Bergmann, H. Theuer, and B. W. Shore, “Coherent population transfer among quantum states of atoms and molecules,” *Rev. Mod. Phys.*, vol. 70, pp. 1003–1025, Jul 1998.
- [117] P. Král, I. Thanopoulos, and M. Shapiro, “Colloquium: Coherently controlled adiabatic passage,” *Rev. Mod. Phys.*, vol. 79, pp. 53–77, Jan 2007.
- [118] J. Wesenberg and K. Mølmer, “Robust quantum gates and a bus architecture for quantum computing with rare-earth-ion-doped crystals,” *Phys. Rev. A*, vol. 68, p. 012320, Jul 2003.
- [119] B. T. Torosov, S. Guérin, and N. V. Vitanov, “High-fidelity adiabatic passage by composite sequences of chirped pulses,” *Phys. Rev. Lett.*, vol. 106, p. 233001, Jun 2011.
- [120] T. Nöbauer, A. Angerer, B. Bartels, M. Trupke, S. Rotter, J. Schmiedmayer, F. Mintert, and J. Majer, “Smooth optimal quantum control for robust solid-state spin magnetometry,” *Phys. Rev. Lett.*, vol. 115, p. 190801, Nov 2015.

- [I21] X. Chen, I. Lizuain, A. Ruschhaupt, D. Guéry-Odelin, and J. G. Muga, “Shortcut to adiabatic passage in two- and three-level atoms,” *Phys. Rev. Lett.*, vol. 105, p. 123003, Sep 2010.
- [I22] X. Chen, A. Ruschhaupt, S. Schmidt, A. del Campo, D. Guéry-Odelin, and J. G. Muga, “Fast optimal frictionless atom cooling in harmonic traps: Shortcut to adiabaticity,” *Phys. Rev. Lett.*, vol. 104, p. 063002, Feb 2010.
- [I23] X. Chen, E. Torrontegui, and J. G. Muga, “Lewis-riesenfeld invariants and transitionless quantum driving,” *Phys. Rev. A*, vol. 83, p. 062116, Jun 2011.
- [I24] X. Chen and J. G. Muga, “Engineering of fast population transfer in three-level systems,” *Phys. Rev. A*, vol. 86, p. 033405, Sep 2012.
- [I25] S. Masuda and K. Nakamura, “Fast-forward of adiabatic dynamics in quantum mechanics,” *Proceedings of the Royal Society A: Mathematical, Physical and Engineering Sciences*, vol. 466, no. 2116, pp. 1135–1154, 2010.
- [I26] M. A. Nielsen and I. L. Chuang, *Quantum Computation and Quantum Information: 10th Anniversary Edition*. Cambridge University Press, 2010.
- [I27] D. G. Tempel and A. Aspuru-Guzik, “Relaxation and dephasing in open quantum systems time-dependent density functional theory: Properties of exact functionals from an exactly-solvable model system,” *Chemical Physics*, vol. 391, pp. 130–142, Nov. 2011.
- [I28] H. R. Lewis and W. B. Riesenfeld, “An Exact Quantum Theory of the Time-Dependent Harmonic Oscillator and of a Charged Particle in a Time-Dependent Electromagnetic Field,” *Journal of Mathematical Physics*, vol. 10, pp. 1458–1473, Aug. 1969.
- [I29] Y.-Z. Lai, J.-Q. Liang, H. J. W. Müller-Kirsten, and J.-G. Zhou, “Time-dependent quantum systems and the invariant hermitian operator,” *Phys. Rev. A*, vol. 53, pp. 3691–3693, May 1996.
- [I30] E. Magesan, J. M. Gambetta, and J. Emerson, “Scalable and robust randomized benchmarking of quantum processes,” *Phys. Rev. Lett.*, vol. 106, p. 180504, May 2011.
- [I31] H. Q. Fan, K. H. Kagalwala, S. V. Polyakov, A. L. Migdall, and E. A. Goldschmidt, “Electromagnetically induced transparency in inhomogeneously broadened solid media,” *Phys. Rev. A*, vol. 99, p. 053821, May 2019.
- [I32] K. Tordrup and K. Mølmer, “Effects of ground-state hyperfine shifts in quantum computing with rare-earth-metal ions in solids,” *Phys. Rev. A*, vol. 75, p. 022316, Feb 2007.

Scientific publications

Author contributions

Paper I: Microscopic model of spin flip-flop processes in rare-earth-ion-doped crystals

I planned, prepared, and performed all the experiments with contributions from Chunyan Shi and Lars Rippe. I performed the simulations with Adam Kinos. I did the data analysis and wrote the manuscript, with discussions from all the authors.

Paper II: Experimental implementation of precisely tailored light-matter interaction via inverse engineering

I joined Ying Yan for the experiments and participated in the writing and analysis of the data. I was also involved in the discussions of the manuscript.

Paper III: Towards high fidelity transfers in $\text{Eu}^{3+} : \text{Y}_2\text{SiO}_5$ for quantum computing applications

I designed, prepared, and performed all the experiments with discussions from all the authors. I performed the simulations with contributions from Lars Rippe. I did the data analysis and wrote the manuscript, with discussions from all the authors.

